January 2009

Backscatter and Attenuation Characterization of Ventricular Myocardium

Allyson Gibson
Washington University in St. Louis

WASHINGTON UNIVERSITY IN SAINT LOUIS

Department of Physics

Dissertation Examination Committee:

James G. Miller, Chair
R. Martin Arthur
Patrick C. Gibbons
Charles M. Hohenberg
Mark R. Holland
Martin H. Israel
Gautam K. Singh

BACKSCATTER AND ATTENUATION CHARACTERIZATION OF VENTRICULAR MYOCARDIUM

by

Allyson Ann Gibson

A dissertation presented to the
Graduate School of Arts and Sciences
of Washington University in
partial fulfillment of the
requirements for the degree
of Doctor of Philosophy

August 2009

Saint Louis, Missouri

.

Abstract

This Dissertation presents quantitative ultrasonic measurements of the myocardium in fetal hearts and adult human hearts with the goal of studying the physics of sound waves incident upon anisotropic and inhomogeneous materials. Ultrasound has been used as a clinical tool to assess heart structure and function for several decades. The clinical usefulness of this noninvasive approach has grown with our understanding of the physical mechanisms underlying the interaction of ultrasonic waves with the myocardium.

In this Dissertation, integrated backscatter and attenuation analyses were performed on midgestational fetal hearts to assess potential differences in the left and right ventricular myocardium. The hearts were interrogated using a 50 MHz transducer that enabled finer spatial resolution than could be achieved at more typical clinical frequencies. Ultrasonic data analyses demonstrated different patterns and relative levels of backscatter and attenuation from the myocardium of the left ventricle and the right ventricle.

Ultrasonic data of adult human hearts were acquired with a clinical imaging system and quantified by their magnitude and time delay of cyclic variation of myocar-

dial backscatter. The results were analyzing using Bayes Classification and ROC analysis to quantify potential advantages of using a combination of two features of cyclic variation of myocardial backscatter over using only one or the other feature to distinguish between groups of subjects. When the subjects were classified based on hemoglobin A1c, the homeostasis model assessment of insulin resistance, and the ratio of triglyceride to high-density lipoprotein-cholesterol, differences in the magnitude and normalized time delay of cyclic variation of myocardial backscatter were observed. The cyclic variation results also suggested a trend toward a larger area under the ROC curve when information from magnitude and time delay of cyclic variation is combined using Bayes classification than when each feature is analyzed individually.

Ultrasound continues to be a powerful tool that enables noninvasive quantification of material properties. The studies in this Dissertation show that understanding the physical mechanisms behind the interaction of sound waves with myocardium can reveal new information about the structure, composition and overall state of the heart.

Acknowledgments

The work presented in this dissertation was not done in isolation, but benefited from many great scientists who are a part of the Laboratory for Ultrasonics at Washington University in St. Louis. My research would not have been possible without the support and guidance of my two advisors, James Miller and Mark Holland. I owe them both a great amount of gratitude for their patience, thoughtfulness, and enthusiasm. I would also like to thank Steve Baldwin, Scott Handley, Karen Marutyan, Becky Trousil, Kirk Wallace and Min Yang, who helped lay the foundation for my research, taught me the principles of ultrasound, and guided me as I began this journey. Special thanks also go to my friends and peers within the laboratory, Chris Anderson, Adam Bauer, Joe Hoffman, Ben Johnson, Todd Krueger, Chris Lloyd, and Amber Nelson for their support and helpful scientific discussions over the years.

In addition to the member of the Laboratory for Ultrasonics, this research benefited greatly from the energy and support of our collaborators at Barnes Jewish Hospital, Washington University School of Medicine, and the Division of Imaging and Applied Mathematics at the U.S. Food and Drug Administration. In particular I would like to acknowledge Dr. Gautam Singh and the team of Dr. Linda Peterson,

Dr. Jean Schaffer, Kyle Bilhorn, Marsha Farmer, Troy Haider, and Karla Robert for allowing me to be part of such interesting studies, and for teaching me about clinical cardiology, sonography, fetal hearts and diabetes. I would also like to recognize the late Dr. Robert Wagner for the joy he brought to my life, and for teaching me that statistical analysis could actually be fun.

I am deeply appreciative for the faculty and staff of the Department of Physics who offered support throughout my graduate school career. Specifically, Jan Foster, Julia Hamilton, Sarah Hedley, Alison Verbeck, and Tammy White-Devine all provided invaluable help navigating the administrative hoops of graduate school. Tony Biondo, Todd Hardt, and Denny Huelsman made the research possible by masterfully machining various parts for our experiments. Rita Wilson deserves thanks for keeping Compton Hall clean and for always managing to put a smile on my face.

I have been very lucky to have numerous friends who have supported me through my journey as a graduate student. I am grateful for my friendships with Seth Bartel, Adam Eggebrecht and Kasey Wagoner and for our great nights of music, cards, and conversations. I also want to thank Laurie Bauer, Charles Chung, Ashley Fitzgerald, Shannon Hoffman, Patrick Johnson, Tim Mitchell, Lauren Scott, Amy Sheldahl, Paul Rebillot, Vic Wessels, Dawn Yanker, Shannon Zareh and the rest of the physics crew for many fun cabin trips, weekend gatherings, flag football games, and breaks from work. Special thanks goes to Christopher Aubin, one of my first friends in St. Louis, who continually keeps me smiling and patiently answers my questions. In addition, I am indebted to the ANTM crew, especially Scott Hughes and Danette Wilson,

who have been an oasis for crazy conversations, fun TV, and great dinners for over 12 “cycles”. A huge thanks belongs to a wonderful group of women I met in St. Louis including Linda, Katie, Rebecca, Katie, Gabriella, Erin, and Anna who are so supportive, brought balance to my life, and were great fun. I am also profoundly grateful for my friendships with Michelle Milne and Becky Trousil. Both women are my pillars of support, confidants, and sounding boards. Thanks also to my friends at UUMC especially Laura Cochrane, Margaret Davis, Doug and Judith Durham, Beth Elders, Suzy Hamon, Linda Harris, Brad and Phyllis Hershey, Alice and John Mohr, Brenda Stobbe, Julie Thrasher, and Bette Welch.

I feel inordinately lucky to have a wonderfully supportive family and adopted families who have cheered me on throughout my life. I am deeply appreciative to the Clardys, Giddens, and Koenigs who have welcomed me into their families, and let me share in their joys and sorrows. I cannot thank enough the unquestioning support and encouragement of Clif Judy who shaped my life with his dreams and passions. I am also indebted to the Foster family, especially Jan Foster, who has shown me unbounded love and support, and brought a great deal of laughter and joy into my life. I am profoundly grateful for my parents, James and Elizabeth Gibson, who are sources of love, strength, inspiration, hope, and playfulness. I am also thankful for my sister, Kathryn Gibson, who is my role model, hero, and close friend. Thanks also to my grandmother, Beulah Brown, who, with every conversation, says, “I’m so proud of you”. My deepest thanks and gratitude go to Chris, someone I feel very fortunate to have in my life. Chris has brought a tremendous amount of support, comfort, joy,

and happiness to my life, and without him this whole process would have been much more challenging.

There are many people who directly and indirectly helped me along this journey and I am deeply grateful for all of their support. Had it not been for the many hands holding me up along the way, this work would not have been possible. Thank you!

Contents

List of Figures

List of Tables

Chapter 1

Introduction

1.1 Background and Motivation

The objective of this Dissertation is to study the physics of ultrasonic waves incident upon the anisotropic and inhomogeneous muscle of the heart, the myocardium. Understanding the physical mechanisms underpinning the interaction of sound waves with complex materials can elucidate information about the structure and composition in a nondestructive manner. Additionally, analysis of the observed acoustic parameters can highlight potentially occult anomalies. These ultrasonic techniques of interrogation are useful in a wide range of applications, and are applied to the study of the myocardium in this Dissertation.

Ultrasound has been used as a clinical tool to assess heart structure and function for several decades. The clinical usefulness of this noninvasive approach has grown with our understanding of the physical mechanisms underlying the interaction of ultrasonic waves with the myocardium. Laboratory measurements of the speed of

sound, attenuation of the ultrasonic signal, and the backscattered ultrasonic energy have been an ongoing focus of the Washington University Physics Department's Laboratory for Ultrasonics (Baldwin *et al.*, 2005a,b; Hall *et al.*, 1997; Hoffmeister *et al.*, 1994, 1995, 1996; Madaras *et al.*, 1988; Mottley and Miller, 1988, 1990; Sosnovik *et al.*, 2001; Verdonk *et al.*, 1992, 1996; Yang *et al.*, 2006). These qualitative measurements have been useful in characterizing properties of the myocardium.

Quantitative ultrasonic measurements have enhanced clinical ultrasound by measuring differences between the material properties of normal and diseased hearts. Numerous studies have shown quantitative differences in the acoustic properties of hearts with specific pathologies relative to those of normal hearts (Barzilai *et al.*, 1988, 1990; Feinberg *et al.*, 1996; Holland *et al.*, 2004; Mottley *et al.*, 1984; Perez *et al.*, 1992, 1995; Wagner *et al.*, 1995). By further understanding the physical mechanisms associated with the interaction of ultrasound waves and normal and diseased soft tissue, one can envision new and novel techniques to enhance the assessment of a patient's heart.

This Dissertation is a step to further understanding the physical mechanisms behind the propagation of ultrasonic waves in specific anisotropic and inhomogeneous materials. This work deals with both laboratory based measurements of ultrasonic properties in fetal hearts and with clinically based measurements in the adult hearts of normal subjects and subjects with type 2 diabetes. A long term goal of the studies reported in this Dissertation is to contribute to the knowledge base that might ultimately provide improved diagnoses of congenital heart disease and of diabetic

cardiomyopathy.

1.2 Overview of the Dissertation

The first portion of the Dissertation focuses on studies of the left and right ventricular myocardium in formalin-fixed fetal hearts using data acquired over 30 to 60 MHz. The aim of this section is to elucidate the similarities and differences between the structure and composition of left and right sided ventricular myocardium using a high-frequency ultrasound system. Numerous studies have focused primarily on the left ventricular myocardium, whereas this work extends that knowledge by comparing the ultrasonic properties of the right ventricular myocardium to that of the left.

Chapter 2 begins the study of the regional variation of the left and right ventricular myocardium in mid-gestational fetal pig hearts by analyzing the backscattered energy. The measurements were performed using a single element transducer centered at 50 MHz, an approach that permitted finer spatial resolution than would be achieved at a more typical clinical frequency of 5 MHz. Although both ventricles of the developing fetal heart are exposed to similar pressures, an important determinant of ventricular properties, the results of this study documented differences in the fiber architecture and composition between the myocardium of the left and right ventricle in the mid-gestational fetal hearts.

Chapter 3 continues the study of mid-gestational fetal hearts by measuring the regional differences in the ultrasonic attenuation properties of the ventricular my-

ocardium. In this study the myocardium of the left and right ventricle exhibited differences in both the attenuation coefficient at mid-bandwidth and the frequency dependence of the attenuation coefficient (the so-called slope of attenuation). This study provided further evidence that the structure and composition of the left and right ventricular myocardium are distinct in fetal hearts at mid-gestation.

Chapter 4 presents images of the apparent integrated backscatter, slope of attenuation, and attenuation coefficient at 45 MHz for the midgestational fetal pig hearts discussed in Chapters 2 and 3. These images help demonstrate the differences between the left and right ventricular myocardium, and the relationship between the three ultrasonic measurements.

The second portion of the Dissertation, presented in Chapter 5, is a study of the left ventricular myocardium in adult human hearts. This work measures acoustic properties from backscattered ultrasound using a clinical imaging system. Interpretation of the results of these *in vivo* studies benefits from knowledge obtained in studies similar to those presented in the first portion of this Dissertation.

The work presented in Chapter 5 quantifies the systematic variation (cyclic variation) of myocardial ultrasonic backscatter over the heart cycle in asymptomatic type 2 diabetic patients and in normal control subjects. The study uses Bayes classification and ROC (Receiver Operator Characteristic) analysis to quantify potential advantages of using a combination of two features of the cyclic variation of myocardial backscatter over using only one or the other feature to distinguish between groups of subjects.

A summary of the Dissertation and closing remarks are presented in Chapter 6.

Bibliography

Baldwin, S. L., Holland, M. R., Sosnovik, D. E., and Miller, J. G. (**2005**a). "Effects of region-of-interest length on estimates of myocardial ultrasonic attenuation and backscatter", Med Phys **32**, 418–26.

Baldwin, S. L., Marutyan, K. R., Yang, M., Wallace, K. D., Holland, M. R., and Miller, J. G. (**2005**b). "Estimating myocardial attenuation from M-mode ultrasonic backscatter", Ultrasound Med Biol **31**, 477–84.

Barzilai, B., Thomas, Lewis J., I., Glueck, R. M., Saffitz, J. E., Vered, Z., Sobel, B. E., Miller, J. G., and Perez, J. E. (**1988**). "Detection of remote myocardial infarction with quantitative real-time ultrasonic characterization", J. Am. Soc. Echocardiogr **1**, 179–186.

Barzilai, B., Vered, Z., Mohr, G. A., Wear, K. A., Courtois, M., Sobel, B. E., Miller, J. G., and Perez, J. E. (**1990**). "Myocardial ultrasonic backscatter for characterization of ischemia and reperfusion: Relationship to wall motion", Ultrasound Med Biol **16**, 391–398.

Feinberg, M. S., Gussak, H. M., Davila-Roman, V. G., Baumann, C. M., Miller, J. G., and Perez, J. E. (**1996**). "Dissociation between wall thickening of normal myocardium and cyclic variation of backscatter during inotropic stimulation", Am J Cardiol **77**, 515–520.

Hall, C. S., Verdonk, E. D., Wickline, S. A., Perez, J. E., and Miller, J. G. (**1997**). "Anisotropy of the apparent frequency dependence of backscatter in formalin fixed human myocardium", J. Acoust. Soc. Am. **101**, 563–568.

Hoffmeister, B. K., Handley, S. M., Wickline, S. A., and Miller, J. G. (**1996**). "Ultrasonic determination of the anisotropy of Young's modulus of fixed tendon and fixed myocardium", J. Acoust. Soc. Am. **100**, 3933–3940.

Hoffmeister, B. K., Verdonk, E. D., Wickline, S. A., and Miller, J. G. (**1994**). "Effect of collagen on the anisotropy of quasi-longitudinal mode ultrasonic velocity in fibrous soft tissues: A comparison of fixed tendon and fixed myocardium", J. Acoust. Soc. Am. **96**, 1957–1964.

Hoffmeister, B. K., Wong, A. K., Verdonk, E. D., Wickline, S. A., and Miller, J. G. (**1995**). "Comparison of the anisotropy of apparent integrated ultrasonic backscatter from fixed human tendon and fixed human myocardium", J. Acoust. Soc. Am. **97**, 1307–1313.

Holland, M. R., Wallace, K. D., and Miller, J. G. (**2004**). "Potential relationships among myocardial stiffness, the measured level of myocardial backscatter ("image brightness") and the magnitude of the systematic variation of backscatter (cyclic variation) over the heart cycle", J. Am. Soc. Echocardiogr **17**, 1131–1137.

Madaras, E., Perez, J., Sobel, B., Mottley, J., and Miller, J. (**1988**). "Anisotropy of the ultrasonic backscatter of myocardial tissue: II. Measurements in vivo", J. Acoust. Soc. Am. **83**, 762–769.

Mottley, J. G., Glueck, R. M., Perez, J. E., Sobel, B., and Miller, J. (**1984**). "Regional differences in the cyclic variation of myocardial backscatter that parallel regional differences in contractile performance", J. Acoust. Soc. Am. **76**, 1617–1623.

Mottley, J. G. and Miller, J. (**1988**). "Anisotropy of the ultrasonic backscatter of myocardial tissue: I. theory and measurements in vitro", J. Acoust. Soc. Am. **83**, 755–761.

Mottley, J. G. and Miller, J. G. (**1990**). "Anisotropy of the ultrasonic attenuation in soft tissues: Measurements in vitro", J. Acoust. Soc. Am. **88**, 1203–1210.

Perez, J. E., Davila-Roman, V. G., and Miller, J. G. (**1995**). "Assessment of myocardial viability by ultrasonic tissue characterization", Coronary Artery Disease **6**, 613–618.

Perez, J. E., McGill, J. B., Santiago, J. V., Schechtman, K. B., Waggoner, A. D., Miller, J. G., and Sobel, B. E. (**1992**). "Abnormal myocardial acoustic properties in diabetic patients and their correlation with the severity of disease", J. Am. Coll. Cardiol. **19**, 1154–1162.

Sosnovik, D. E., Baldwin, S. L., Holland, M. R., and Miller, J. G. (**2001**). "Transmural variation of myocardial attenuation and its potential effect on contrast-mediated estimates of regional myocardial perfusion", J Am Soc Echocardiogr **14**, 782–8.

Verdonk, E. D., Hoffmeister, B. K., Wickline, S. A., and Miller, J. G. (**1996**). "Anisotropy of the slope of ultrasonic attenuation in formalin fixed human myocardium", J. Acoust. Soc. Am. **99**, 3837–3843.

Verdonk, E. D., Wickline, S. A., and Miller, J. G. (**1992**). "Anisotropy of ultrasonic velocity and elastic properties in normal human myocardium", J. Acoust. Soc. Am. **92**, 3039–3050.

Wagner, R. F., Wear, K. A., Perez, J. E., McGill, J. B., Schechtman, K. B., and Miller, J. G. (**1995**). "Quantitative assessment of myocardial ultrasonic tissue characterization through Receiver Operating Characteristic analysis of Bayesian classifiers", J. Am. Coll. Cardiol. **25**, 1706–1711.

Yang, M., Baldwin, S. L., Marutyan, K. R., Wallace, K. D., Holland, M. R., and Miller, J. G. (**2006**). "Elastic stiffness coefficients (c11, c33, and c13) for freshly excised and formalin-fixed myocardium from ultrasonic velocity measurements", J Acoust Soc Am **119**, 1880–1887.

Chapter 2

Measurements of Apparent Ultrasonic Backscatter

2.1 Preface

This chapter is based on the peer-reviewed journal article *Regional Variation in the Measured Apparent Ultrasonic Backscatter of Mid-Gestational Fetal Pig Hearts* written by Allyson A. Gibson, Gautam K. Singh, Agnieszka Kulikowska, Kirk D. Wallace, Joseph J. Hoffman, Achiau Ludomirsky, Mark R. Holland and published in *Ultrasound in Medicine & Biology, Vol. 33, No. 12, pp. 1955-1962, 2007*

2.2 Abstract

The goal of this study was to characterize and compare regional backscatter properties of fetal hearts through measurements of the apparent integrated backscatter. Sixteen excised, formalin-fixed fetal pig hearts, representing an estimated 53-63 days of gestation, were investigated. Spatially localized measurements of integrated backscatter from these specimens were acquired using a 50-MHz single-element transducer. The apparent integrated backscatter measurements demonstrate different patterns of backscatter from the myocardium of the right ventricle compared to that of the left ventricle. These backscatter measurements appear to be consistent with the anisotropy of the fiber orientation observed in histological assessment of the same specimens. For each of the 16 hearts, the apparent integrated backscatter from the right ventricular myocardium was larger than that from the left ventricular myocardium exhibiting mean apparent backscatter values of -35.9 $\pm$ 2.0 dB and -40.1 $\pm$ 1.9 dB (mean $\pm$ standard deviation; N = 16; p <0.001), respectively. This study suggests that the intrinsic ultrasonic properties of the left and right ventricular myocardium are distinct in fetal pig hearts at mid-gestation.

2.3 Introduction

Although previous studies have demonstrated significant regional differences in measured ultrasonic backscatter in mature hearts (Hoyt *et al.*, 1984), relatively little is known regarding these differences in the fetal heart. Because both ventricles of

the fetal heart are exposed to similar prenatal loading conditions, which represent an important determinant of ventricular geometry, one might anticipate that the myoarchitecture of the two ventricles would develop similarly. However, embryologic studies suggest that the left- and right-ventricular myocardium develop differently which leads to a particular interest in quantifying the intrinsic differences in the left and right ventricular myoarchitecture and properties of the developing heart (Perles *et al.*, 2007; Salih *et al.*, 2004; Smolich *et al.*, 1989). The objective of this investigation was to characterize and compare the relative regional ultrasonic backscatter properties of the myocardium in the left-ventricular and right-ventricular free walls in fetal hearts. Our approach was to investigate excised formalin-fixed, mid-gestational fetal pig heart specimens by measuring the backscattered ultrasound from a thin slice of the heart. Mid-gestational fetal pig hearts were chosen for this study because the gross structural formation of the heart is completed by this time point, and fetal pigs of this gestational age are similar in gestational age to human fetuses referred for fetal echocardiography at our clinic at St. Louis Children's Hospital. The measurements performed in this study focus on the relative left-ventricular and right-ventricular myocardium backscatter properties of the heart. Although formalin fixation can affect the absolute level of apparent backscatter (Baldwin *et al.*, 2005d; Hall *et al.*, 2000a; Takiuchi *et al.*, 2001) the relative differences are expected to be largely preserved.

Previous studies from our laboratory and others have demonstrated the relationship between measured ultrasonic parameters (ultrasonic attenuation, backscatter, speed of sound) and the inherent properties of myocardial tissue. Both the nature of

the intrinsic material properties (e.g., the types and concentrations of proteins present resulting in specific intracellular and extracellular viscoelastic properties) as well as the geometrical properties (structural morphology) of the myocardium combine to produce the observed ultrasonic parameters (Hall *et al.*, 2000b,c; Kumar and Mottley, 1994; Madaras *et al.*, 1988; Mottley and Miller, 1988; O'Brien *et al.*, 1995b,a; Rose *et al.*, 1995; Wickline *et al.*, 1985). For example, several studies have demonstrated that an increase in both the measured ultrasonic attenuation and backscatter correlate well with increased collagen concentration in the myocardium (Davison *et al.*, 1995; Hall *et al.*, 1997, 2000c; Hoyt *et al.*, 1984, 1985; Mimbs *et al.*, 1980, 1981; Nguyen *et al.*, 2001; O'Donnell *et al.*, 1981; Perez *et al.*, 1984; Pohlhammer and O'Brien, 1981; Wear *et al.*, 1989; Wickline *et al.*, 1992; Wong *et al.*, 1992, 1993).

In addition, effects of the structural properties of myocardium, such as myofiber orientation, on measured ultrasonic parameters are manifest in the angle-of-insonification-dependent (*anisotropic*) nature of the myocardium. These anisotropic properties have been observed in measurements of ultrasonic backscatter, attenuation, and speed of sound (Baldwin *et al.*, 2005a,b; Hoffmeister *et al.*, 1994, 1995, 1996; Madaras *et al.*, 1988; Mottley and Miller, 1988, 1990; Sosnovik *et al.*, 2001; Verdonk *et al.*, 1992, 1996; Yang *et al.*, 2006). These studies demonstrate that the ultrasonic backscatter and longitudinal velocity are significantly larger and the attenuation properties are significantly smaller for insonification perpendicular to the myofibers compared with the corresponding values for parallel insonification.

Because the intrinsic material properties and the myofiber orientation contribute

to the observed ultrasonic attenuation and backscatter properties (Baldwin *et al.*, 2005a,b; Hall *et al.*, 2000b,c; Hoffmeister *et al.*, 1995; Kumar and Mottley, 1994; Madaras *et al.*, 1988; Mottley and Miller, 1988, 1990; O'Brien *et al.*, 1995b,a; Rose *et al.*, 1995; Sosnovik *et al.*, 2001; Verdonk *et al.*, 1996; Wickline *et al.*, 1985), echocardiographic images reflect these intrinsic properties of the heart. Studies by our laboratory and others have demonstrated the profound effects that the intrinsic properties of myocardial tissue have on two-dimensional echocardiographic images (Aygen and Popp, 1987; Holland *et al.*, 1998, 2005; Recchia *et al.*, 1993; Sosnovik *et al.*, 2001). These studies suggest that measurements of the backscatter from myocardium may provide a method to assess differences in the intrinsic properties of the myocardium as the heart develops.

2.4 Methods

2.4.1 Preparation of specimens

A total of 16 age-bracketed, formalin-fixed fetal pigs were obtained from Nebraska Scientific Inc. (Omaha, NE, USA) in compliance with approved procedures established by the Animal Studies Committee at Washington University in St. Louis. The heart and humerus bone were harvested from each of the fetal pigs and placed in 10% formalin solution. Potential effects of formalin fixation on the tissue and resulting measurements are addressed in Section 2.7, (Limitations). After extraction of the fetal heart, the pericardial sac was removed, and the exterior of the left ventricular free wall

was identified and marked with black India ink (Bradley Products Inc., Bloomington, MA, USA) to aid in ventricular identification after slicing. Because the transmural thickness of the ventricular myocardium in the fetal heart appears similar in the left and right side, and the typical morphological appearance of the left and right ventricles in a short axis view (circular left ventricle and a crescent-shaped right ventricle) is not always readily apparent, marking the left side of the heart prior to cutting proved useful. After marking the heart, the atria were removed from the specimen by cutting at a position basal to the atrial-ventricular valve plane. The remaining ventricular section of the heart was glued to a plastic plug and encased in agarose (Sigma-Aldrich Co., St. Louis, MO, USA). Surrounding the heart with agarose provided a uniform cylindrical exterior that closely fit into a custom-designed sectioning tool pictured in Figure 2.1. The sectioning tool was used to cut thin (approximately 1.0 mm) flat and parallel slices of the fetal heart. Each heart was sectioned in a transverse plane, perpendicular to the long axis of the heart, at the mid-papillary level to provide short-axis cross-sectional slices. Figure 2.2 shows a representative short-axis cross-sectional slice of a fetal pig heart used in this investigation.

In addition to the fetal pig heart, the humerus bone was excised to permit estimation of the gestational age of the pig fetus. A linear relationship between the diaphyseal length of the humerus bone and the gestational age of the pig fetus was described by Wrathall et al. (1974). In our study the estimated gestational ages of the 16 fetal pigs ranged from 53 to 63 days with a mean of 57 days, representing approximately half of the gestational age of a pig (full gestation of a pig is $\sim$120

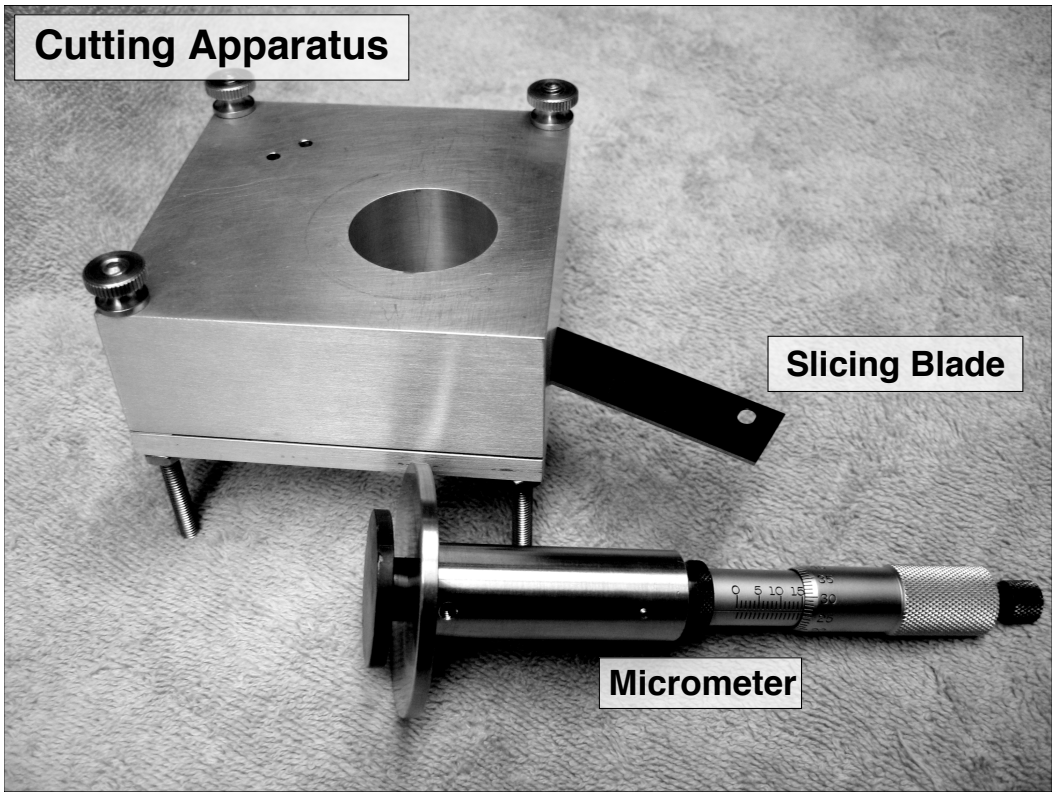

FIGURE 2.1: An image of the custom-designed sectioning tool that was used to cut thin, flat and parallel slices of the fetal heart. The tool was used by inserting an agarose encased heart into the barrel of the micrometer. The micrometer was then placed on top of the cutting tool such that the encased heart fit closely into the hole of the cutting apparatus. This close fit prevented slipping or bunching of the heart as the blade cut through the specimen. The thickness of each slice was determined by adjusting the depth of the micrometer from one cut to the next.

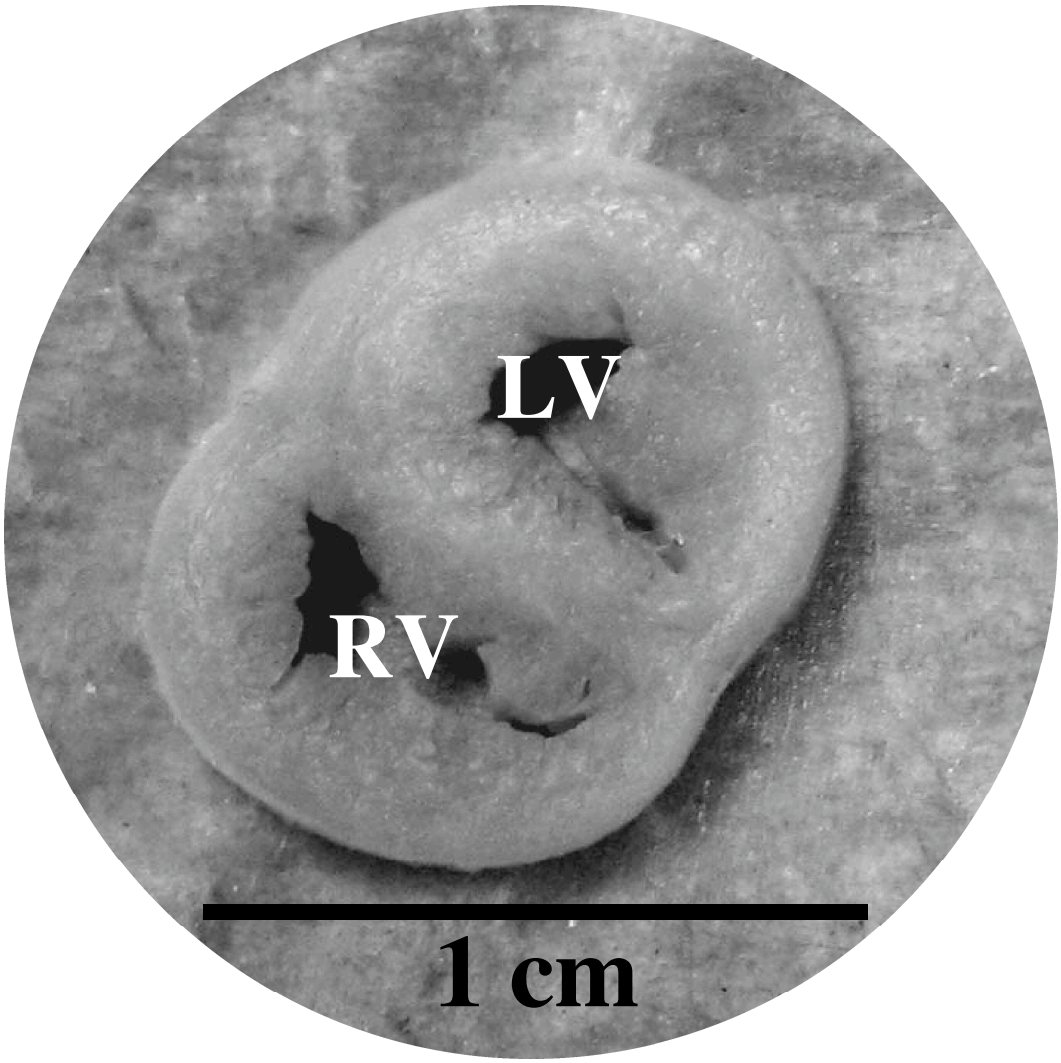

FIGURE 2.2: Representative short-axis cross-sectional slice of a fetal pig heart. LV=left ventricle; RV=right ventricle

days).

2.4.2 Acquisition of ultrasonic backscatter data

The approximately 1.0 mm-thick fetal heart specimens were mounted on a stainless-steel plate and placed in a custom-designed and constructed water tank. Backscattered ultrasonic signals were obtained from the specimens using a broadband, 50-MHz center frequency, single-element transducer (6.35 mm diameter, 12.7 mm focus, Panametrics V390; Panametrics Inc., Waltham, MA, USA) with 6 dB bandwidth of 30-60 MHz. The transducer's angle of insonification was perpendicular to the cut face of the myocardial slice. Figure 2.3b is an image of the experimental setup showing the orientation of the transducer with respect to the myocardial slice. It should be noted that at 50 MHz the ultrasonic beam diameter is approximately 60 μm, and is significantly smaller than the diameter of the transducer casing seen in the image. The transducer was used in pulse-echo mode, and translated in a C-scan over the entire specimen using a Newport XPS motion controller (Newport Corp., Mountain View, CA, USA) in 50 μm steps. The vertical position of the transducer was adjusted to place the focal distance 0.25 mm below the face of the tissue. In our experimental setup, a Panametrics 5900 pulser/receiver was used to trigger a Panametrics 5627RPP-1 remote pulser/preamplifier, which sent a pulse to the Panametrics V390 50-MHz transducer. The backscattered signal from each interrogated site of the myocardial specimen was pre-amplified by the Panametrics 5627RPP-1 remote pulser/preamplifier and sent to the Panametrics 5900 pulser/receiver. The amplified output

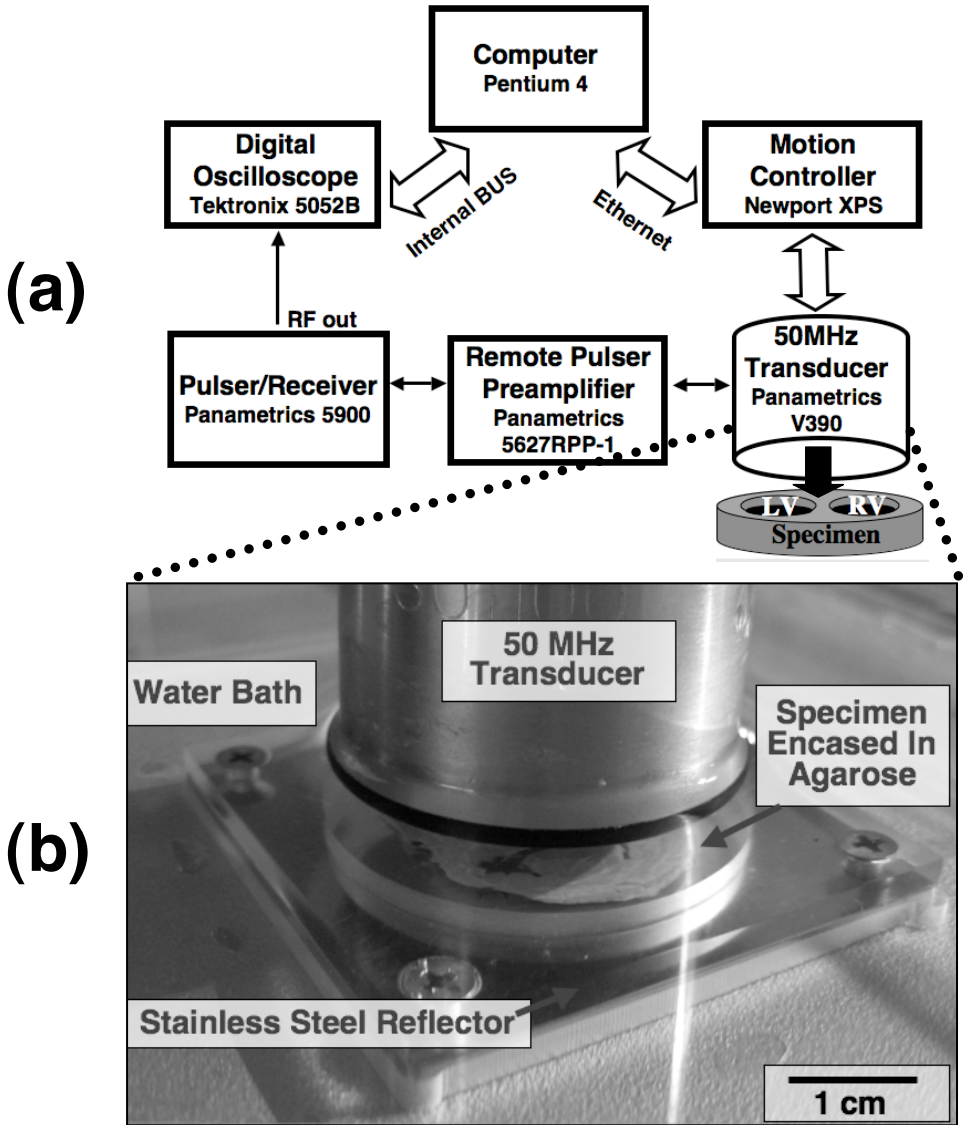

FIGURE 2.3: (a) Block diagram illustrating the experimental setup. The data acquisition computer is imbedded in the Tektronix 5052B digital oscilloscope. (b) Picture of the experimental setup showing the 50 MHz transducers position relative to the cut face of the fetal pig heart specimen. At 50 MHz the ultrasonic beam diameter is approximately 60 μm and is considerably smaller than the dimensions of the transducer casing shown in the image.

from the pulser/receiver was digitized at 625 megasamples-per-second, signal averaged 256 times, and stored as a 2500-point record using a Tektronix 5052B digital oscilloscope with 8-bit digitization (Tektronix Inc., Beaverton, OR, USA). Figure 2.3a shows a block diagram illustrating the experimental setup for these measurements. In addition to the tissue backscatter traces, specular reflections from the stainless-steel plate were acquired to utilize as reference signals. The reference signals used the same acquisition parameters as the backscatter traces with the exception of where the transducer was focused and the input attenuation. In the backscatter traces the focal distance of the ultrasonic beam was placed below the face of the tissue; whereas, the ultrasonic beam was focused on the front wall of the steel plate for the reference traces. Electronic gain and attenuation were adjusted for both the reference and backscatter signals to utilize the full dynamic range of the measurement system. These gain and attenuation settings were compensated for in subsequent analyses of the data.

2.4.3 Integrated backscatter image formation

For each backscattered radio-frequency (RF) signal obtained from the specimen, a 0.67 μs (0.50 mm) segment of the backscattered ultrasound waveform was gated using a Tukey window. Figure 2.4 shows a representative RF trace from one site with the corresponding gated region indicated. A 0.67 μs gate length was chosen because it includes half the thickness of the 1.0 mm slice. A Tukey window was selected to minimize gating artifacts. Because integrated backscatter values (frequency averaged) were used to quantify the level of apparent backscatter the choice of window should

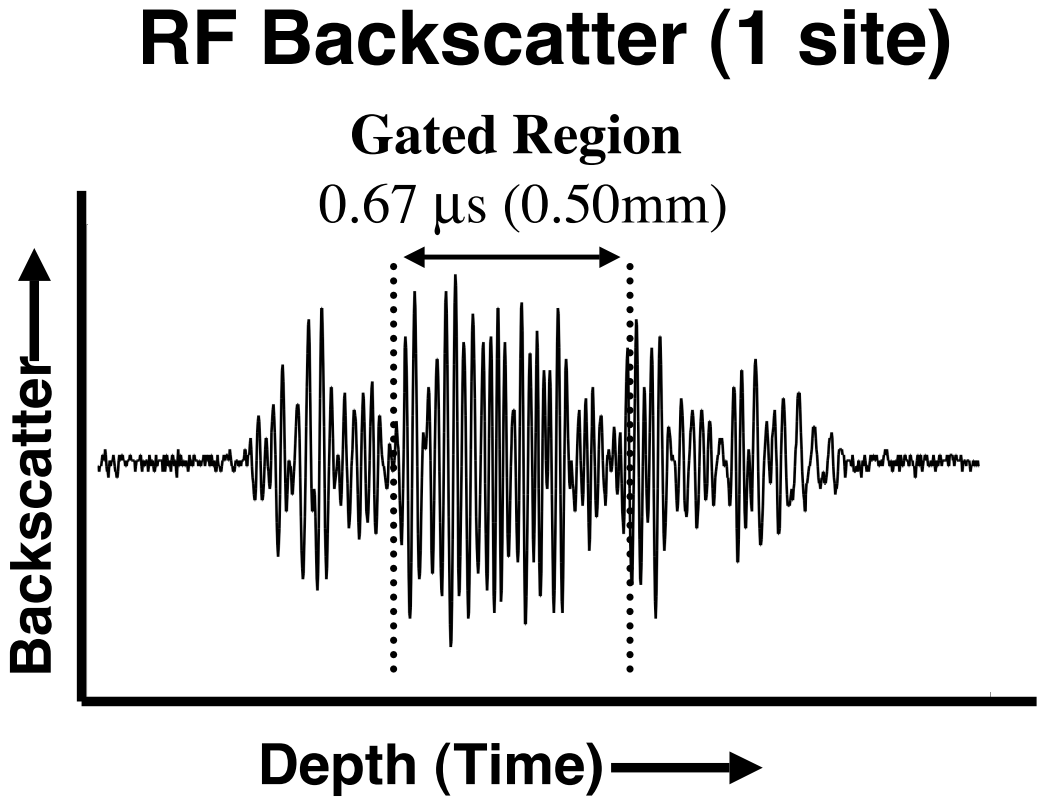

FIGURE 2.4: Representative picture of a RF (radio-frequency) backscatter trace and the corresponding gated region.

not have significantly affected the results of the study. The start of the windowing gate was placed 0.33 μs (0.25 mm) behind the front wall of the tissue such that scattering from the center of the tissue was interrogated, and the specular reflection from the front wall of the specimen was avoided. The backscattered power spectrum from the gated region was determined using a fast Fourier transform and expressed in decibels (dB).

For each myocardial site interrogated, the apparent backscatter transfer function was determined by subtracting the reference power spectrum (the specular echo off of the stainless-steel plate, expressed in dB) from the myocardial backscatter power spectrum (also expressed in dB) and compensated for differences in the input attenuation or gain from the pulser/receiver between the two data acquisitions. The apparent integrated backscatter value was determined by averaging the apparent backscatter transfer function over the useful frequency range from 30 MHz to 60 MHz. Subsequently, this average was converted to a grayscale value and displayed as a pixel in an image. This algorithm was applied to each backscattered RF signal to form an image of the entire fetal pig heart slice. All the images were displayed over the same dynamic range of 30 dB so that the 16 fetal hearts could be compared. All data analyses were performed using Igor Pro (WaveMetrics Inc., Portland, OR, USA) on a PowerBook G4 (Apple Inc., Cupertino, CA, USA).

2.4.4 Measurement of ultrasonic backscatter from the left-ventricular and right-ventricular free walls

To compare the level of backscatter from left-ventricular and right-ventricular myocardium, measurements were obtained from those regions exhibiting the largest level of backscatter within the two ventricular walls. These regions were chosen because they represent areas of perpendicular insonification relative to the predominant myofiber orientation, as demonstrated by previous studies from our laboratory that characterized the level of apparent backscatter and fiber orientation, using both high and low frequencies (Bridal *et al.*, 1993; Hoffmeister *et al.*, 1995; Mottley and Miller, 1988; Sosnovik *et al.*, 2001), as well as the histological measurements described in Section 2.5 (Results). By choosing to compare the areas of perpendicular insonification in both ventricles, the confounding effects of tissue anisotropy on measurements of apparent integrated backscatter (Hoffmeister *et al.*, 1995; Mottley and Miller, 1988; Sosnovik *et al.*, 2001) are significantly reduced.

To quantify the level of backscatter from the myocardium of the left and right ventricles, regions of interest were drawn on each image and analyzed. Figure 2.5 shows a representative integrated backscatter image of one of the fetal pig heart specimens. The size and placement of the region of interest for measurements of the level of backscatter from the left- and right-ventricular myocardium are depicted in the figure.

Each region of interest was centered on a line bisecting the ventricular free walls

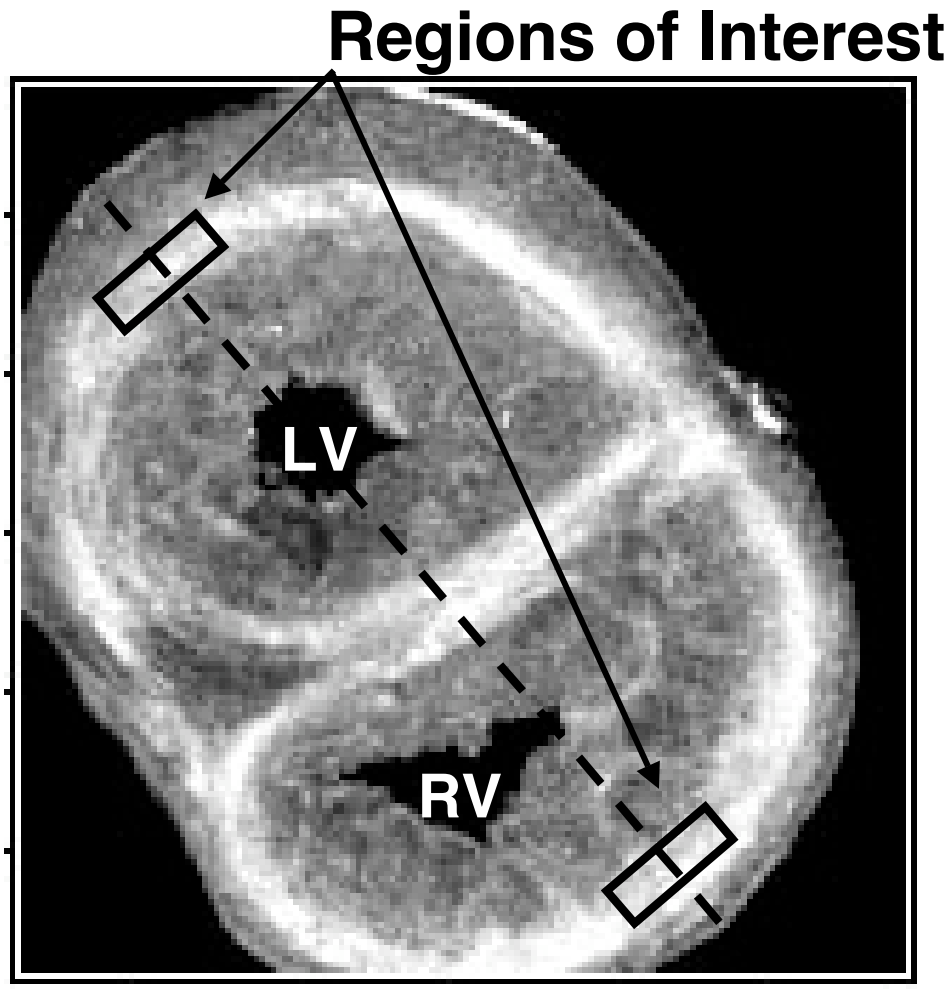

FIGURE 2.5: Representative integrated backscatter image of a fetal pig heart illustrating the positions of the regions of interest. LV=left ventricle; RV=right ventricle

and septum. The dashed line in Figure 2.5 represents this bisecting line. Because the region of investigation was chosen to represent that in which the myofibers are perpendicular to the angle of insonification, the regions of interest for each specimen were drawn to fit within the thinnest transmural bright region and then translated along the bisecting line. Because the ventricular free walls are curved in opposite directions with respect to each other, the width of the region of interest was limited to that which would fit in both ventricular walls.

The size of the region of interest placed in each heart's bright band was uniform within each individual heart, but varied between different hearts depending on the transmural thickness of the bright band. The average area for all the regions of interests was 0.625 mm^2. The regions of interest were always chosen to be small enough to only cover the band of perpendicular insonification, but large enough to provide reasonable spatial averaging.

2.5 Results

2.5.1 Myofiber Architecture

The images representing measurements of the apparent integrated backscatter illustrate different patterns of backscatter in the left and right ventricular free walls, implying distinct ventricular myoarchitecture between the two sides. Within the left-ventricular free wall, the largest level of backscatter is located in a band within the mid-myocardium and regions of decreased apparent backscatter are located subepi-

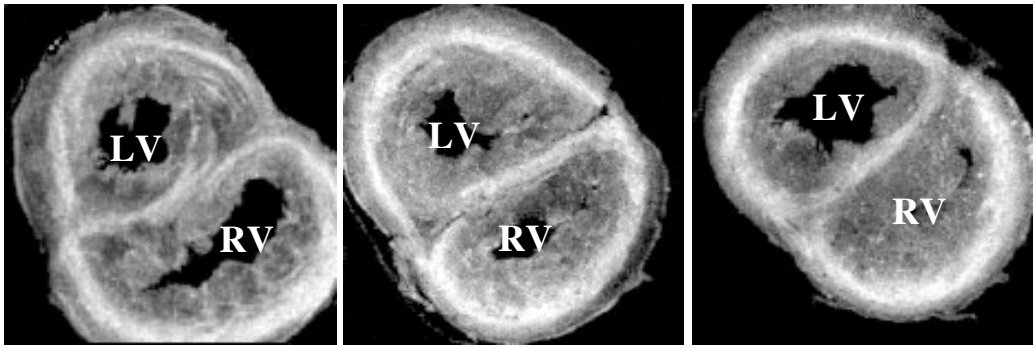

FIGURE 2.6: Representative integrated backscatter images obtained from three of the fetal pig heart specimens. LV=left ventricle; RV=right ventricle

cardially and subendocardially. The right ventricular free wall shows the largest level of apparent backscatter in a subepicardial band with less apparent backscatter measured in the subendocardial region. Figure 2.6 illustrates the apparent backscatter images obtained from three of the fetal pig specimens. These images are typical of those obtained from all 16 specimens.

To examine the relationship between the level of apparent backscatter and myofiber orientation, several of the ultrasonically imaged hearts were further sliced and stained with H&E (hematoxylin and eosin) to visually differentiate microstructure of the slice. Histological analyses demonstrate that the largest (brightest) regions of backscatter in the ventricular free walls correspond to those associated with perpendicular insonification relative to the circular myofiber orientation, whereas the less bright regions represent non-perpendicular insonification. Figure 2.7 shows the apparent integrated backscatter image and corresponding histology images for the same

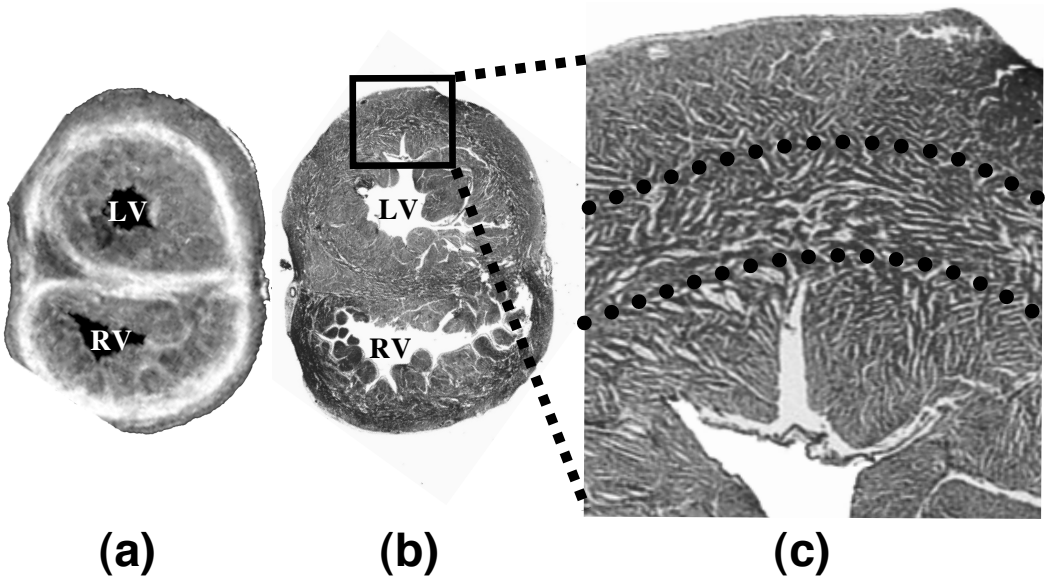

FIGURE 2.7: (a) Apparent integrated backscatter image and (b) corresponding histology image (hematoxylin and eosin stain) of the same fetal pig heart. (c) Magnified histology of the left-ventricular free wall. The area enclosed by the dotted lines represents that in which the myofibers run perpendicular to the direction of insonification, which is into the paper relative to the specimen. LV=left ventricle; RV=right ventricle

fetal heart specimen. Figure 2.7c is a magnified section of the left-ventricular free wall in Figure 2.7b. In Figure 2.7c the area between the two dotted lines represents the region where the myofibers are perpendicular to the direction of insonification and correspond to the white area in the left-ventricular free wall of Figure 2.7a. The direction of insonification is into the paper relative to the specimens in Figure 2.7.

2.5.2 Comparison of Apparent Integrated Backscatter

Figure 2.8 displays the results of the measured level of backscatter from the regions of maximum backscatter (bright bands) in the left-ventricular and right-ventricular

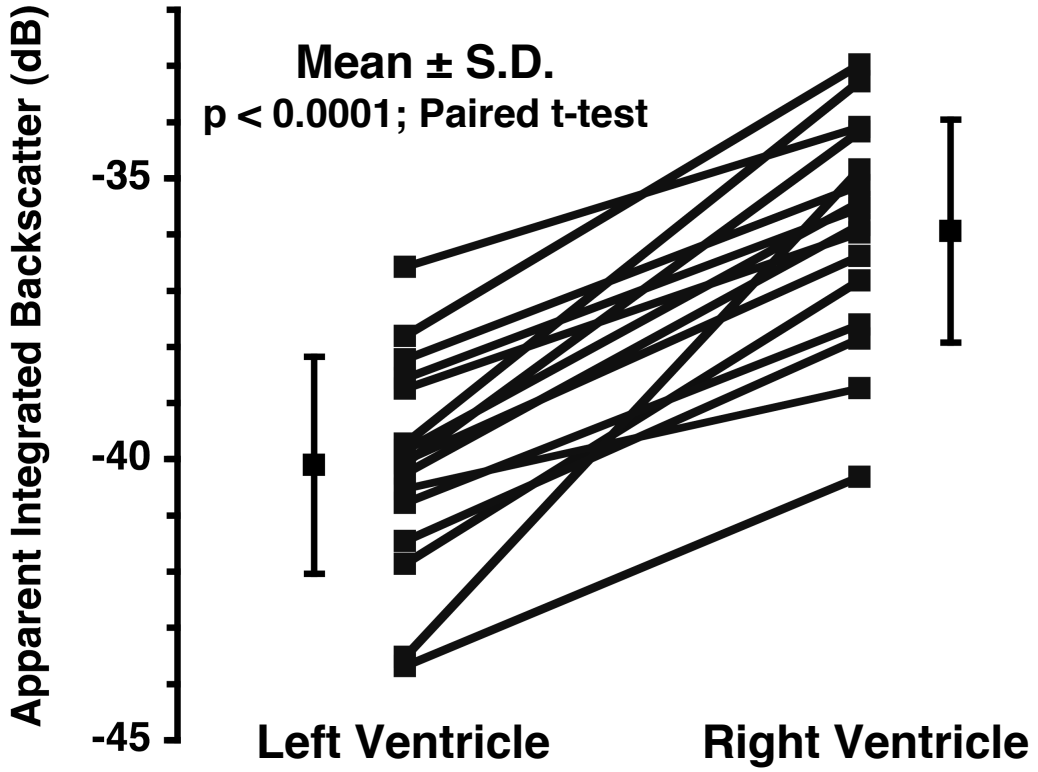

FIGURE 2.8: Individual and mean values of the measured backscatter from the bright bands in the left ventricular and right ventricular myocardium of the fetal pig heart.

myocardium for each of the 16 fetal pig hearts along with the corresponding mean levels. In general, the apparent integrated backscatter for the right ventricular myocardium was larger than that for the left ventricular myocardium ($p < 0.0001$; paired t-test). The mean apparent integrated backscatter from all of the heart slices was found to be -35.9 $\pm$ 2.0 dB and -40.1 $\pm$ 1.9 dB (mean $\pm$ standard deviation; $N = 16$; $p < 0.001$; unpaired two-tailed t-test) from the myocardium of the right ventricle and left ventricle, respectively, representing a 4.2 dB greater level of backscatter in the right-ventricular myocardium than the left-ventricular myocardium.

2.6 Discussion

Measurements of the apparent integrated backscatter from the mid-gestational fetal pig hearts examined in this study demonstrate significant transmural variations in the level of backscatter from the left-ventricular and right-ventricular myocardium. High-frequency apparent integrated backscatter images typically show the largest level of apparent integrated backscatter in the mid-myocardium of the left-ventricular free wall and in the subepicardial region of the right-ventricular free wall. This observation is consistent with the morphological architecture in the three-dimensional organization of muscle fibers for prenatal and adult human hearts described by Sanchez-Quintana et al. (1995). In their study, they found the left-ventricular wall to be arranged in three layers: a subepicardial (superficial) layer, a middle layer, and a deep (subendocardial) layer. The superficial and deep layers were present in both ventri-

cles; however, the middle layer was found only in the left-ventricular myocardium. Age-related differences were noted in the pattern of myoarchitecture of the superficial layer, mainly during the fetal period. Our ultrasound measurements appear to be in agreement with the histological images (Figure 2.7) in which the maximum level of backscatter occurs in those regions representing perpendicular insonification relative to the predominant fiber orientation.

Our experimental measurements demonstrate a lesser degree of backscatter from the brightest region of the left ventricle than from the brightest region of the right ventricle. This result is reflected both in the mean backscatter level for the 16 pigs and in general within each fetal pig. This difference in backscattered energy between the ventricular free walls suggests an intrinsic difference in the myocardium of the left and right ventricles. Studies by Smolich et al. (1989) demonstrated that morphological differences exist between the left and right ventricular myocardium during fetal and postnatal development of sheep hearts. They reported significantly larger myocyte cross-sectional area, capillary luminal area, and intercapillary distance in the right ventricle as compared to the left. Additionally they describe the significantly smaller myocyte density, capillary density, and the myocyte matrix volume density in the right ventricle compared to the densities of those objects in the left ventricle during development. Several studies investigating the mechanisms of ultrasonic scattering have demonstrated the effects of scatterer size, shape, number density, and acoustic impedance properties on the observed level of backscatter from tissue (Insana *et al.*, 1990; Lizzi *et al.*, 1983; Rose *et al.*, 1995).

Furthermore, Salih et al. (2004) showed that the right-ventricular myocardium contains a higher percentage of collagen than the left-ventricular myocardium. Hoyt et al. (1984) demonstrated that in mature human and canine hearts both the integrated backscatter and the amount of collagen present were larger in the right ventricle than the left ventricle.

The results of our measurements appear consistent with these previous studies describing significant differences between left and right ventricular characteristics during fetal and postnatal development. The existence of a difference in the left and right ventricular myoarchitecture in the developing heart is an important observation because both ventricles are exposed to similar prenatal loading conditions, which represent important determinants of ventricular geometry. This suggests that intrinsic myocardial properties of the two ventricles may be genetically programmed differently during the heart development. These high-frequency ultrasonic measurements of excised fetal hearts permit an assessment of the myoarchitecture and intrinsic properties of the developing heart and their potential effects on fetal echocardiography. Although these measurements obtained at 50 MHz are well beyond the frequencies used clinically and the specific interactions of ultrasound with the myocardium may be different at higher frequencies compared with lower frequencies, the influence of the regional variations in acoustic properties discernable at high frequencies may well affect features observed in clinical fetal echocardiographic imaging and permit an enhanced interpretation of the in vivo examinations of the fetal heart. Previous studies from our laboratory suggest many features of myocardial backscatter observed at

lower frequencies (e.g., anisotropy of backscatter) (Hoffmeister *et al.*, 1995; Mottley and Miller, 1988) are observed at higher frequencies as well (Bridal *et al.*, 1993; Hall *et al.*, 2000c). Knowledge of the intrinsic properties of the fetal heart may permit researchers and clinicians to more accurately identify abnormalities of the myocardium earlier than they are currently identified.

2.7 Limitations

One potential limitation of the current study was that measurements were performed on formalin-fixed specimens at room temperature. This approach was necessary due to the length of time required to acquire the ultrasonic measurements. Although measurements using fresh tissue would be desirable, these were not feasible due to concerns regarding tissue degradation over the length of time required for data acquisition (hours). Although fixation does affect absolute values of ultrasonically measured quantities (Baldwin *et al.*, 2005d; Hall *et al.*, 2000a; Takiuchi *et al.*, 2001), the backscatter measurements performed in this study focused on relative properties of the heart (e.g., left-ventricular and right-ventricular myocardium). These relative differences are expected to be largely preserved in fixed myocardium.

Another concern is the placement of the region of interest within the myocardium for intrinsic apparent integrated backscatter measurements. Previously published literature has shown the dependence of velocity, attenuation, and backscatter on the angle of insonification relative to the myofiber direction (Baldwin *et al.*, 2005c;

Hoffmeister *et al.*, 1995; Mottley and Miller, 1988, 1990; Verdonk *et al.*, 1992, 1996; Yang *et al.*, 2006). We chose to place the regions of interest within the brightest bands of the ventricular free walls in order to minimize the effects of myocardial anisotropy. These bright bands represent regions primarily perpendicular to the direction of insonification, as validated by histological analysis. However, it is possible that the regions of interest may contain a modest range of myofibers whose direction was not strictly perpendicular to the incoming ultrasonic beam.

2.8 Summary

Results of this study show that the measured apparent integrated backscatter values demonstrate significant transmural variation in the ventricular myocardium with the largest levels of apparent integrated backscatter located in the mid-myocardium of the left-ventricular free wall and within the subepicardium in the right-ventricular free wall. These different levels of apparent integrated backscatter correspond to the anisotropy of the fiber orientation seen in histological analyses. Comparisons of signals backscattered at perpendicular incidence to the myofibers from the ventricular free walls indicate that the level of backscatter from the right ventricular myocardium is greater than that of the left ventricular myocardium in fetuses. This result is consistent with previous studies in mature hearts (Hoyt *et al.*, 1984) and with published studies showing differences in developing hearts (Salih *et al.*, 2004; Smolich *et al.*, 1989).

We speculate that the left and right ventricles of the fetal heart follow a biogenetically predetermined trajectory of growth and development, which can be altered by the intrauterine environment (e.g. nutritional deprivation or excess hormonal exposure). This altered environment can result in an altered trajectory of the developing heart that can permanently change cardiovascular structure and physiology (Barker, 1995; Lucas, 1991). In this context, our method of evaluation of myoarchitectural properties may discern prenatally the cardiac changes with consequential long-term postnatal effects.

Our research suggests that the intrinsic properties of the left and right ventricular myocardium are distinct in fetal pig hearts at mid-gestation. Apparent integrated backscatter may offer a method for assessing changes of fetal hearts due to primary cardiac defects and secondary adaptive changes.

2.9 Acknowledgment

We would like to thank Dr. Joe Lennerz and Dr. Frances V. White, Department of Pathology and Immunology, Washington University School of Medicine, for the preparation and interpretation of the histology specimens.

Bibliography

Aygen, M. and Popp, R. L. (**1987**). "Influence of the orientation of myocardial fibers on echocardiographic images", Am J Cardiol **60**, 147–152.

Baldwin, S. L., Holland, M. R., Sosnovik, D. E., and Miller, J. G. (**2005**a). "Effects of region-of-interest length on estimates of myocardial ultrasonic attenuation and backscatter", Med Phys **32**, 418–26.

Baldwin, S. L., Marutyan, K. R., Yang, M., Wallace, K. D., Holland, M. R., and Miller, J. G. (**2005**b). "Estimating myocardial attenuation from M-mode ultrasonic backscatter", Ultrasound Med Biol **31**, 477–84.

Baldwin, S. L., Yang, M., Marutyan, K. R., Wallace, K. D., Holland, M. R., and Miller, J. G. (**2005**c). "Measurements of the anisotropy of ultrasonic velocity in freshly excised and formalin-fixed myocardial tissue", J Acoust Soc Am **118**, 505–513.

Baldwin, S. L., Yang, M., Marutyan, K. R., Wallace, K. D., Holland, M. R., and Miller, J. G. (**2005**d). "Ultrasonic detection of the anisotropy of protein cross-linking in myocardium", IEEE Ultrason Symp 2263–2266.

Barker, D. J. (**1995**). "Fetal origins of coronary heart disease", BMJ **311**, 171–4.

Bridal, S. L., Recchia, D., Miller, J. G., and Wickline, S. A. (**1993**). "Anisotropy of apparent integrated backscatter, signal loss, and backscatter coefficient at 30 to 45 MHz in canine papillary muscle", Ultrasonic Imaging **15**, 155–156.

Davison, G., Hall, C. S., Miller, J. G., Scott, M., and Wickline, S. A. (**1995**). "Ultrasonic tissue characterization of end-stage dilated cardiomyopathy", Ultrasound Med Biol **21**, 853–60.

Hall, C. S., Dent, C. L., Scott, M. J., and Wickline, S. A. (**2000**a). "High-frequency ultrasound detection of the temporal evolution of protein cross linking in myocardial tissue", IEEE Trans Ultrason Ferroelec Freq Control **47**, 1051–1058.

Hall, C. S., Nguyen, C. T., Scott, M. J., Lanza, G. M., and Wickline, S. A. (**2000**b). "Delineation of the extracellular determinants of ultrasonic scattering from elastic arteries", Ultrasound Med Biol **26**, 613–20.

Hall, C. S., Scott, M. J., Lanza, G. M., Miller, J. G., and Wickline, S. A. (**2000**c). "The extracellular matrix is an important source of ultrasound backscatter from myocardium", J Acoust Soc Am **107**, 612–9.

Hall, C. S., Verdonk, E. D., Wickline, S. A., Perez, J. E., and Miller, J. G. (**1997**). "Anisotropy of the apparent frequency dependence of backscatter in formalin fixed human myocardium", J. Acoust. Soc. Am. **101**, 563–568.

Hoffmeister, B. K., Handley, S. M., Wickline, S. A., and Miller, J. G. (**1996**). "Ultrasonic determination of the anisotropy of Young's modulus of fixed tendon and fixed myocardium", J. Acoust. Soc. Am. **100**, 3933–3940.

Hoffmeister, B. K., Verdonk, E. D., Wickline, S. A., and Miller, J. G. (**1994**). "Effect of collagen on the anisotropy of quasi-longitudinal mode ultrasonic velocity in fibrous soft tissues: A comparison of fixed tendon and fixed myocardium", J. Acoust. Soc. Am. **96**, 1957–1964.

Hoffmeister, B. K., Wong, A. K., Verdonk, E. D., Wickline, S. A., and Miller, J. G. (**1995**). "Comparison of the anisotropy of apparent integrated ultrasonic backscatter from fixed human tendon and fixed human myocardium", J. Acoust. Soc. Am. **97**, 1307–1313.

Holland, M. R., Kovacs, A., Posdamer, S. H., Wallace, K. D., and Miller, J. G. (**2005**). "Anisotropy of apparent backscatter in the short-axis view of mouse hearts", Ultrasound Med Biol **31**, 1623–1629.

Holland, M. R., Wilkenshoff, U. M., Finch-Johnston, A. E., Handley, S. M., Perez, J. E., and Miller, J. G. (**1998**). "Effects of myocardial fiber orientation in echocardiography: Quantitative measurements and computer simulation of the regional dependence of backscattered ultrasound in the parasternal short-axis view", J Am Soc Echocardiogr **11**, 929–937.

Hoyt, R., Skorton, D. J., Collins, S. M., and Melton, H. E., J. (**1984**). "Ultrasonic backscatter and collagen in normal ventricular myocardium", Circulation **69**, 775–82.

Hoyt, R. H., Collins, S. M., Skorton, D. J., Ericksen, E. E., and Conyers, D. (**1985**). "Assessment of fibrosis in infarcted human hearts by analysis of ultrasonic backscatter", Circulation **71**, 740–4.

Insana, M. F., Wagner, R. F., Brown, D. G., and Hall, T. J. (**1990**). "Describing small-scale structure in random media using pulse-echo ultrasound", J Acoust Soc Am **87**, 179–92.

Kumar, K. N. and Mottley, J. G. (**1994**). "Quantitative modeling of the anisotropy of ultrasonic backscatter from canine myocardium", IEEE Trans Ultrason Ferroelectr Freq Control **41**, 441–450.

Lizzi, F. L., Greenebaum, M., Feleppa, E. J., Elbaum, M., and Coleman, D. J. (**1983**). "Theoretical framework for spectrum analysis in ultrasonic tissue characterization", J Acoust Soc Am **73**, 1366–73.

Lucas, A. (**1991**). "Programming by early nutrition in man", Ciba Found Symp **156**, 38–50; discussion 50–5.

Madaras, E., Perez, J., Sobel, B., Mottley, J., and Miller, J. (**1988**). "Anisotropy of the ultrasonic backscatter of myocardial tissue: II. Measurements in vivo", J. Acoust. Soc. Am. **83**, 762–769.

Mimbs, J., O'Donnell, M., Bauwens, D., Miller, J., and Sobel, B. (**1980**). "The dependence of ultrasonic attenuation and backscatter on collagen content in dog and rabbit hearts", Circ Res **47**, 49–58.

Mimbs, J. W., O'Donnell, M., Miller, J. G., and Sobel, B. E. (**1981**). "Detection of cardiomyopathic changes induced by doxorubicin based on quantitative analysis of ultrasonic backscatter", Am J Cardiol **47**, 1056–60.

Mottley, J. G. and Miller, J. (**1988**). "Anisotropy of the ultrasonic backscatter of myocardial tissue: I. Theory and measurements in vitro", J. Acoust. Soc. Am. **83**, 755–761.

Mottley, J. G. and Miller, J. G. (**1990**). "Anisotropy of the ultrasonic attenuation in soft tissues: Measurements in vitro", J. Acoust. Soc. Am. **88**, 1203–1210.

Nguyen, C. T., Hall, C. S., Scott, M. J., Zhu, Q., Marsh, J., and Wickline, S. A. (**2001**). "Age-related alterations of cardiac tissue microstructure and material properties in Fischer 344 rats", Ultrasound Med Biol **27**, 611–9.

O'Brien, William D., J., Sagar, K. B., Warltier, D. C., and Rhyne, T. L. (**1995**a). "Acoustic propagation properties of normal, stunned, and infarcted myocardium: Morphological and biochemical determinants", Circulation **91**, 154–160.

O'Brien, P. D., O'Brien, W. D., J., Rhyne, T. L., Warltier, D. C., and Sagar, K. B. (**1995**b). "Relation of ultrasonic backscatter and acoustic propagation properties to myofibrillar length and myocardial thickness", Circulation **91**, 171–5.

O'Donnell, M., Mimbs, J. W., and Miller, J. G. (**1981**). "Relationship between collagen and ultrasonic backscatter in myocardial tissue", J Acoust Soc Am **69**, 580–8.

Perez, J. E., Barzilai, B., Madaras, E. I., Glueck, R. M., Saffitz, J. E., Johnston, P., Miller, J. G., and Sobel, B. E. (**1984**). "Applicability of ultrasonic tissue characterization for longitudinal assessment and differentiation of calcification and fibrosis in cardiomyopathy", J Am Coll Cardiol **4**, 88–95.

Perles, Z., Nir, A., Gavri, S., and Rein, A. J. (**2007**). "Assessment of fetal myocardial performance using myocardial deformation analysis", Am J Cardiol **99**, 993–6.

Pohlhammer, J. and O'Brien, W. D., J. (**1981**). "Dependence of the ultrasonic scatter coefficient on collagen concentration in mammalian tissues", J Acoust Soc Am **69**, 283–5.

Recchia, D., Miller, J. G., and Wickline, S. A. (**1993**). "Quantification of ultrasonic anisotropy in normal myocardium with lateral gain compensation of two-dimensional integrated backscatter images", Ultrasound Med Biol **19**, 497–505.

Rose, J. H., Kaufmann, M. R., Wickline, S. A., Hall, C. S., and Miller, J. G. (**1995**). "A proposed microscopic elastic wave theory for ultrasonic backscatter from myocardial tissue", J Acoust Soc Am **97**, 656–68.

Salih, C., McCarthy, K., and Ho, S. Y. (**2004**). "The fibrous matrix of ventricular myocardium in hypoplastic left heart syndrome: A quantitative and qualitative analysis", Ann Thorac Surg **77**, 36–40.

Sanchez-Quintana, D., Garcia-Martinez, V., Climent, V., and Hurle, J. (**1995**). "Morphological changes in the normal pattern of ventricular myoarchitecture in the developing human heart", Anat Rec **243**, 483–495.

Smolich, J. J., Walker, A. M., Campbell, G. R., and Adamson, T. M. (**1989**). "Left and right ventricular myocardial morphometry in fetal, neonatal, and adult sheep", Am J Physiol **257**, H1–9.

Sosnovik, D. E., Baldwin, S. L., Holland, M. R., and Miller, J. G. (**2001**). "Transmural variation of myocardial attenuation and its potential effect on contrast-mediated estimates of regional myocardial perfusion", J Am Soc Echocardiogr **14**, 782–8.

Takiuchi, S., Marsh, J. N., Hall, C. S., Lanza, G. M., and Wickline, S. A. (**2001**). "Unexpected anisotropic behavior of ultrasound attenuation after collagen cross-linking in porcine tendons", in *IEEE Ultrason Symp*, volume 2, 1253–1256.

Verdonk, E. D., Hoffmeister, B. K., Wickline, S. A., and Miller, J. G. (**1996**). "Anisotropy of the slope of ultrasonic attenuation in formalin fixed human myocardium", J. Acoust. Soc. Am. **99**, 3837–3843.

Verdonk, E. D., Wickline, S. A., and Miller, J. G. (**1992**). "Anisotropy of ultrasonic velocity and elastic properties in normal human myocardium", J. Acoust. Soc. Am. **92**, 3039–3050.

Wear, K. A., Milunski, M. R., Wickline, S. A., Perez, J. E., Sobel, B. E., and Miller, J. G. (**1989**). "Differentiation between acutely ischemic myocardium and zones of completed infarction in dogs on the basis of frequency-dependent backscatter", J Acoust Soc Am **85**, 2634–2641.

Wickline, S. A., Thomas, L. J., r., Miller, J. G., Sobel, B. E., and Perez, J. E. (**1985**). "A relationship between ultrasonic integrated backscatter and myocardial contractile function", J Clin Invest **76**, 2151–60.

Wickline, S. A., Verdonk, E. D., Sobel, B. E., and Miller, J. G. (**1992**). "Identification of human myocardial infarction in vitro based on the frequency dependence of ultrasonic backscatter", J Acoust Soc Am **91**, 3018–25.

Wong, A. K., Osborn, T. G., Miller, J. G., and Wickline, S. A. (**1993**). "Quantification of ventricular remodeling in the tight-skin mouse cardiomyopathy with acoustic microscopy", Ultrasound Med Biol **19**, 365–74.

Wong, A. K., Verdonk, E. D., Hoffmeister, B. K., Miller, J. G., and Wickline, S. A. (**1992**). "Detection of unique transmural architecture of human idiopathic cardiomyopathy by ultrasonic tissue characterization", Circulation **86**, 1108–1115.

Wrathall, A., Bailey, J., and Hebert, C. (**1974**). "A radiographic study of development of appendicular skeleton in the fetal pig", Res Vet Sci **17**, 154–168.

Yang, M., Baldwin, S. L., Marutyan, K. R., Wallace, K. D., Holland, M. R., and Miller, J. G. (**2006**). "Elastic stiffness coefficients (c11, c33, and c13) for freshly excised and formalin-fixed myocardium from ultrasonic velocity measurements", J Acoust Soc Am **119**, 1880–1887.

Chapter 3

Measurements of Ultrasonic Attenuation Properties

3.1 Preface

This chapter is based on the peer-reviewed journal article *Measurements of Ultrasonic Attenuation Properties of Mid-Gestational Fetal Pig Hearts* written by Allyson A. Gibson, Gautam K. Singh, Joseph J. Hoffman, Achiau Ludomirsky, Mark R. Holland and published in *Ultrasound in Medicine & Biology, Vol. 35, No. 2, pp. 319-328, 2009.*

3.2 Abstract

The objectives of this study were to measure the relative attenuation properties of the left and right ventricles in fetal pig hearts and to compare the spatial variation in attenuation measurements with those observed in Chapter 2. Approximately 1.0 mm thick, short-axis slices of excised, formalin-fixed heart were examined from 15 mid-gestational fetal pigs using a 50-MHz single-element transducer. Measurements of the attenuation properties demonstrate regional differences in the left and right ventricular myocardium that appear consistent with the previously reported regional differences in apparent integrated backscatter measurements of the same fetal pig hearts. For regions of perpendicular insonification relative to the myofiber orientation, the right ventricular free wall showed larger values for the slope of the attenuation coefficient from 30-60 MHz (1.48 ± 0.22 dB/(cm·MHz) [mean ± standard deviation]) and attenuation coefficient at 45 MHz (46.3 ± 7.3 dB/cm [mean ± SD]) than the left ventricular free wall (1.18 ± 0.24 dB/(cm·MHz) and 37.0 ± 7.9 dB/cm [mean ± SD]) for slope of attenuation coefficient and attenuation coefficient at 45 MHz, respectively). This attenuation study supports the hypothesis that intrinsic differences in the myocardium of the left and right ventricles exist in fetal pig hearts at mid-gestation.

3.3 Introduction

Echocardiographic assessment of the developing fetal heart is becoming an important component of overall prenatal care. The ability to characterize intrinsic features of the developing myocardium may aid researchers and clinicians in identifying those fetuses most at risk for developing congenital heart defects, myopathies, or altered myocardial function due to an adverse intrauterine environment. Observed characteristics of fetal echocardiographic images are significantly dependent upon the inherent ultrasonic properties of the developing myocardium. Observed images of the heart depend upon the combined contributions of both the intrinsic ultrasonic backscatter and attenuation properties of myocardium (Holland *et al.*, 1998, 2005). These ultrasonic properties are largely determined by the detailed viscoelastic and structural properties of myocardial tissue (Insana *et al.*, 1990; Lizzi *et al.*, 1987; O'Brien *et al.*, 1995; O'Donnell *et al.*, 1979, 1981; Oelze *et al.*, 2002; Rose *et al.*, 1995). Hence, a better understanding of the inherent ultrasonic properties of the developing myocardium and their spatial variation may provide new insights into the development of enhanced echocardiography-based methods to assess heart development and aid in prenatal diagnoses of altered growth trajectories.

In Chapter 2, we reported measurements of the apparent integrated backscatter properties of excised mid-gestational fetal pig hearts. This study showed distinct patterns of backscatter in the left and right ventricular free walls that appeared to correlate with the ventricular myoarchitecture associated with the two sides. For

ultrasonic insonficiation perpendicular to the transverse plane of the heart, at the mid-papillary level, the largest level of backscatter in the left ventricular free wall was located within the mid-myocardium and regions of decreased apparent backscatter were located subepicardially and subendocardially. The right ventricular free wall showed the largest level of apparent backscatter in a subepicardial band with less apparent backscatter measured in the subendocardial region. Histological analyses of the ultrasonically imaged fetal pig hearts demonstrated the regions of largest backscatter in the ventricular free walls were areas corresponding to perpendicular insonification relative to the circular myofiber orientation. Regions of the ventricular free wall where the predominant myofiber direction was not perpendicular to the ultrasonic beam exhibited smaller levels of backscatter. Furthermore, for those regions of perpendicular insonification relative to the myofiber orientation, it was seen that the level of apparent integrated backscatter for the right ventricular myocardium was larger than that for the left ventricular myocardium. The objectives of the study reported in this chapter are to extend the ultrasonic characterization of fetal hearts by measuring the relative attenuation properties of the fetal myocardium and to compare these attenuation measurements with the apparent backscatter measurements.

Our approach was to investigate excised formalin-fixed, mid-gestational fetal pig heart specimens by measuring the ultrasonic properties from a thin slice of the heart. Mid-gestational fetal pig hearts were chosen for this study because the gross structural formation of the heart is complete by this time point, and fetal pigs of this gestational age are similar in gestational age to human fetuses referred for routine diagnostic fetal

echocardiographic evaluation at fetal cardiology clinics of other institutions and our center at St. Louis Children's Hospital. The measurements performed in this study focus on the relative attenuation properties of the left ventricular and right ventricular myocardium. Although formalin fixation can affect the absolute level of attenuation and backscatter parameters (Baldwin *et al.*, 2005b; Bamber *et al.*, 1979; Hall *et al.*, 2000a; Takiuchi *et al.*, 2001; van der Steen *et al.*, 1991) the relative differences should be largely preserved.

3.4 Methods

3.4.1 Preparation of specimens

Fifteen mid-gestational, formalin-fixed fetal pigs were obtained from Nebraska Scientific Inc. (Omaha, NE, USA) in compliance with approved procedures established by the Animal Studies Committee at Washington University in St. Louis. The heart and humerus bone were harvested from each of the fetal pigs and placed in 10% formalin solution. Thin (approximately 1.0 mm) flat and parallel short-axis cross-sectional specimens of the fetal hearts, representing a transverse plane perpendicular to the long axis of the heart at the mid-papillary level, were prepared using a previously described method in Section 2.4.1 of Chapter 2. The gestational age of each fetal pig was estimated from the length of the humerus bone using a previously described approach (Wrathall *et al.*, 1974). In our study the estimated age of the 15 fetal pigs was 57 ± 3 days (mean $\pm$ standard deviation), representing approximately half of the

gestational age of a pig (full gestation of a pig is ∼120 days).

3.4.2 Acquisition of ultrasonic attenuation data

Measurements of the ultrasonic attenuation properties of the excised fetal heart specimens were obtained using a shadowed-reflector method (Ophir *et al.*, 1984; Verdonk *et al.*, 1996). In this approach, the approximately 1.0 mm-thick fetal heart specimens were mounted on a stainless-steel plate and placed in a custom-designed and constructed water tank. A broadband, 50-MHz center frequency, single-element transducer (6.35 mm diameter, 12.7 mm focus, Panametrics V390; Panametrics Inc., Waltham, MA, USA) with a nominal 60 μm beam width was used to insonify the specimens and measure the specular reflection from the shadowed surface of the stainless-steel plate. The angle of insonification was perpendicular to the cut face of the myocardial slice such that the ultrasonic wave propagated through the entire thickness of each specimen twice. Figure 3.1 shows a block diagram illustrating the experimental setup and the orientation of the transducer with respect to the myocardial slice. The transducer was used in pulse-echo mode, and data were acquired over the entire specimen, by translating the transmitting /receiving transducer in a C-scan pattern using a Newport XPS motion controller (Newport Corp., Mountain View, CA, USA) in 50 μm steps. The vertical position of the transducer was adjusted to place the focus at the front face of the stainless-steel plate. A Panametrics 5900 pulser /receiver was used in conjunction with a Panametrics 5627RPP-1 remote pulser /preamplifier to drive the transmit of the Panametrics V390 50-MHz transducer and

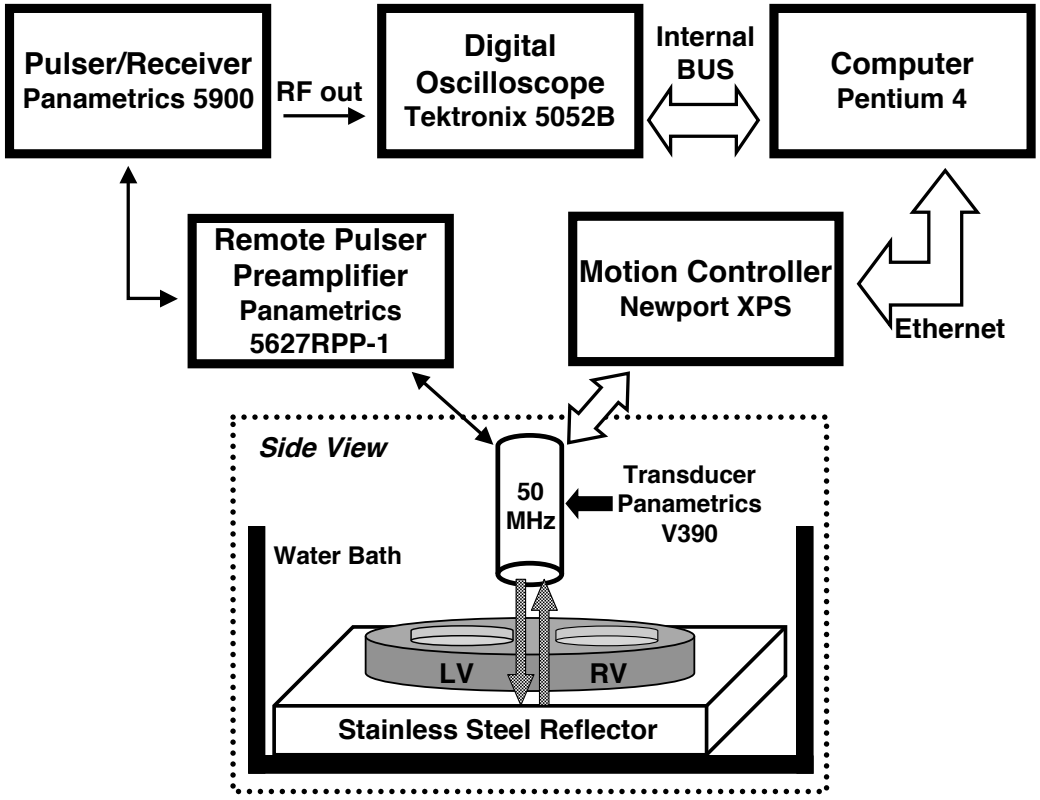

FIGURE 3.1: Block diagram illustrating the experimental setup. The 50-MHz transducer scans the excised heart specimen in a C-scan format. LV=left ventricle; RV=right ventricle

preamplify the reflected signal from the surface of the shadowed stainless-steel plate. The shadowed reflector signal from each interrogated myocardial site was digitized at 625 megasamples-per-second, signal averaged 64 times, and stored as a 2500-point record using a Tektronix 5052B digital oscilloscope with 8-bit digitization (Tektronix Inc., Beaverton, OR, USA). In addition to the tissue-shadowed reflected signals, unshadowed specular reflections from the stainless-steel plate were acquired as reference signals using the same acquisition parameters.

3.4.3 Data Analyses

Each radio-frequency (RF) signal acquired was gated using a 0.67 μs long Tukey window centered on the reflection off the stainless-steel plate. Contributions to the measured signal arising from myocardial backscatter within the gate were small compared to the specularly-reflected signal from the stainless-steel plate and did not significantly affect the measurements. At each site, the power spectrum was calculated from the gated waveform using a fast Fourier transform and the same algorithm was performed on the water-path-only reference signal from the steel plate.

The power spectrum $P_{reference}(f)$ of the received reference signal can be expressed as

$$P_{reference}(f) = P_0(f) \cdot E_0(f)^2 \cdot (D_{host}(f)) \cdot [exp(-\alpha_{host}(f) \cdot 2L)]^2 \cdot (R^{Intensity}_{host \rightarrow reflector}) \quad (3.1)$$

where $P_0(f)$ is the transmitted power spectrum, $E_0(f)$ is the frequency response of the transducer and associated electronics, $D_{host}(f)$ is the diffraction effects in the host medium (water), $\alpha_{host}(f)$ is the frequency dependent attenuation coefficient of the water, L represents the distance from the transducer to the stainless-steel plate, and R is the intensity reflection coefficient at the surface of the stainless-steel reflector. Similarly the received power spectrum, $P_{specimen}(f)$ of the reflector shadowed by the

specimen can be written as

$$P_{specimen}(f) = P_0(f) \cdot E_0(f)^2 \cdot (D_{specimen}(f)) \cdot [exp(-\alpha_{host}(f) \cdot 2(L-l))]^2 \cdot [exp(-\alpha_{specimen}(f) \cdot 2l]^2 \cdot (T^{Intensity}_{host \rightarrow specimen}) \cdot (R^{Intensity}_{host \rightarrow reflector}) \cdot (T^{Intensity}_{specimen \rightarrow host}) \quad (3.2)$$

in which $D_{specimen}(f)$ is the diffraction effects in the path including the host and specimen, l represents the specimen thickness, $\alpha_{specimen}(f)$ is the frequency dependent attenuation coefficient of the specimen, and T represents the intensity transmission coefficients at the interface between the host medium and specimen. Figure 3.2a shows representative logarithmic power spectra corresponding to a reference signal and specimen signal for one site within the specimen.

A ratio of the linear reference power spectrum (Equation 3.1) and linear specimen power spectrum (Equation 3.2) is then used to calculate the total signal loss (TSL) and compensate for the frequency response of the transducer and associated electronics.

$$TSL = \frac{P_{reference}(f)}{P_{specimen}(f)} = [exp(\alpha_{specimen}(f) - \alpha_{host}(f)) \cdot 2l]^2 \cdot \left[\frac{R^{Intensity}_{host \rightarrow reflector}}{(T^{Intensity}_{host \rightarrow specimen}) \cdot (R^{Intensity}_{specimen \rightarrow reflector}) \cdot (T^{Intensity}_{specimen \rightarrow host})} \right] \quad (3.3)$$

The total signal loss has contributions arising from the reflection and transmission losses at the water, tissue and stainless-steel interfaces as well as the losses associated with the intrinsic attenuation properties of myocardial tissue. The effects of diffraction are not explicitly stated in the expression for the total signal loss

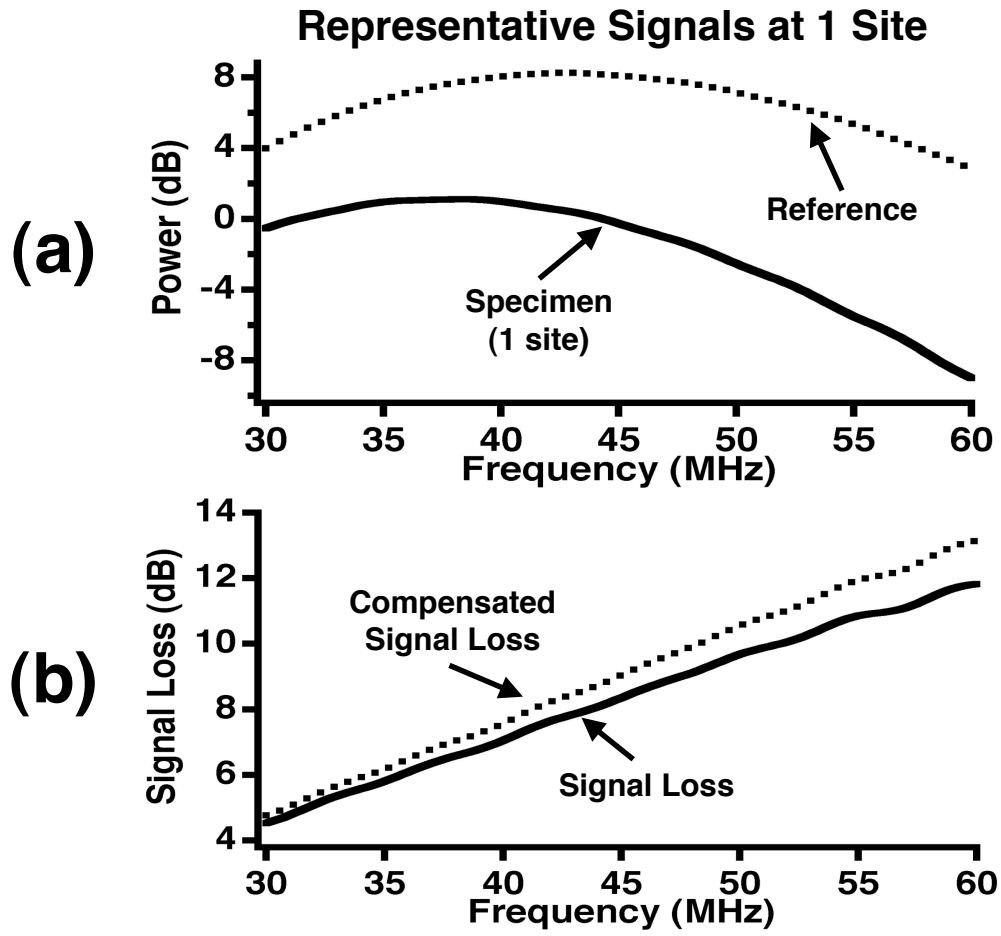

FIGURE 3.2: (a) Representative power spectra for a reference signal and specimen signal at one site. (b) A representative signal loss curve and signal loss compensated for transmission and reflection effects and the attenuation effect of water at high frequencies.

because of the similarity of the velocity of sound in water and myocardium. Furthermore, because the experiment is performed at 50 MHz, the attenuation coefficient of water, the host medium, cannot be neglected. At the experimental temperature of 24°C, the frequency dependent attenuation coefficient of water was taken to be $\alpha_{host}(f) = 0.00022 \cdot f^2(\text{cm}^{-1}\text{MHz}^{-2})$ where f is the frequency in MHz (AIUM, 1992).

By rearranging Equation 3.3 and converting to logarithmic units, the compensated signal loss is written as

$$\alpha_{specimen,dB}(f) \cdot 2l = 10log(P_{reference}) - 10log(P_{specimen}) + \alpha_{host,dB}(f) \cdot 2l - 10log\left[\frac{R^{Intensity}_{host \rightarrow reflector}}{(T^{Intensity}_{host \rightarrow specimen}) \cdot (R^{Intensity}_{specimen \rightarrow reflector}) \cdot (T^{Intensity}_{specimen \rightarrow host})}\right] \quad (3.4)$$

where $\alpha_{specimen,dB}(f)$ and $\alpha_{host,dB}(f)$ are expressed in units of dB/cm and the signal loss due to water (host) is added to the reflection and transmission losses. The reflection and transmission coefficients were calculated based on the acoustic impedance values (MKS units) of stainless steel (45.4 MRayl), water (1.46 MRayl), and fixed myocardium (1.67 MRayl) (Baldwin *et al.*, 2005a; Yang *et al.*, 2006). The value for the acoustic impedance of myocardium was derived from density and speed of sound measurements of fixed ovine myocardium at lower frequencies. However, we anticipate the potential difference in the acoustic impedance for the two species and two frequency ranges should have minimal effects on the reported results. Figure 3.2b displays representative total signal loss and compensated signal loss curves for one site. After these compensations were applied to the measured signal loss, the attenuation coefficient as a function of frequency was determined by dividing by twice

the thickness of the tissue. The tissue thickness was determined with the micrometer that was mounted on the custom-designed cutting tool shown in Figure 2.1.

The compensated attenuation coefficient was further analyzed to determine the attenuation coefficient at a specific frequency and the frequency dependence of the attenuation coefficient over the bandwidth of the transducer. A line was fit to the compensated attenuation coefficient data over the useful 6 dB bandwidth of 30 MHz to 60 MHz. From this best-fit line the slope of attenuation coefficient and attenuation coefficient at 45 MHz were recorded for each site interrogated. This algorithm was applied to every shadowed reflector RF signal obtained to form images of the entire fetal pig heart slice. Images of the attenuation properties were created by mapping the attenuation measurements to grayscale values and displaying them as pixels in either a slope of attenuation coefficient from 30-60 MHz image or an attenuation coefficient at 45 MHz image. Figure 3.3a displays a representative slope of attenuation image for one of the fetal pig hearts. All data analysis was performed using Igor Pro (WaveMetrics Inc., Portland, OR, USA) on a PowerBook G4 (Apple Inc., Cupertino, CA, USA).

3.4.4 Measurement of attenuation properties from the left ventricular and right ventricular free walls

To compare the attenuation properties of the left ventricular myocardium with those of the right, measurements were obtained from regions of perpendicular insoni-

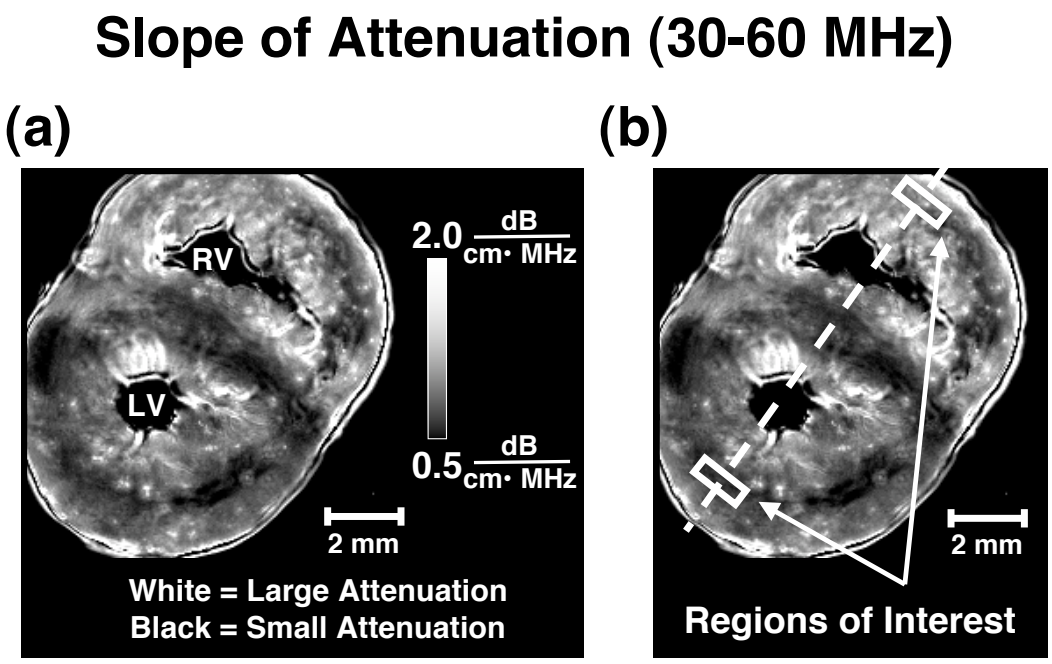

FIGURE 3.3: (a) Representative slope of attenuation image of a fetal pig heart with bright pixels representing relatively large values for slope of attenuation and dark pixels representing small values for slope of attenuation (range 0.5 to 2.0 dB/(cm·MHz)). LV=left ventricle; RV=right ventricle (b) An illustration of the bisecting line used for line profile analysis and locations of the regions of interest in a representative slope of attenuation image.

fication relative to the predominant myofiber orientation based on previous analyses of the backscatter data in Chapter 2. These specific regions of interest were chosen to reduce the confounding effects of tissue anisotropy on the ultrasonic measurements and enable assessment of other intrinsic properties of the tissue. Figure 3.3b illustrates the placement of the regions of interest on a representative slope of attenuation image.

The regions of interest used for analyses in each attenuation image were similar in

size, shape, and placement as those regions used in Chapter 2. Each region of interest was centered on a line bisecting the ventricular free walls and septum. The size of the region of interest was uniform within each individual heart, but varied between different hearts depending on the transmural dimension of the regions of perpendicular insonification, as validated by histology. The average area for the regions of interest was 0.533 mm^2. The regions were always chosen to be small enough to cover only the band of perpendicular insonification, but large enough to provide reasonable spatial averaging of measured values. Because the fetal hearts were not repositioned between acquisitions of backscatter and attenuation data, each region of interest was drawn on the backscatter images and copied onto the attenuation images to ensure the same myocardial regions were compared for each heart.

3.5 Results

3.5.1 Regional Variation of Attenuation Properties

Parametric images generated from measurements of the slope of the attenuation coefficient from 30-60 MHz and attenuation coefficient at 45 MHz illustrate distinct patterns of attenuation in the left and right ventricular myocardium for all 15 specimens investigated. These spatial variations in attenuation properties are consistent with those reported in Chapter 2 for apparent integrated backscatter values and are further examined in the Discussion section of this chapter (Section 3.6). The attenuation images show distinctly different patterns of values in the left and right ventricu-

lar myocardium implying distinct ventricular myoarchitecture and properties between the two sides. In these images the darkest levels, representing relatively small attenuation coefficient or small slope of attenuation coefficient values, are located in the mid-myocardium of left ventricles and brighter regions (higher attenuation coefficient or slope of attenuation coefficient) are located in the subepicardium and subendocardium. Values range from approximately 0.5 dB/(cm·MHz) to 1.5 dB/(cm·MHz) for slope of attenuation coefficient (20 to 60 dB/cm for the attenuation coefficient at 45 MHz) in this region. In the right ventricular myocardium the regions with lower attenuation values were positioned more subepicardially with regions of higher attenuation values on the endocardial side of the ventricular free wall. Right ventricular values ranged from 1.0 dB/(cm·MHz) to 2.5 dB/(cm·MHz) for slope of attenuation coefficient and 40 to 70 dB/cm for the attenuation coefficient at 45 MHz in this region. Figure 3.3 shows representative patterns of attenuation for the left and right ventricular myocardium for one of the fetal hearts.

3.5.2 Comparison of attenuation properties

In general, the right ventricular myocardium of each ultrasonic attenuation image exhibits larger values of the slope of attenuation coefficient and the attenuation coefficient at 45 MHz than the left ventricular myocardium. Figure 3.4 shows the results of attenuation measurements from the left and right ventricular myocardium for regions of perpendicular insonification relative to the myofibers. This figure depicts a) measurements of the slope of attenuation coefficient from 30-60 MHz and b) the atten-

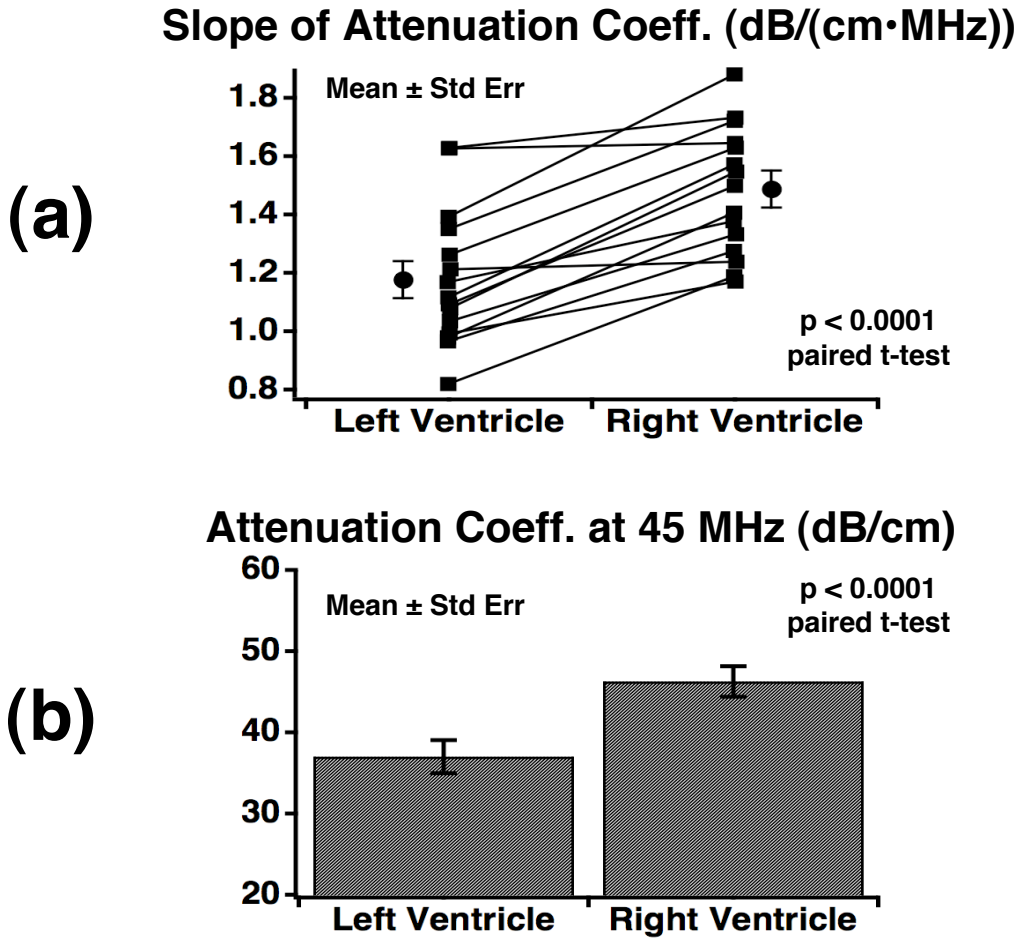

FIGURE 3.4: (a) Individual and mean ± standard error values (N=15) for the slope of attenuation coefficient from regions within the ventricular free walls with perpendicular insonification relative to the predominant myofiber orientation. (b) The mean and standard error (N=15) of the attenuation coefficient at 45 MHz from the left and right ventricular free walls where insonification is perpendicular to the predominant myofiber orienation.

uation coefficient at 45 MHz for the 15 fetal pig hearts along with the corresponding mean levels. In both sets of measurements, the right ventricular myocardium yields significantly larger values than the left ventricular myocardium, both for paired analyses within each specimen ($p < 0.0001$; paired t-test) as well as overall ($p < 0.005$; unpaired t-test; N=15). Specifically, the mean slope of attenuation coefficient over the experimental bandwidth was 1.48 ± 0.22 and 1.18 ± 0.24 dB/(cm·MHz) (mean $\pm$ standard deviation; $N = 15$; $p < 0.005$; unpaired t-test) from the myocardium of the right ventricle and left ventricle, respectively. The mean attenuation coefficient at 45 MHz was 46.3 ± 7.3 dB/cm for the right ventricular myocardium and 37.0 ± 7.9 dB/cm for the left ventricular myocardium (mean $\pm$ standard deviation; $N = 15$; $p < 0.005$; unpaired t-test) showing a 9.3 dB/cm difference between the two ventricles.

3.6 Discussion

Unlike mature adult hearts, both ventricles of fetal hearts are exposed to similar pressures that represent an important determinant of ventricular geometry. Despite the similar prenatal loading conditions, previous embryologic studies suggest the left and right ventricular myocardium develop differently (Salih *et al.*, 2004; Sanchez-Quintana *et al.*, 1995; Smolich *et al.*, 1989). These developmental differences lead to particular interest in quantifying the intrinsic differences in the left and right ventricular myoarchitecture and properties of the developing heart. Because the intrinsic composition and myofiber orientation of the heart can affect measured ultrasonic

properties and hence fetal echocardiographic imaging, our aim is to analyze the ultrasonic attenuation parameters and compare these to the reported backscatter results, as a means of characterizing the fetal myocardium.

High frequency analysis of the ventricular myocardium shows transmural variations in the attenuation properties of the heart that appear consistent with the variations observed in the backscatter data in Chapter 2. Grayscale images of the histology, apparent integrated backscatter values, slope of attenuation coefficient values, and attenuation coefficient at 45 MHz values are shown in Figure 3.5 for a representative fetal pig heart specimen. Both the backscatter and attenuation images display bands within the mid-myocardium of the left ventricular free wall and the subepicardial area of the right ventricular free wall that correspond to insonification perpendicular to the predominant myofiber orientation as validated by histology.

The three panels in Figure 3.6 depict mean transmural line profiles of the apparent integrated backscatter values and slope of attenuation coefficient values for the left ventricular free wall, septal wall, and right ventricular free wall, as well as a pictorial representation of the approximate location of each line profile for each heart investigated. The line profiles for each heart wall were generated by plotting the measured backscatter or attenuation values as a function of the percentage of wall thickness. Results from each specimen were averaged to produce the mean line profiles illustrated. The line profile data represents that corresponding to the bisecting line for each specimen as indicated in Figure 3.3b. The nature of the transmural line profiles depicted in Figure 3.6 appears consistent with what would be anticipated based on

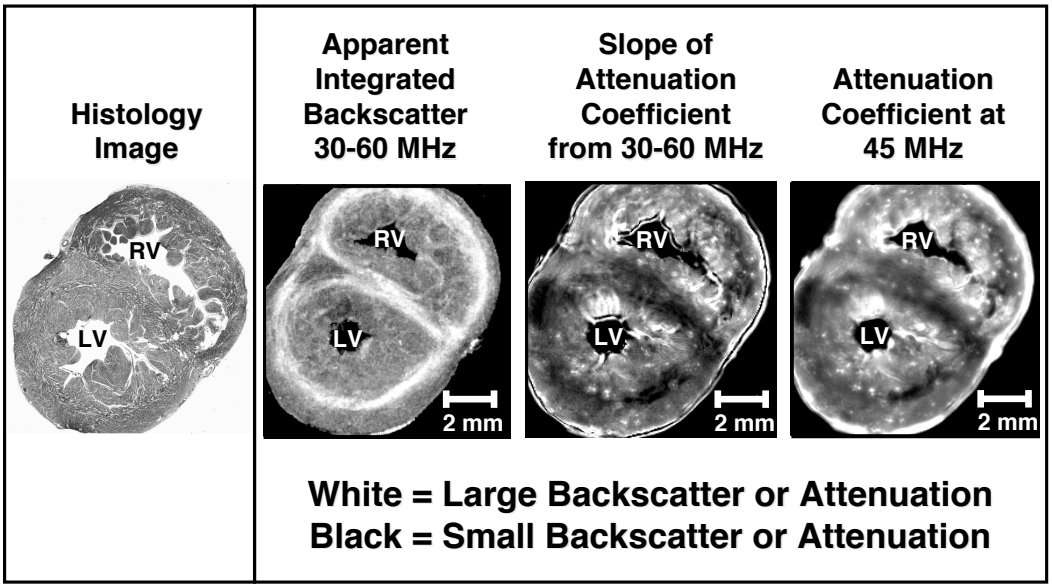

FIGURE 3.5: Histology, backscatter, and attenuation images from a representative fetal pig heart. White represents large apparent integrated backscatter values in the second image from the left and large values for slope of attenuation coefficient and attenuation coefficient at 45 MHz in the two right images, respectively. Black represents small values of apparent integrated backscatter in the second image and small slope of attenuation coefficient and attenuation coefficient at 45 MHz values in the two right images. LV=left ventricle; RV=right ventricle

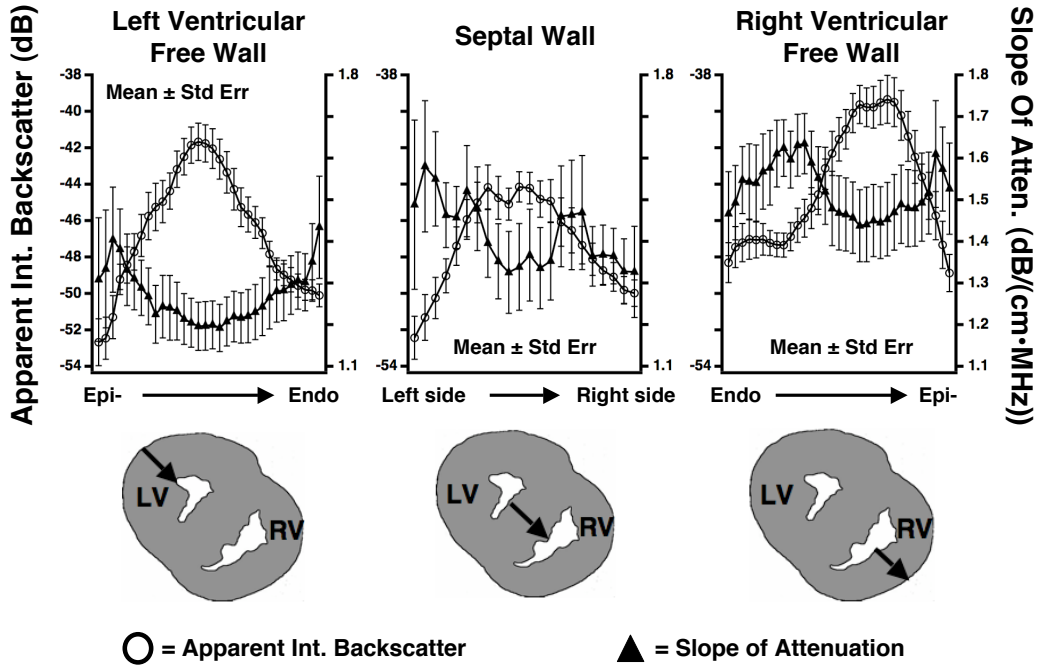

FIGURE 3.6: Mean ± standard error values of the apparent integrated backscatter (IBS) and slope of attenuation coefficient with respect to position within the left ventricular free wall, septal wall, and right ventricular free wall for 15 fetal pig heart specimens. The open circles represent average apparent integrated backscatter values and correspond to the left axes. The average slope of attenuation coefficient values are plotted using triangles and correspond to the right axes. Below the graphs are illustrations of the locations of the line profiles within the walls of the fetal pig hearts. LV=left ventricle; RV=right ventricle

previously published studies examining the effects of anisotropy on ultrasonic parameters (Baldwin *et al.*, 2006; Hall *et al.*, 1997; Hoffmeister *et al.*, 1995; Kumar and Mottley, 1994; Madaras *et al.*, 1988; Mottley and Miller, 1988, 1990; Sosnovik *et al.*, 2001; Verdonk *et al.*, 1996). Specifically, these studies demonstrated that maximum values of apparent backscatter with minimum levels of attenuation are associated with perpendicular insonification relative to the myofibers whereas, for non-perpendicular insonification larger levels of attenuation and smaller levels of apparent backscatter are observed. The measured line profiles demonstrate that the maximum apparent integrated backscatter values and slope of attenuation coefficient values are larger in the right ventricular free wall than the corresponding values in the left ventricular free wall.

Comparison of the values in these line profiles with the mean values for the slope of attenuation coefficient depicted in Figure 3.4 and the backscatter results reported in Chapter 2 demonstrate slight differences. This is a result of averaging the line profiles from the 15 individual hearts, each exhibiting slight variations in transmural myofiber orientation. Hence, the absolute ultrasonic values are somewhat muted by the influence of varying fiber orientation, and the detailed shape of the transmural line profiles may be influenced as well. On average these observed transmural variations of the acoustic properties of the left and right ventricular myocardium are consistent with previously published fiber architecture data. Sanchez-Quintanta et al. (1995) describe architecture of three layers (subepicardial, middle, subendocardial) in the left ventricular myocardium and a right ventricular fiber architecture consisting of

only two layers (subendocardial, subepicardial) for the prenatal and adult human hearts.

Additional insights regarding the intrinsic properties of fetal myocardium can be obtained by further analyses of those regions of perpendicular insonification within the ventricular free walls. A comparison of the ultrasonic measurements in the left and right ventricular regions show both the attenuation coefficient (and its frequency dependence) and the backscatter levels are larger in the right ventricular myocardium than in the left ventricular myocardium. Because the results from these regions (perpendicular insonification) diminish the effects of fiber orientation, these differences may imply compositional differences between the two ventricles. This observation is consistent with previously published data from mature hearts that demonstrate higher collagen content in the right ventricular myocardium compared to the myocardium of the left ventricle (Hoyt *et al.*, 1984, 1985). These studies also showed that an increase in myocardial collagen concentration correlates with an increase in both the measured ultrasonic attenuation and backscatter (Hall *et al.*, 2000b; Hoyt *et al.*, 1984, 1985; Mimbs *et al.*, 1980, 1981; Nguyen *et al.*, 2001; O'Donnell *et al.*, 1979, 1981; Perez *et al.*, 1984; Pohlhammer and O'Brien, 1981; Wear *et al.*, 1989; Wong *et al.*, 1993).

3.7 Clinical Implications

The results of these ultrasonic measurements of excised fetal hearts permit an assessment of the myoarchitecture and intrinsic properties of the developing heart. Although these measurements obtained at 50 MHz are well beyond the frequencies used clinically, the influence of the regional variations in acoustic properties discernable at high frequencies may affect features observed in clinical fetal echocardiographic imaging (Holland *et al.*, 1998). Previous studies from our laboratory suggest several of the features of myocardial backscatter observed at lower frequencies (e.g., anisotropy of backscatter) (Hoffmeister *et al.*, 1995; Mottley and Miller, 1988) are observed at higher frequencies as well (Bridal *et al.*, 1993; Hall *et al.*, 2000a,b; Saijo *et al.*, 1997).

Knowledge of the intrinsic properties of the fetal heart may permit researchers and clinicians to more accurately identify abnormalities of the myocardium earlier than they are currently identified and permit an enhanced interpretation of the *in vivo* examinations of the fetal heart. Congenital heart defects and cardiomyopathies that exhibit a spectrum of pathologic substrates with myocardial fiber disarray and altered myoarchitecture evolve in the first trimester but are only recognized by current echocardiographic modalities in the second trimester. An evaluation of intrinsic properties of the fetal myocardium, discernable by backscatter and attenuation properties in the early stages of hearts destined to develop congenital heart defects, myopathies or altered myocardial function due to an adverse intrauterine environment, will likely improve diagnostic ability and the scope of favorable intervention in the future.

3.8 Limitations

A potential limitation of this study was that ultrasonic measurements were performed on formalin-fixed specimens at room temperature. While it is known that fixation does affect absolute values of ultrasonically measured quantities (Baldwin *et al.*, 2005b; Bamber *et al.*, 1979; Hall *et al.*, 2000a; Takiuchi *et al.*, 2001; van der Steen *et al.*, 1991), the measurements performed in this study focused on relative properties of the heart, which should be largely preserved in fixed myocardium. For this research study, the length of time required for data acquisition (hours) and concerns regarding fresh tissue degradation made the use of fresh tissue impractical, although desirable.

The region of interest placement may represent another concern of our study. Regions of interest were intentionally located in areas primarily perpendicular to the direction of insonification, as validated by histological analysis, in order to minimize the effects of myocardial anisotropy. However, it is possible that some regions encircle a few non-perpendicular fibers. Because the analysis averages over the entire area enclosed, the large number of perpendicular fibers in the enclosed area will minimize the effects of the non-perpendicular fibers.

3.9 Summary

Measurements of the attenuation coefficient at 45 MHz and slope of attenuation coefficient from 30-60 MHz demonstrate regional differences between the left and

right ventricular myocardium of the developing heart that appear to correspond to the regional differences in apparent integrated backscatter measurements and histological analyses reported in Chapter 2. Measurements exhibited the smallest levels of attenuation and the largest levels of backscatter for those regions where insonification was perpendicular to the predominant myofiber direction. More specifically, for data acquired with insonification perpendicular to the cut faces of the transverse cross-sectional fetal heart specimens, lower attenuation values and higher backscatter values were located in the mid-myocardium of the left ventricle and located more subepicardially in the right ventricular myocardium. Furthermore, attenuation and backscatter values for perpendicular insonification in the right ventricular free wall were larger than those areas in the left ventricular free wall, suggesting intrinsic differences between the two ventricles.

The results of this study appear consistent with previously published literature examining the differences in tissue properties of developing hearts (Salih *et al.*, 2004; Sanchez-Quintana *et al.*, 1995; Smolich *et al.*, 1989). It is interesting to note that, in spite of exposure to similar prenatal loading conditions, the left and right ventricular myocardium show architectural and compositional differences in the ultrasonic measurements. This suggests that the left and right ventricles of the fetal heart follow a biogenetically predetermined trajectory of growth and development that may be altered by the intrauterine environment. An adverse environment can result in an altered trajectory of the developing heart leading to a permanent change in cardiovascular structure and physiology (Barker, 1995; Lucas, 1991). Hence, prenatal changes

in structural and viscoelastic properties resulting in altered ultrasonic properties of the myocardium may permit analyses of fetal echocardiographic images to discern cardiac changes with consequential long-term postnatal effects.

Bibliography

AIUM (**1992**). "Standards and technical report", Technical Report, American Institue of Ultrasound in Medicine.

Baldwin, S. L., Marutyan, K. R., Yang, M., Wallace, K. D., Holland, M. R., and Miller, J. G. (**2006**). "Measurements of the anisotropy of ultrasonic attenuation in freshly excised myocardium", J Acoust Soc Am **119**, 3130–3139.

Baldwin, S. L., Yang, M., Marutyan, K. R., Wallace, K. D., Holland, M. R., and Miller, J. G. (**2005**a). "Measurements of the anisotropy of ultrasonic velocity in freshly excised and formalin-fixed myocardial tissue", J Acoust Soc Am **118**, 505–513.

Baldwin, S. L., Yang, M., Marutyan, K. R., Wallace, K. D., Holland, M. R., and Miller, J. G. (**2005**b). "Ultrasonic detection of the anisotropy of protein cross-linking in myocardium", IEEE Ultrason Symp 2263–2266.

Bamber, J. C., Hill, C. R., King, J. A., and Dunn, F. (**1979**). "Ultrasonic propagation through fixed and unfixed tissues", Ultrasound Med Biol **5**, 159–65.

Barker, D. J. (**1995**). "Fetal origins of coronary heart disease", BMJ **311**, 171–4.

Bridal, S. L., Recchia, D., Miller, J. G., and Wickline, S. A. (**1993**). "Anisotropy of apparent integrated backscatter, signal loss, and backscatter coefficient at 30 to 45 MHz in canine papillary muscle", Ultrason Imaging **15**, 155–156.

Hall, C. S., Dent, C. L., Scott, M. J., and Wickline, S. A. (**2000**a). "High-frequency ultrasound detection of the temporal evolution of protein cross linking in myocardial tissue", IEEE Trans Ultrason Ferroelec Freq Control **47**, 1051–1058.

Hall, C. S., Scott, M. J., Lanza, G. M., Miller, J. G., and Wickline, S. A. (**2000**b). "The extracellular matrix is an important source of ultrasound backscatter from myocardium", J Acoust Soc Am **107**, 612–9.

Hall, C. S., Verdonk, E. D., Wickline, S. A., Perez, J. E., and Miller, J. G. (**1997**). "Anisotropy of the apparent frequency dependence of backscatter in formalin fixed human myocardium", J. Acoust. Soc. Am. **101**, 563–568.

Hoffmeister, B. K., Wong, A. K., Verdonk, E. D., Wickline, S. A., and Miller, J. G. (**1995**). "Comparison of the anisotropy of apparent integrated ultrasonic backscatter from fixed human tendon and fixed human myocardium", J. Acoust. Soc. Am. **97**, 1307–1313.

Holland, M. R., Kovacs, A., Posdamer, S. H., Wallace, K. D., and Miller, J. G. (**2005**). "Anisotropy of apparent backscatter in the short-axis view of mouse hearts", Ultrasound Med Biol **31**, 1623–1629.

Holland, M. R., Wilkenshoff, U. M., Finch-Johnston, A. E., Handley, S. M., Perez, J. E., and Miller, J. G. (**1998**). "Effects of myocardial fiber orientation in echocardiography: Quantitative measurements and computer simulation of the regional dependence of backscattered ultrasound in the parasternal short-axis view", J Am Soc Echocardiogr **11**, 929–937.

Hoyt, R., Skorton, D. J., Collins, S. M., and Melton, H. E., J. (**1984**). "Ultrasonic backscatter and collagen in normal ventricular myocardium", Circulation **69**, 775–82.

Hoyt, R. H., Collins, S. M., Skorton, D. J., Ericksen, E. E., and Conyers, D. (**1985**). "Assessment of fibrosis in infarcted human hearts by analysis of ultrasonic backscatter", Circulation **71**, 740–4.

Insana, M. F., Wagner, R. F., Brown, D. G., and Hall, T. J. (**1990**). "Describing small-scale structure in random media using pulse-echo ultrasound", J Acoust Soc Am **87**, 179–92.

Kumar, K. N. and Mottley, J. G. (**1994**). "Quantitative modeling of the anisotropy of ultrasonic backscatter from canine myocardium", IEEE Trans Ultrason Ferroelectr Freq Control **41**, 441–450.

Lizzi, F. L., Ostromogilsky, M., Feleppa, E. J., Rorke, M. C., and Yaremko, M. M. (**1987**). "Relationship of ultrasonic spectral parameters to features of tissue microstructure", IEEE Trans Ultrason Ferroelectr Freq Control **34**, 319–329.

Lucas, A. (**1991**). "Programming by early nutrition in man", Ciba Found Symp **156**, 38–50; discussion 50–5.

Madaras, E., Perez, J., Sobel, B., Mottley, J., and Miller, J. (**1988**). "Anisotropy of the ultrasonic backscatter of myocardial tissue: II. Measurements in vivo", J. Acoust. Soc. Am. **83**, 762–769.

Mimbs, J., O'Donnell, M., Bauwens, D., Miller, J., and Sobel, B. (**1980**). "The dependence of ultrasonic attenuation and backscatter on collagen content in dog and rabbit hearts", Circ Res **47**, 49–58.

Mimbs, J. W., O'Donnell, M., Miller, J. G., and Sobel, B. E. (**1981**). "Detection of cardiomyopathic changes induced by doxorubicin based on quantitative analysis of ultrasonic backscatter", Am J Cardiol **47**, 1056–60.

Mottley, J. G. and Miller, J. (**1988**). "Anisotropy of the ultrasonic backscatter of myocardial tissue: I. Theory and measurements in vitro", J. Acoust. Soc. Am. **83**, 755–761.

Mottley, J. G. and Miller, J. G. (**1990**). "Anisotropy of the ultrasonic attenuation in soft tissues: Measurements in vitro", J. Acoust. Soc. Am. **88**, 1203–1210.

Nguyen, C. T., Hall, C. S., Scott, M. J., Zhu, Q., Marsh, J., and Wickline, S. A. (**2001**). "Age-related alterations of cardiac tissue microstructure and material properties in Fischer 344 rats", Ultrasound Med Biol **27**, 611–9.

O'Brien, P. D., O'Brien, W. D., J., Rhyne, T. L., Warltier, D. C., and Sagar, K. B. (**1995**). "Relation of ultrasonic backscatter and acoustic propagation properties to myofibrillar length and myocardial thickness", Circulation **91**, 171–5.

O'Donnell, M., Mimbs, J. W., and Miller, J. G. (**1979**). "The relationship between collagen and ultrasonic attenuation in myocardial tissue", J Acoust Soc Am **65**, 512–7.

O'Donnell, M., Mimbs, J. W., and Miller, J. G. (**1981**). "Relationship between collagen and ultrasonic backscatter in myocardial tissue", J Acoust Soc Am **69**, 580–8.

Oelze, M. L., Zachary, J. F., and O'Brien, W. D., J. (**2002**). "Characterization of tissue microstructure using ultrasonic backscatter: theory and technique for optimization using a Gaussian form factor", J Acoust Soc Am **112**, 1202–11.

Ophir, J., Shawker, T., Maklad, N., Miller, J., Flax, S., Narayana, P., and Jones, J. (**1984**). "Attenuation estimation in reflection: Progress and prospects", Ultrasonic Imaging **6**, 349–395.

Perez, J. E., Barzilai, B., Madaras, E. I., Glueck, R. M., Saffitz, J. E., Johnston, P., Miller, J. G., and Sobel, B. E. (**1984**). "Applicability of ultrasonic tissue characterization for longitudinal assessment and differentiation of calcification and fibrosis in cardiomyopathy", J Am Coll Cardiol **4**, 88–95.

Pohlhammer, J. and O'Brien, W. D., J. (**1981**). "Dependence of the ultrasonic scatter coefficient on collagen concentration in mammalian tissues", J Acoust Soc Am **69**, 283–5.

Rose, J. H., Kaufmann, M. R., Wickline, S. A., Hall, C. S., and Miller, J. G. (**1995**). "A proposed microscopic elastic wave theory for ultrasonic backscatter from myocardial tissue", J Acoust Soc Am **97**, 656–68.

Saijo, Y., Tanaka, M., Okawai, H., Sasaki, H., Nitta, S. I., and Dunn, F. (**1997**). "Ultrasonic tissue characterization of infarcted myocardium by scanning acoustic microscopy", Ultrasound Med Biol **23**, 77–85.

Salih, C., McCarthy, K., and Ho, S. Y. (**2004**). "The fibrous matrix of ventricular myocardium in hypoplastic left heart syndrome: A quantitative and qualitative analysis", Ann Thorac Surg **77**, 36–40.

Sanchez-Quintana, D., Garcia-Martinez, V., Climent, V., and Hurle, J. (**1995**). "Morphological changes in the normal pattern of ventricular myoarchitecture in the developing human heart", Anat Rec **243**, 483–495.

Smolich, J. J., Walker, A. M., Campbell, G. R., and Adamson, T. M. (**1989**). "Left and right ventricular myocardial morphometry in fetal, neonatal, and adult sheep", Am J Physiol **257**, H1–9.

Sosnovik, D. E., Baldwin, S. L., Holland, M. R., and Miller, J. G. (**2001**). "Transmural variation of myocardial attenuation and its potential effect on contrast-mediated estimates of regional myocardial perfusion", J Am Soc Echocardiogr **14**, 782–8.

Takiuchi, S., Marsh, J. N., Hall, C. S., Lanza, G. M., and Wickline, S. A. (**2001**). "Unexpected anisotropic behavior of ultrasound attenuation after collagen cross-linking in porcine tendons", in *IEEE Ultrason Symp*, volume 2, 1253–1256.

van der Steen, A. F., Cuypers, M. H., Thijssen, J. M., and de Wilde, P. C. (**1991**). "Influence of histochemical preparation on acoustic parameters of liver tissue: a 5-MHz study", Ultrasound Med Biol **17**, 879–91.

Verdonk, E. D., Hoffmeister, B. K., Wickline, S. A., and Miller, J. G. (**1996**). "Anisotropy of the slope of ultrasonic attenuation in formalin fixed human myocardium", J. Acoust. Soc. Am. **99**, 3837–3843.

Wear, K. A., Milunski, M. R., Wickline, S. A., Perez, J. E., Sobel, B. E., and Miller, J. G. (**1989**). "Differentiation between acutely ischemic myocardium and zones of completed infarction in dogs on the basis of frequency-dependent backscatter", J Acoust Soc Am **85**, 2634–2641.

Wong, A. K., Osborn, T. G., Miller, J. G., and Wickline, S. A. (**1993**). "Quantification of ventricular remodeling in the tight-skin mouse cardiomyopathy with acoustic microscopy", Ultrasound Med Biol **19**, 365–74.

Wrathall, A., Bailey, J., and Hebert, C. (**1974**). "A radiographic study of development of appendicular skeleton in the fetal pig", Res Vet Sci **17**, 154–168.

Yang, M., Baldwin, S. L., Marutyan, K. R., Wallace, K. D., Holland, M. R., and Miller, J. G. (**2006**). "Elastic stiffness coefficients (c11, c33, and c13) for freshly excised and formalin-fixed myocardium from ultrasonic velocity measurements", J Acoust Soc Am **119**, 1880–1887.

Chapter 4

Ultrasonic Images of Mid-gestational Fetal Hearts

4.1 Description of the Images

This Chapter presents quantitative images of the 15 fetal pig heart slices that are analyzed in Chapters 2 and 3 of this thesis. For each heart there are three ultrasonic images that are displayed horizontally for ease of visual comparison. In each image, the left ventricle is located in the upper-right section or upper half of the image and the right ventricle is positioned in the lower-left section or lower half.

In each figure the columns group the fetal pig heart images by the ultrasonic data analyses used to create them. The left column correspond to the data analysis performed in Chapter 2 and contain images of the integrated backscatter from 30-60 MHz. In order to permit direct comparisons among these, these backscatter images are displayed using identical grayscale color mappings from -20dB to -60dB. In the left column, the color "white" represents large backscatter whereas the color "black"

represents little backscatter.

The images in the middle and right columns show the relative differences in attenuation properties of the fetal hearts and correspond to the data analyses in Chapter 3. The middle column display images of the slope of attenuation from 30-60 MHz, and the right column show images of the attenuation coefficient at midbandwidth, 45 MHz, as determined from a least squared fit line to the data over the entire available bandwidth. In the middle and right columns, the color "white" represents large slope of attenuation and large attenuation coefficient respectively. The color "black" corresponds to small values of slope of attenuation and attenuation coefficient. In a fashion similar to that employed for the integrated backscatter images, each column of attenuation images is displayed with identical grayscale color mappings so that results from the individual hearts can be compared. The values for slope of attenuation from 30-60 MHz range from 0.5 to 2.0 dB/(cm·MHz) and the values for the attenuation coefficient at 45 MHz range from 25 to 75 dB/cm.

4.2 Comparison of the Images

As discussed in Chapters 2 and 3, a number of structures are common to essentially all of the fetal pig heart images. In general, the bright band that appears in the left ventricular free wall of the integrated backscatter images is located in the midmyocardium. In contrast, the bright band that appears in the right ventricular myocardium is more subepicardial.

The bright bands within the integrated backscatter images are in the same locations as the darker bands in the attenuation images of the same fetal heart specimen. These locations correspond to the portion of the ventricle in which the local myofiber arrangement is most perpendicular to the incident ultrasonic beam. This result is consistent with what would be anticipated based on previously published studies examining the effects of anisotropy on ultrasonic parameters and is quantified in Figure 3.6 (Baldwin *et al.*, 2006; Hall *et al.*, 1997; Hoffmeister *et al.*, 1995; Kumar and Mottley, 1994; Madaras *et al.*, 1988; Mottley and Miller, 1988, 1990; Sosnovik *et al.*, 2001; Verdonk *et al.*, 1996).

In addition to the ventricular anisotropy, the 15 fetal pig hearts show similarities in their relative brightness between the left and right myocardium. In general the right side of the heart appears brighter than the left side of the heart. This observation was quantified in Chapters 2 and 3 for regions of interest drawn within the bands of perpendicular insonification in the left and right ventricular myocardium. Although the difference in relative brightness between the two ventricles is easiest to see in the attenuation images, this observation holds true for all three methods of data analysis, integrated backscatter, slope of attenuation, and attenuation coefficient at midband.

4.3 Anomalies Within the Images

Several images, specifically the attenuation coefficient images for pig 1, pig 4 and pig 10, show large white circles within the myocardium. These white spots are be-

lieved to be air bubbles that accumulated on the surface of the myocardium during the multiple hour data acquisition. These suspected surface bubble artifacts are more readily apparent on the shadowed reflector attenuation measurements where surface effects can affect the data; whereas the backscatter measurements might be less influenced by surface effects because they are based on gated regions of backscatter from within the myocardium. Although these artifacts do affect the qualitative appearance of the ultrasonic images, the quantitative analyses were not affected. Regions of interest used for quantitative analyses were specifically drawn to not include any large bright spots.

In several of the attenuation images (e.g. pig 7 and pig 11), small white spots appear in the ventricular myocardium and are sometimes denser on the right side than on to the left. Unlike the larger bright spots described previously, we believe these smaller spots are not air bubbles and possibly reflect actual features of the fetal myocardium.

4.4 Summary

Differences in the properties of left and right ventricular myocardium, as reflected in the images displayed in this chapter, are clearly evident for all 15 midgestational fetal pig hearts. These differences in the ventricular myoarchitecture exist despite the fact that left and rights sides of heart are exposed to very similar prenatal pressures and loading conditions, conditions that are known to represent important determi-

nants of ventricular geometry. To our knowledge, existing models for fetal ventricular development do not account for this result.

4.5 Images

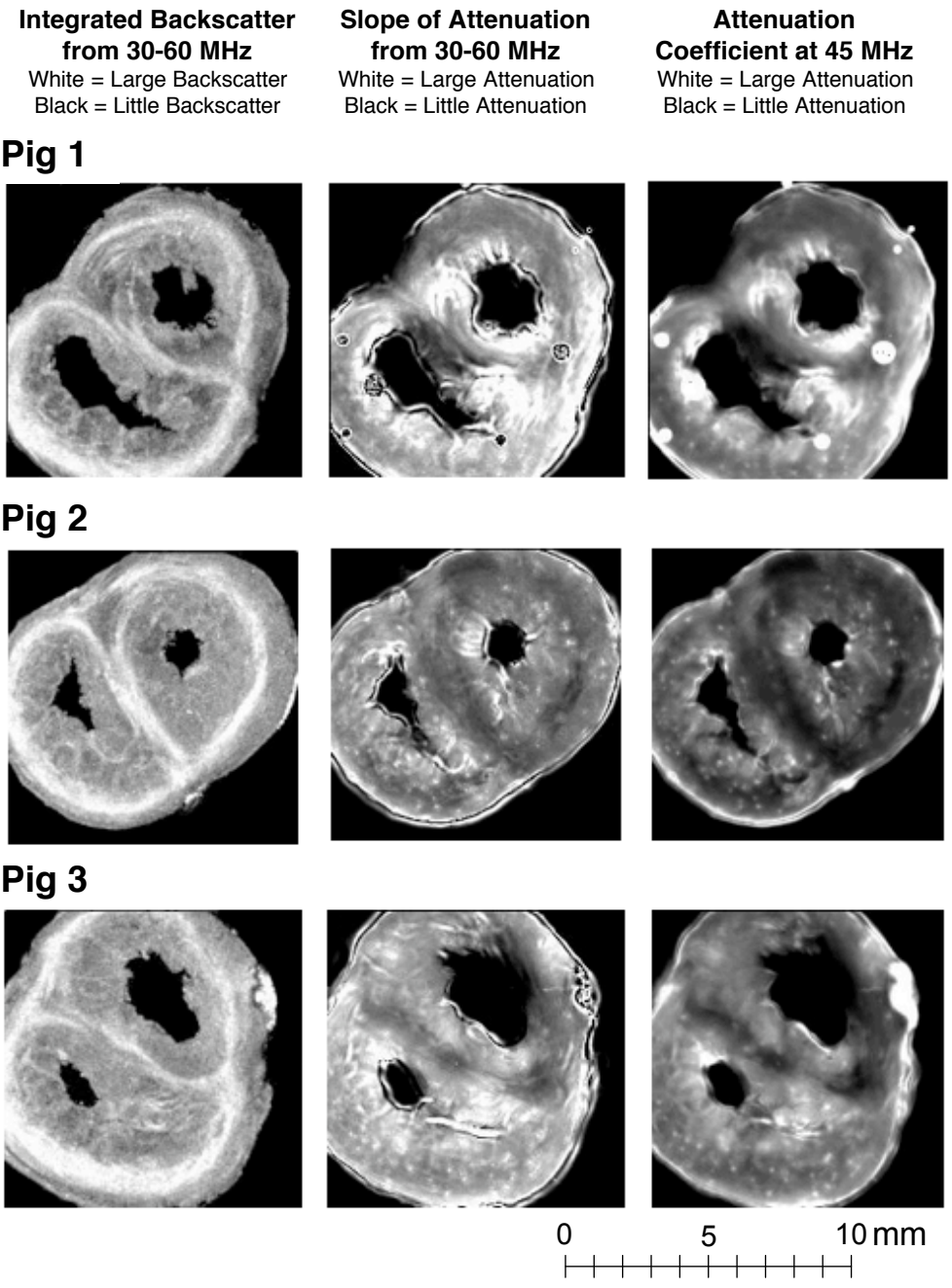

FIGURE 4.1: Ultrasonic images of fetal pigs 1, 2, and 3

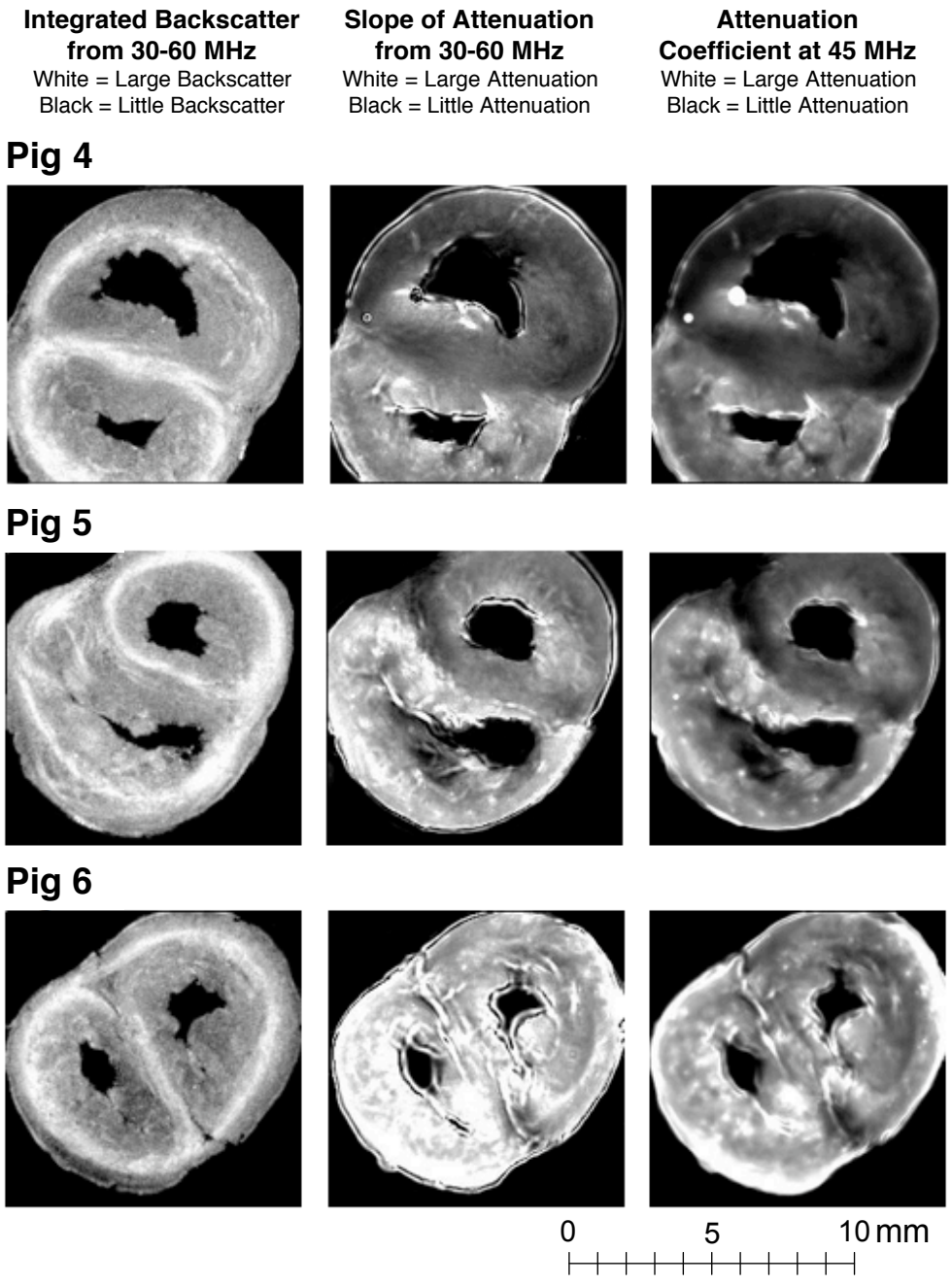

FIGURE 4.2: Ultrasonic images of fetal pigs 4, 5, and 6

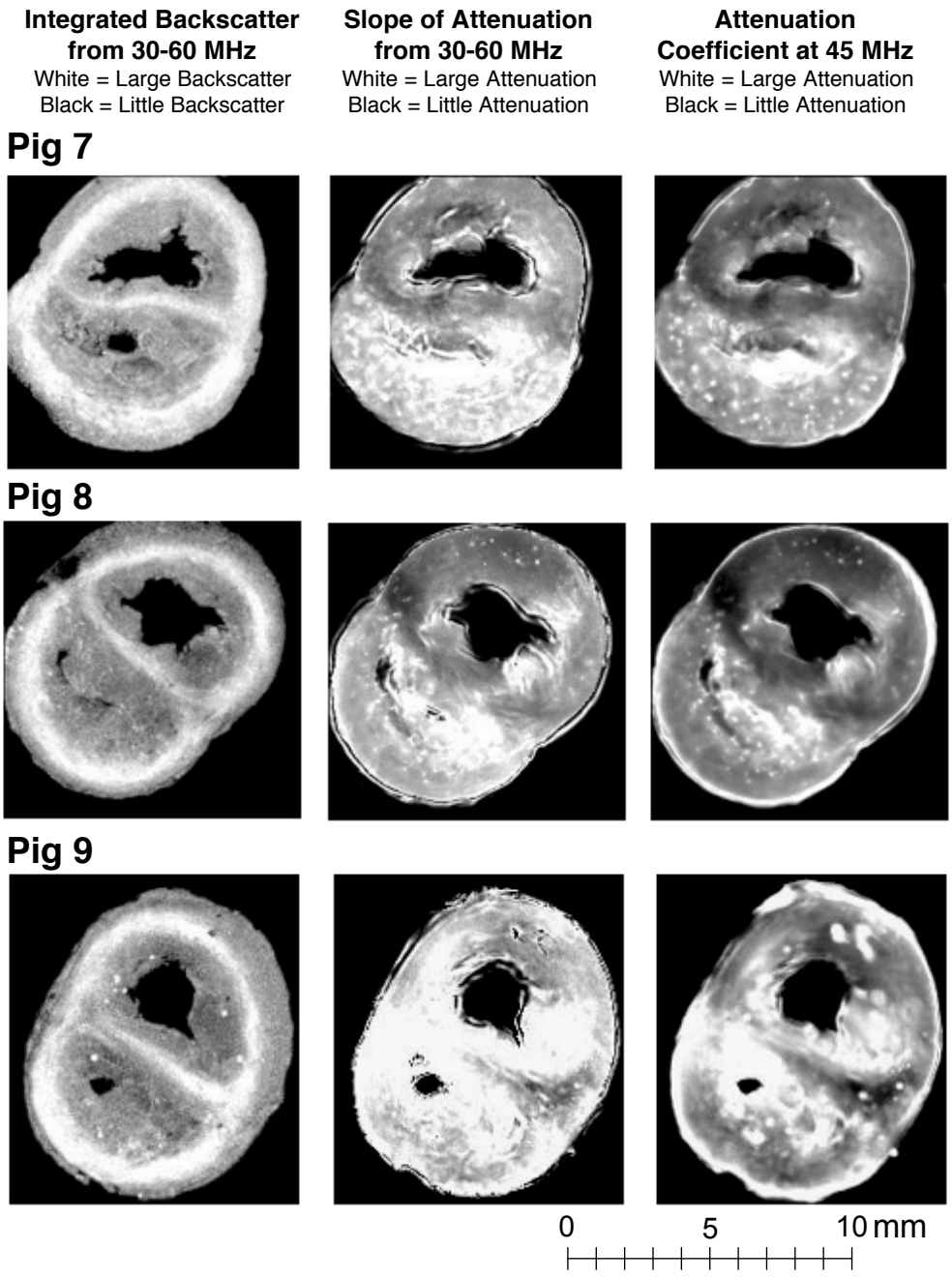

FIGURE 4.3: Ultrasonic images of fetal pigs 7, 8, and 9

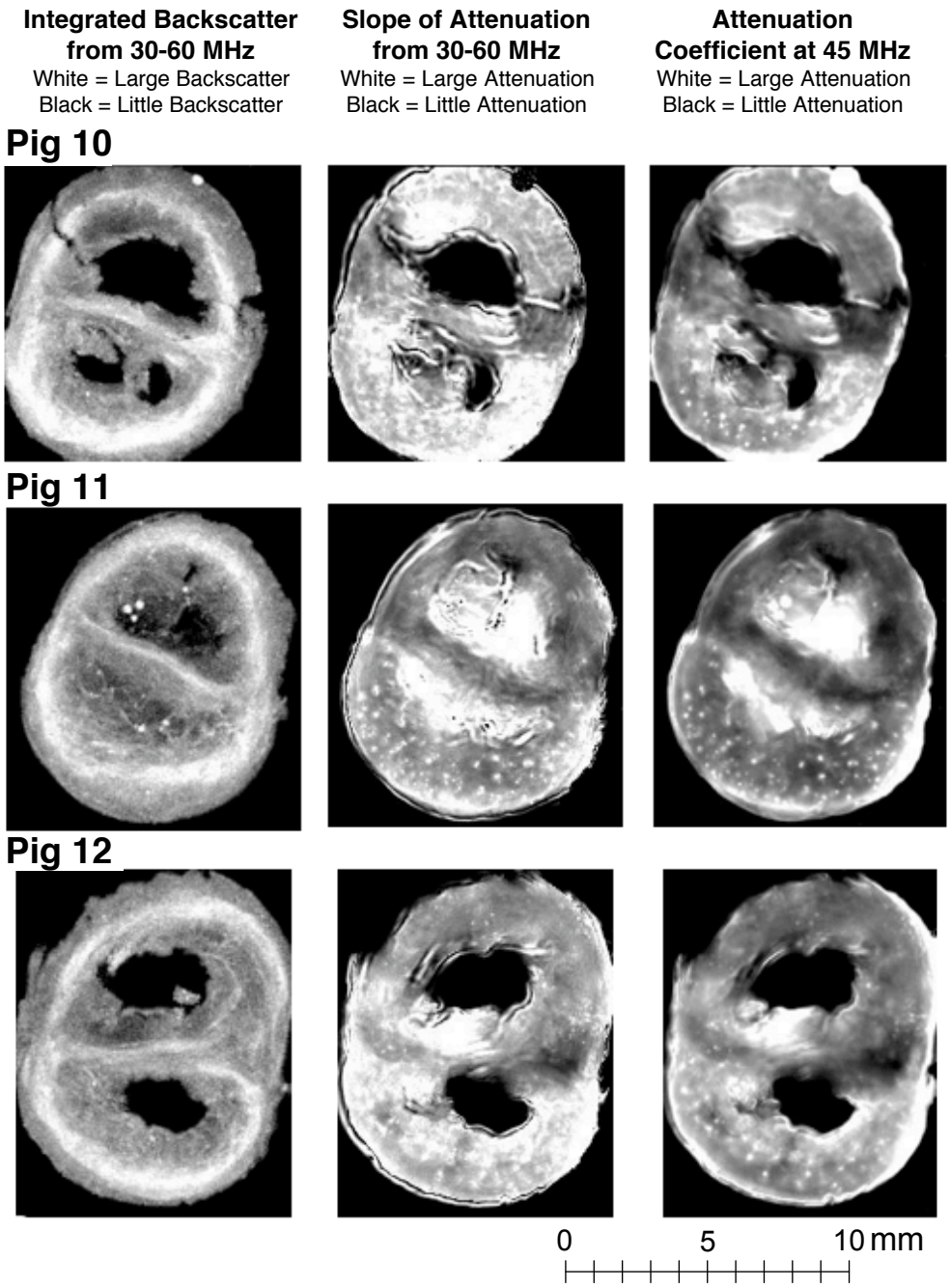

FIGURE 4.4: Ultrasonic images of fetal pigs 10, 11, and 12

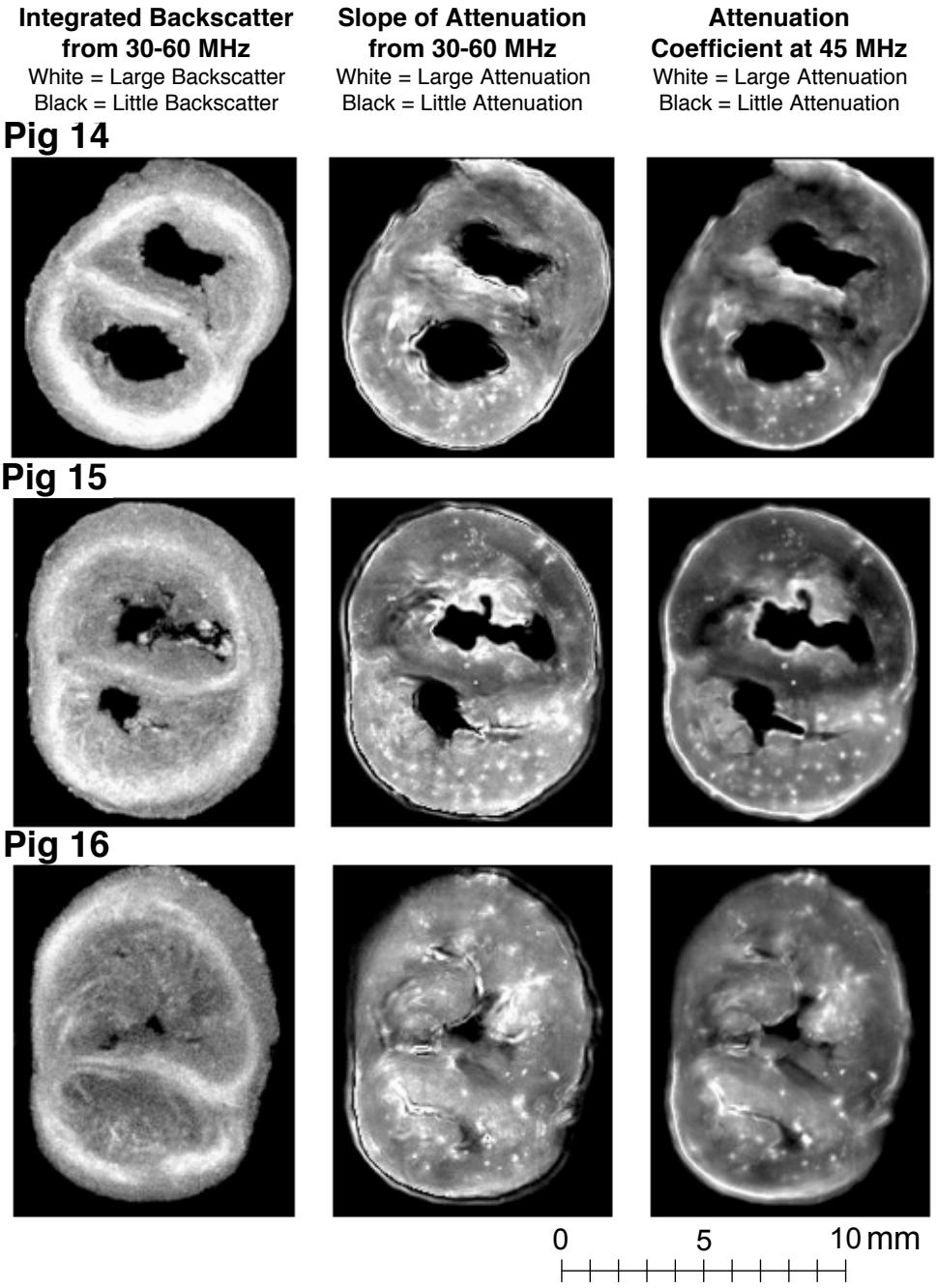

FIGURE 4.5: Ultrasonic images of fetal pigs 14, 15, and 16

Bibliography

Baldwin, S. L., Marutyan, K. R., Yang, M., Wallace, K. D., Holland, M. R., and Miller, J. G. (**2006**). "Measurements of the anisotropy of ultrasonic attenuation in freshly excised myocardium", J Acoust Soc Am **119**, 3130–3139.

Hall, C. S., Verdonk, E. D., Wickline, S. A., Perez, J. E., and Miller, J. G. (**1997**). "Anisotropy of the apparent frequency dependence of backscatter in formalin fixed human myocardium", J. Acoust. Soc. Am. **101**, 563–568.

Hoffmeister, B. K., Wong, A. K., Verdonk, E. D., Wickline, S. A., and Miller, J. G. (**1995**). "Comparison of the anisotropy of apparent integrated ultrasonic backscatter from fixed human tendon and fixed human myocardium", J. Acoust. Soc. Am. **97**, 1307–1313.

Kumar, K. N. and Mottley, J. G. (**1994**). "Quantitative modeling of the anisotropy of ultrasonic backscatter from canine myocardium", IEEE Trans Ultrason Ferroelectr Freq Control **41**, 441–450.

Madaras, E., Perez, J., Sobel, B., Mottley, J., and Miller, J. (**1988**). "Anisotropy of the ultrasonic backscatter of myocardial tissue: II. Measurements in vivo", J. Acoust. Soc. Am. **83**, 762–769.

Mottley, J. G. and Miller, J. (**1988**). "Anisotropy of the ultrasonic backscatter of myocardial tissue: I. Theory and measurements in vitro", J. Acoust. Soc. Am. **83**, 755–761.

Mottley, J. G. and Miller, J. G. (**1990**). "Anisotropy of the ultrasonic attenuation in soft tissues: Measurements in vitro", J. Acoust. Soc. Am. **88**, 1203–1210.

Sosnovik, D. E., Baldwin, S. L., Holland, M. R., and Miller, J. G. (**2001**). "Transmural variation of myocardial attenuation and its potential effect on contrast-mediated estimates of regional myocardial perfusion", J Am Soc Echocardiogr **14**, 782–8.

Verdonk, E. D., Hoffmeister, B. K., Wickline, S. A., and Miller, J. G. (**1996**). "Anisotropy of the slope of ultrasonic attenuation in formalin fixed human myocardium", J. Acoust. Soc. Am. **99**, 3837–3843.

Chapter 5

Quantitative Analysis of Cyclic Variation of Myocardial Backscatter

5.1 Preface

This chapter is based on the peer-reviewed journal article *Quantitative Analysis of the Magnitude and Time Delay of Cyclic Variation of Myocardial Backscatter from Asymptomatic Type 2 Diabetes Mellitus Subjects* written by Allyson A. Gibson, Jean E. Schaffer, Linda R. Peterson, Kyle R. Bilhorn, Karla M. Robert, Troy A. Haider, Marsha S. Farmer, Mark R. Holland, James G. Miller and published in *Ultrasound in Medicine & Biology, Vol. 35, No. 9, pp. 1458-1467, 2009.*

5.2 Abstract

Early detection of diabetic patients at high risk for developing diabetic cardiomyopathy may permit effective intervention. The goal of this work is to determine whether measurements of the magnitude and time delay of cyclic variation of myocardial backscatter, individually and in combination, can be used to discriminate between subgroups of individuals including normal controls and asymptomatic type 2 diabetes subjects. Two-dimensional parasternal long-axis echocardiographic images of 104 type 2 diabetic patients and 44 normal volunteers were acquired. Cyclic variation data were produced by measuring the mean myocardial backscatter level within a region of interest in the posterior wall, and characterized in terms of the magnitude and normalized time delay. The cyclic variation parameters were analyzed using Bayes classification and a nonparametric estimate of the area under the receiver operating characteristic (ROC) curve to illustrate the relative effectiveness of using one or two features to segregate subgroups of individuals. The subjects were grouped based on glycated hemoglobin (HbA1c), the homeostasis model assessment for insulin resistance (HOMA-IR), and the ratio of triglyceride to high-density lipoprotein cholesterol (TG/HDL-C). Analyses comparing the cyclic variation measurements of subjects in the highest and lowest quartiles of HbA1c, HOMA-IR, and TG/HDL-C showed substantial differences in the mean magnitude and normalized time delay of cyclic variation. Results show that analyses of the cyclic variation of backscatter in young asymptomatic type 2 diabetics may be an early indicator for the development

of diabetic cardiomyopathy.

5.3 Introduction

Insulin resistance and type 2 diabetes are growing concerns in populations in which there is an increasing prevalence of obesity. Although diabetes is a well-known risk factor for coronary artery disease, and consequently, ischemia-related heart failure, there is increasing evidence that diabetes is also a risk factor for the development of heart failure apart from coronary disease, a so-called "diabetic cardiomyopathy" (Fang *et al.*, 2004; Hamby *et al.*, 1974; Kannel *et al.*, 1974; Witteles and Fowler, 2008).

The mechanisms for the development of diabetic cardiomyopathy are not completely known and likely involve multiple pathways including impaired renal function, sympathetic/parasympathetic imbalance, protein glycosylation, and upregulation of the renin-angiotensin-aldosterone system. Evidence is also emerging that hyperlipidemia plays a central role in the pathogenesis of heart failure in diabetic patients, independent of atherosclerosis. Type 2 diabetes is associated with elevated serum triglyceride and free fatty acid level (Barrett-Connor *et al.*, 1982; Fraze *et al.*, 1985; Hallgren *et al.*, 1960). These elevated levels can increase the supply of fatty acid substrates to the heart, increase fatty acid utilization, and alter the lipid homeostasis of the tissue, particularly in the setting of insulin resistance (Augustus *et al.*, 2003; Carley and Severson, 2005; Peterson *et al.*, 2004; Stremmel, 1988). Several mouse models show that accumulation of lipids in non-adipose tissue such as the myocardium can

lead to cell dysfunction and cell death, and ultimately result in cardiomyopathy, even in the absence of hyperglycemia (Borradaile and Schaffer, 2005; Chiu *et al.*, 2001, 2005; Finck *et al.*, 2003; Nielsen *et al.*, 2002; Rijzewijk *et al.*, 2008; Zhou *et al.*, 2000). While the link between lipid metabolic abnormalities and cardiomyopathy in diabetic patients is less clear, evidence suggests that the myocardium of patients with type 2 diabetes is exposed to excessive free fatty acid and triglyceride delivery, which causes lipotoxicity and thereby contributes to the development of diabetic cardiomyopathy. This is supported by studies demonstrating increased myocardial triglycerides in hearts of diabetic patients at autopsy and in pathological examinations of failing hearts explanted from individuals with diabetes and cardiomyopathy who underwent orthotopic cardiac transplantation (Alavaikko *et al.*, 1973; Sharma *et al.*, 2004; Szczepaniak *et al.*, 2003).

Cyclic variation of myocardial backscatter is a non-invasive approach for assessing myocardial structure and function. This form of tissue characterization analysis has been employed to characterize a number of cardiac pathologies including ischemia (Barzilai *et al.*, 1984), myocardial infarction (Hancock *et al.*, 2002; Iwakura *et al.*, 2003; Ohara *et al.*, 2005), cardiac hypertrophy (Losi *et al.*, 2007; Masuyama *et al.*, 1989), and changes in myocardial size, structure, and function (Di Bello *et al.*, 1998; Giglio *et al.*, 2003; Hu *et al.*, 2003; Komuro *et al.*, 2005; Madaras *et al.*, 1983; Micari *et al.*, 2006; Naito *et al.*, 1996). One such study from our laboratory examined differences in magnitude and normalized time delay of cyclic variation of backscatter among type 1 diabetic patients with systemic complications and normal controls

(Perez *et al.*, 1992). In a follow up study, Wagner et al. extended this work by using Receiver Operating Characteristic (ROC) analysis to quantitatively assess the univariate and multivariate discriminating power of the cyclic variation parameters (Wagner *et al.*, 1995). The results of that paper indicated that a combination of two or more cyclic variation parameters (magnitude of the septal wall, time delay of the septal wall, magnitude of the left ventricular free wall, and time delay of the left ventricular free well) yielded a larger area under the ROC curve than a single feature. Early detection of diabetic patients at high risk for developing diabetic cardiomyopathy might permit effective intervention. The long-term goal of this exploratory study is to determine whether myocardial tissue characterization based on measurements of the magnitude and time delay of cyclic variation of myocardial backscatter might be a useful non-invasive indicator of hearts at potentially higher risk for developing diabetic cardiomyopathy. Although a longitudinal study over many years would be required to determine the utility of this approach in modifying clinical outcomes, this preliminary study examines methodology that might be appropriate for such a longer-term investigation.

5.4 Methods

5.4.1 Subjects Studied

A total of 148 subjects (44 normal controls and 104 asymptomatic type 2 diabetic patients) between the ages of 30 and 55 years old were recruited for the research

study over a 3-year period. Subjects were enrolled in the study after signing informed consent forms approved by the Washington University Human Studies Committee. Subjects were excluded if they met the following criteria that are known to affect adversely heart function or metabolism independent of parameters being studied: participants who had greater than Stage 1 hypertension as defined by the seventh report of the Joint National Committee (JNC, 2003); valvular disease including trace or mild valvular regurgitation; systolic dysfunction; ischemic heart disease as assessed by a screening stress echocardiography exam; or symptoms of heart failure. Subjects were also excluded if they were outside the age range of 30 to 55 years old, current smokers, postmenopausal, pregnant or lactating. Out of the 148 subjects enrolled, 7 subjects withdrew from the study, 4 subjects did not have all the plasma markers needed for analysis, and data from 12 subjects were not analyzed due to poor signal to noise ratios for the tissue characterization measurements. In the end, data from 125 subjects were collected and analyzed. These 125 subjects had an average age of 43 ± 7 years (mean $\pm$ standard deviation) and included 72 females and 53 males.

5.4.2 Laboratory Tests

Once a subject was enrolled in the study, laboratory tests were performed after an overnight fast. The tests included fasting glucose, glycated hemoglobin, lipid, and protein levels. The echocardiographic evaluation included standard measurements to assess cardiac function as well as study specific measurements such as tissue characterization.

5.4.3 Tissue Characterization Data Acquisition

A detailed description of the system calibration, backscatter data acquisition, and cyclic variation analysis can be found in Holland et al. (2006) and is summarized below. Subjects were imaged using a General Electric (GE) Vivid 7 clinical imaging system (General Electric Medical Systems, Waukesha, WI). Data was collected from the parasternal long-axis view in harmonic imaging mode with a transmit frequency of 1.7 MHz and a receive frequency of 3.4 MHz. The post-processing settings (compression, reject, dynamic range, data dependent processing (DDP)) of the imaging system were configured to optimize the dynamic range of images of the left ventricular free wall, and to provide a linear relationship between changes in the displayed grayscale value and changes in the level of ultrasonic backscatter expressed in decibels. This relationship was achieved by acquiring a succession of images of a tissue-mimicking phantom as the overall receiver gain was systematically changed in known decibel (dB) steps for a specific post-processing and dynamic range setting. The phantom images were analyzed offline using NIH ImageJ (National Institutes of Health, Bethesda, MD). In this approach, a region of interest was placed within each phantom image and the mean grayscale value was measured. Analysis of the measured mean grayscale level corresponding to each known gain setting was used to determine the relationship between changes in the displayed grayscale value and changes expressed in dB. Furthermore, this approach established the useful dynamic range (the linear backscatter to grayscale range) of the imaging system for a specific

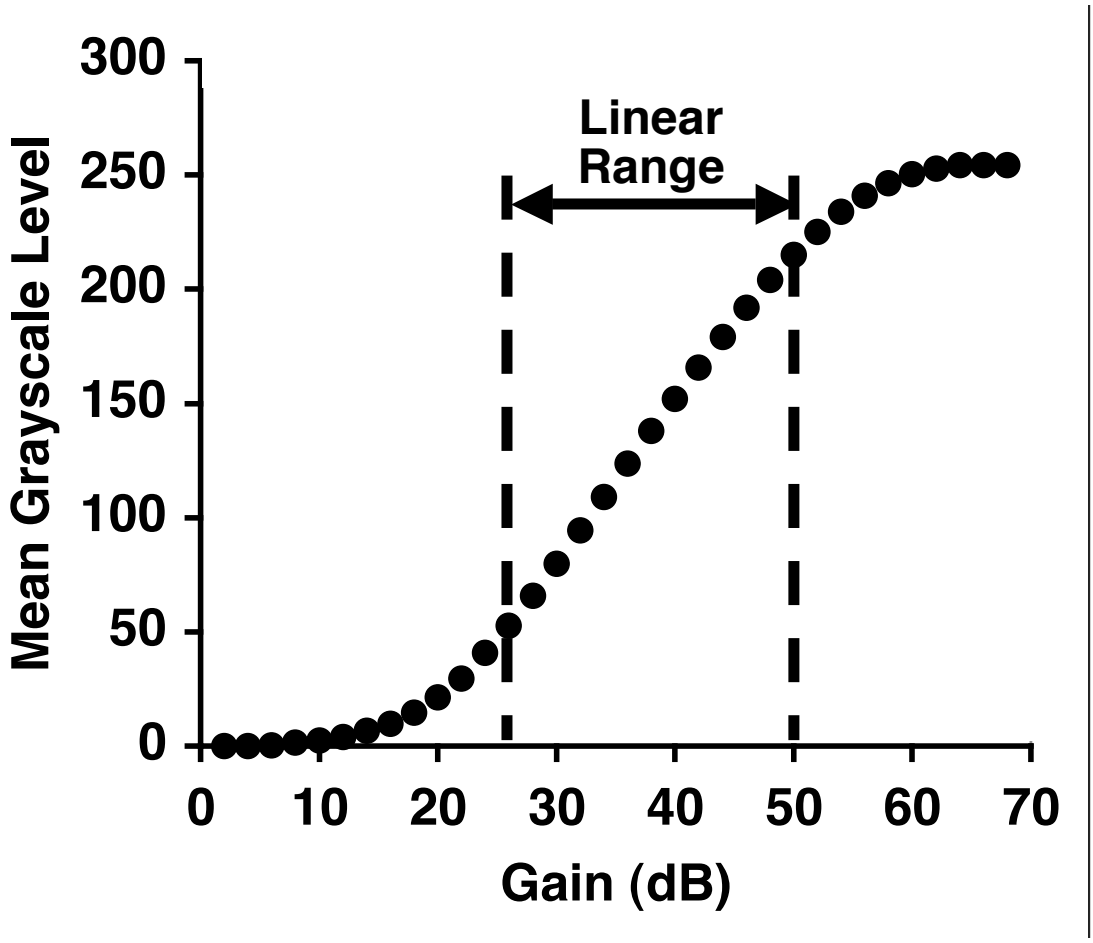

FIGURE 5.1: Relationship between ultrasonic backscatter level (expressed in decibels [dB]) and mean grayscale value for one specific configuration of the GE Vivid 7 clinical imaging system.

configuration.

Figure 5.1 illustrates the relationship between backscatter level and mean grayscale value for one specific configuration of the GE Vivid 7 clinical imaging system used in this study. The conversion factor relating a change in grayscale value to the equivalent change in decibels was found by determining the slope of the best-fit line in the "linear range" region. For the system configuration used in this study the conversion

factor was 6.98 grayscale level/dB.

To obtain echocardiographic data from subjects, images from five consecutive heart cycles were digitally acquired with the overall gain of the imaging system configured to maximize the available dynamic range of backscattered signals. Digital cine loops with frame rates of at least 30 frames/second were acquired and saved in a standard 8-bit image format (e.g. DICOM format). Because it was difficult to know the mean grayscale level of the mid-myocardium prior to quantitative data analyses, several sets of image data were acquired with different values of overall system gain. Subsequent analyses of the acquired image data were performed off-line using NIH ImageJ.

Backscatter data were generated from a region of interest that was manually tracked to stay within the mid-myocardium of the left ventricular free wall over the heart cycle. Figure 5.2a shows a representative echocardiographic image with a region of interest drawn in the posterior wall of the parasternal long-axis view. Previous studies have used this method of measuring backscatter data from a manually positioned region of interest and shown both intra- and inter-observer backscatter results are reproducible (Holland *et al.*, 2009). For each image frame of the cineloop, the mean grayscale value of the region of interest was recorded and converted to backscattered energy expressed in decibels. The backscattered energy was plotted versus time (or frame number) to yield the systematic variation of backscatter from the heart. A similar procedure was performed for a region of interest placed in the blood-filled cavity of the left ventricle. This analysis was done to ensure clutter in the image did

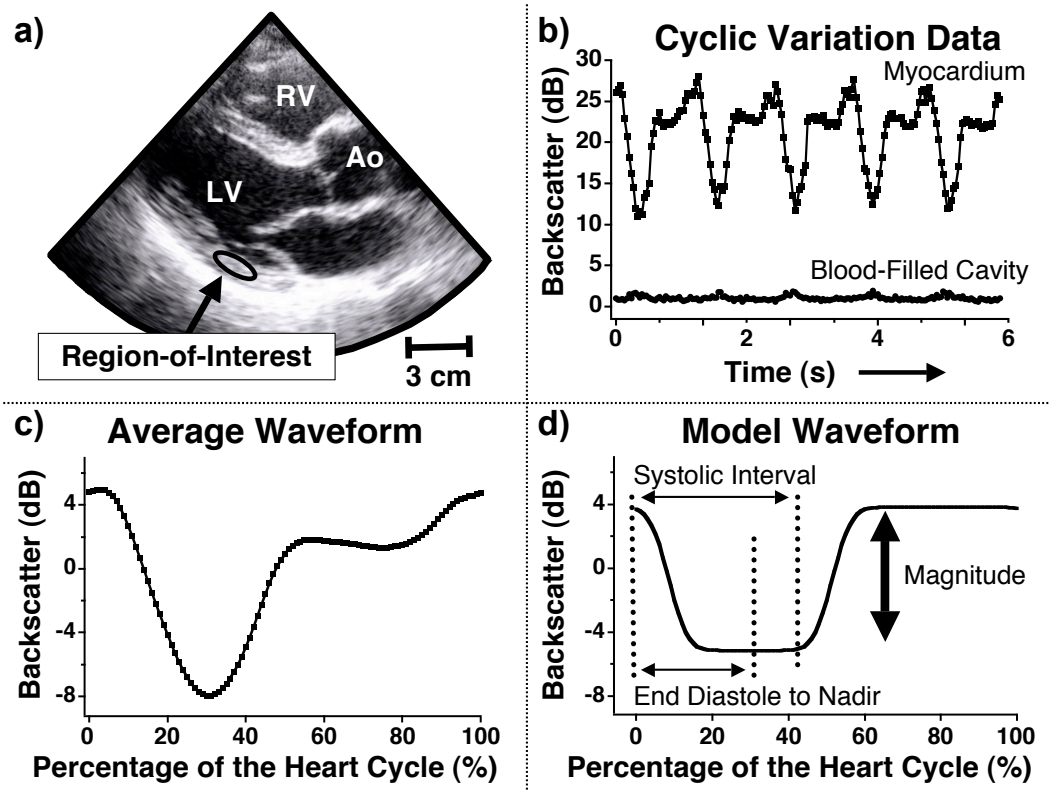

FIGURE 5.2: (a) Image showing a representative region of interest placed in the posterior wall of the parasternal long-axis view for one subject. RV = right ventricle LV = left ventricle Ao= aorta (b) Cyclic variation of myocardial backscatter data from the region of interest shown in Figure 5.2a and backscatter data from the blood-filled cavity. The vertical scale illustrates the relative difference in backscatter results and does not represent an absolute measurement. (c) Average waveform calculated from the five heart cycles illustrated in Figure 5.2b. The data are represented as a zero-mean curve and the heart cycle is defined as starting and ending with end diastole. (d) A model waveform utilized in the automated analysis of cyclic variation data (Mohr, *et al.*, 1989) to calculate the magnitude and time delay of the cyclic variation of myocardial backscatter. The vertical arrow illustrates the magnitude of cyclic variation, and the normalized time delay is calculated as the time interval from end diastole to the center of the nadir divided by the systolic interval.

not strongly affect the measured backscatter energy from the myocardium and ultimately influence the cyclic variation results. Figure 5.2b shows the cyclic variation of myocardial backscatter over five heart cycles for the region of interest drawn in Figure 5.2a, and for a region of interest placed in the blood-filled cavity. The vertical scale in Figure 5.2b illustrates the relative difference between the measured backscatter energy in the myocardium and the blood-filled cavity, and does not represent the absolute level of backscatter. Figure 5.2c depicts the average cyclic variation waveform calculated by averaging the five separate heart cycles of myocardial backscatter in Figure 5.2b. The data are represented as a zero-mean curve and plotted as a percentage of the heart cycle. In this formalism, end-diastole is defined as the start (0%) and end (100%) of the heart cycle.

The systematic variation of the backscattered energy was quantified by analyzing the magnitude and normalized time delay of cyclic variation using an automated algorithm (Mobley *et al.*, 1995; Mohr *et al.*, 1989). The magnitude of cyclic variation was calculated as the difference between the average peak and average nadir values of the backscattered energy. The corresponding normalized time delay is expressed as a dimensionless ratio obtained by dividing the time interval from end-diastole to the nadir of the mean backscatter trace by the systolic interval. Mitral valve motion was used to identify the diastolic and systolic intervals. End diastole was defined as the frame just after the mitral valve closed and end systole corresponded to the frame before the mitral valve opened. The analysis of magnitude and normalized time delay of cyclic variation are illustrated in Figure 5.2d.

5.4.4 Data Analysis

For this preliminary study, analyses of the cyclic variation of myocardial backscatter were performed with subjects divided into quartiles based on each of three indices, glycated hemoglobin (HbA1c), the homeostasis model assessment of insulin resistance (HOMA-IR) as calculated by The Oxford Centre for Diabetes, Endocrinology, and Metabolism HOMA calculator (Wallace *et al.*, 2004), and the ratio of triglyceride to high-density lipoprotein-cholesterol levels (TG/HDL-C). With regard to the choice of indices for these planned comparisons, HbA1c and HOMA-IR were selected for the data analyses because they represent useful indices for the monitoring of type 2 diabetic patients. The ratio of TG/HDL-C, which was previously employed as a predictor of insulin resistance and cardiometabolic risk in the Framingham offspring cohort (Kannel *et al.*, 2008), illustrates a particular dislipidemia that could play a role in the pathogenesis of heart failure in diabetic patients. For each classification, cyclic variation measurements from subjects in the highest quartile (N=32) were compared with those in the lowest quartile (N=32). The quartiles were determined by rank ordering the subjects according to the index of interest, and grouping the 32 subjects with the largest rank as the highest quartile and the 32 subjects with the smallest rank in the lowest quartile. Our hypothesis was that subjects with a high percentage of HbA1c, large value for HOMA-IR, or large ratio of TG/HDL-C exhibited a less favorable profile than those subjects with lower values. In this sense, the lowest quartile might be considered to be the "healthier" of the two quartiles; however, the

TABLE 5.1: A summary of the laboratory results for the study population. The column headings represent how the subjects were divided for cyclic variation analysis and the rows represent a subset of the biological parameters reported. All values are expressed as a mean ± standard deviation. The p values were determined using a two-tailed, unpaired student t-test. HOMA-IR = Homeostasis model assessment for insulin resistance, TG/HDL-C = Triglyceride to high density lipoprotein-cholesterol ratio, BMI = Body Mass Index, n.s. = not significant

	HbA1c		**HOMA-IR**		**TG/HDL-C**	
	Lowest Quartile (N=32)	Highest Quartile (N=32)	Lowest Quartile (N=32)	Highest Quartile (N=32)	Lowest Quartile (N=32)	Highest Quartile (N=32)
Gender	M=10 F=22	M=15 F=17	M=13 F=19	M=14 F=18	M=11 F=21	M=16 F=16
Age (yrs)	39 ± 6	44 ± 6	41 ± 6	43 ± 7	41 ± 6	43 ± 8
	$p < 0.05$		p = n.s.		p = n.s.	
BMI (kg/m^2)	28 ± 7	36 ± 7	26 ± 5	38 ± 7	31 ± 8	34 ± 7
	$p < 0.001$		$p < 0.001$		p = n.s.	
HbA1c (%)	5.4 ± 0.2	9.1 ± 1.3	5.7 ± 0.7	7.4 ± 1.6	6.7 ± 1.6	7.5 ± 1.7
	$p < 0.001$		$p < 0.001$		p = n.s.	
HOMA-IR	1.1 ± 0.7	2.8 ± 1.8	0.7 ± 0.2	4.7 ± 2.2	1.7 ± 1.9	3.1 ± 1.8
	$p < 0.001$		$p < 0.001$		$p < 0.01$	
TG/HDL-C	3.0 ± 3.0	6.4 ± 8.0	2.7 ± 2.9	6.8 ± 7.7	1.2 ± 0.3	10.7±7.4
	$p < 0.05$		$p < 0.01$		$p < 0.001$	

subjects in both groups have clinically normal hearts as assessed by a stress echocardiography exam. A subset of the laboratory results for these three subject groupings is presented in Table 5.1.

Cyclic variation data from the lowest and highest quartile-groups (small HbA1c, HOMA-IR, or ratio of TG/HDL-C and large HbA1c, HOMA-IR or ratio of TG/HDL-C respectively) served as the input data for Bayes classification. Bayes classification

was employed to combine information from the magnitude and time delay of cyclic variation and assign a subject to the lowest or highest quartile. Once the result was calculated for each subject, Receiver Operating Characteristic (ROC) analysis was used to assess the performance of the Bayes classified data. A more detailed explanation of Bayes classification and ROC analysis is provided in the Appendix of this chapter.

5.5 Results

The mean and standard error for the magnitude and time delay of cyclic variation of myocardial backscatter were analyzed for the highest and lowest quartile groups of each metabolic parameter to quantify how the subjects separated on average. Figure 5.3 illustrates these results for three metabolic parameters, HbA1c, HOMA-IR, and TG/HDL-C. For each parameter, we observed a separation between the lowest and highest quartiles for the magnitude and the normalized time delay. In all but one case this separation between the results for the lowest and highest quartile was calculated to be statistically significant with a two-tailed, unpaired student t-test. Of the three metabolic parameters, HbA1c yielded the largest separation between the mean magnitude results, with the lowest quartile averaging 5.4 dB and the highest quartile averaging 4.1 dB. The average time delay measurements for this classification were 0.78 and 0.85 for the lowest and highest quartiles respectively. Dividing the subjects by HOMA-IR resulted in a similar separation of the average time delays as that seen

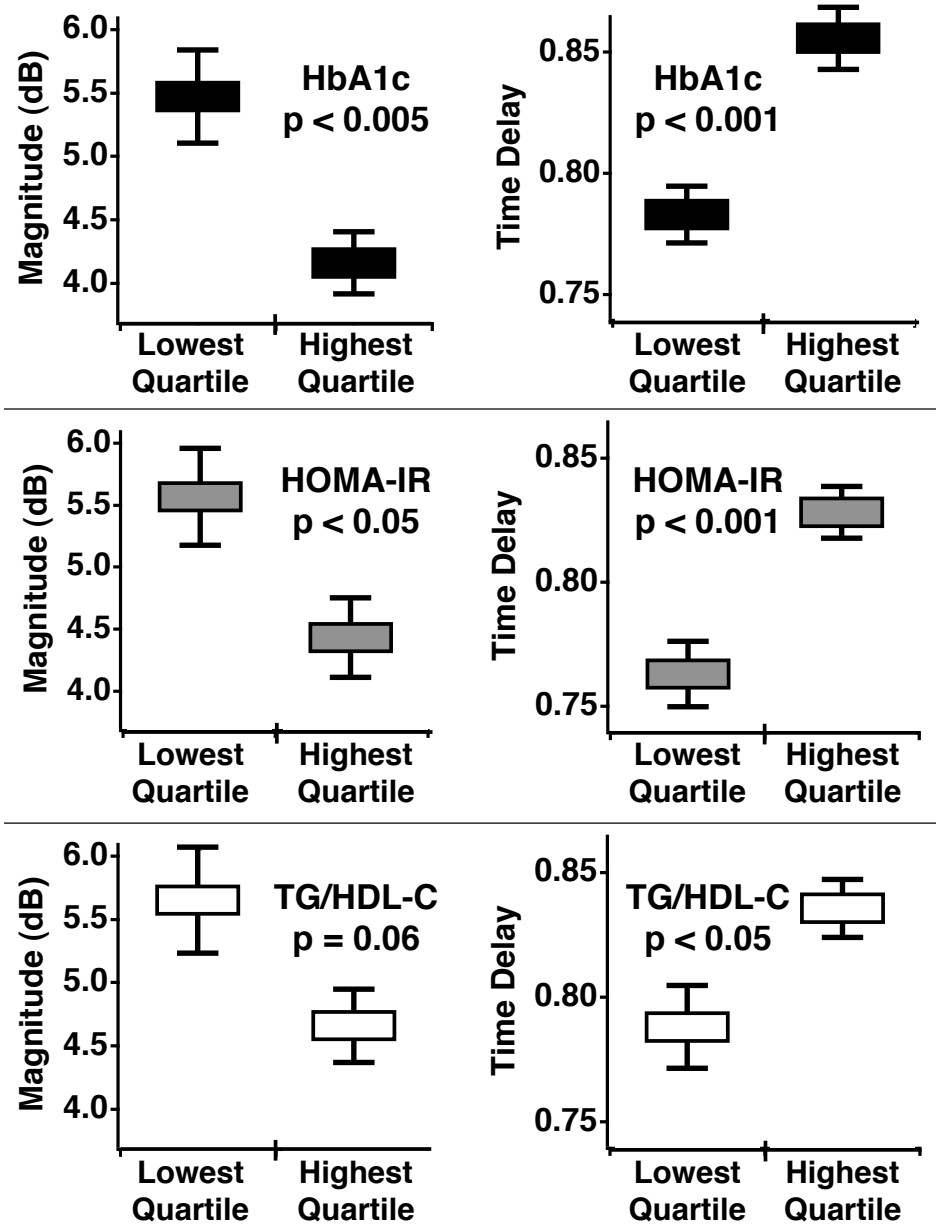

FIGURE 5.3: The averages and standard errors of the magnitude (left panels) and normalized time delay (right panels) of cyclic variation for the lowest and highest quartiles in each subject division. The significance of each cyclic variation parameters was found using a two-tailed unpaired student t-test. HbA1c = Hemoglobin A1c, HOMA-IR = Homeostasis model assessment for insulin resistance, TG/HDL-C = Triglyceride to high density lipoprotein-cholesterol ratio

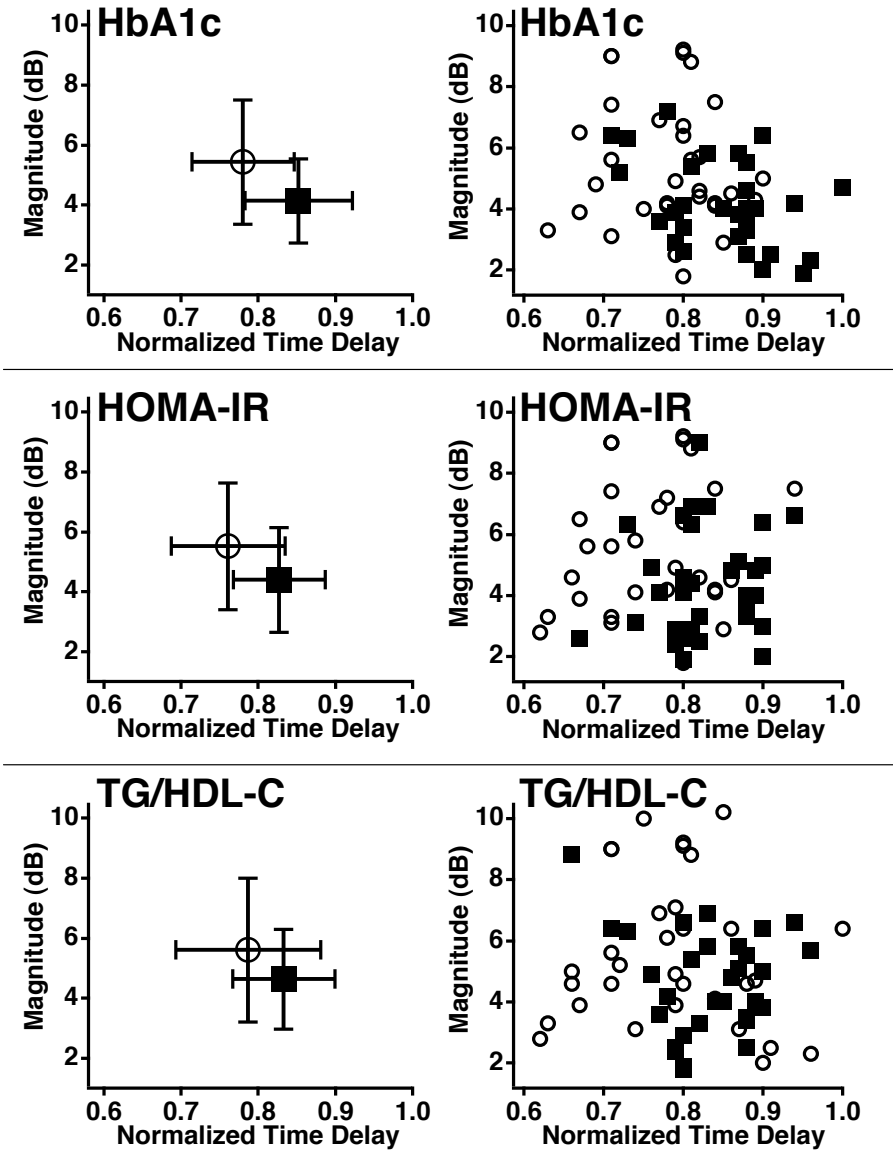

FIGURE 5.4: The left panels are the mean, and standard deviations of the magnitude and normalized time delay of cyclic variation for the lowest and highest quartiles in each subject division. The right panels are individual subject results for the magnitude and normalized time delay of cyclic variation. In all the graphs, the open circles represent the 32 subjects in the lowest quartile of each subject division while the squares illustrate the results for the 32 subjects in the highest quartiles. HbA1c = Hemoglobin A1c, HOMA-IR = Homeostasis model assessment for insulin resistance, TG/HDL-C = Triglyceride to high density lipoprotein-cholesterol ratio

in the HbA1c results. The results for subjects in the lowest and highest quartiles of HOMA-IR were mean time delays of 0.76 and 0.83, respectively, and mean magnitudes of 5.5 dB and 4.4 dB, respectively. TG/HDL-C yielded a less pronounced separation of the cyclic variation results than the other metabolic parameters. In this subject classification, the lowest quartile had an average magnitude of 5.6 dB and average time delay of 0.79 whereas the highest quartile had a mean value of 4.6 dB for the magnitude and 0.83 for the time delay. The magnitude and normalized time delay of cyclic variation are illustrated together in Figure 5.4. The left panels of Figure 5.4 show the means, and standard deviations for the magnitude and time delay of cyclic variation for the highest and lowest quartile groups of each metabolic parameter. The right panels display the individual data for the 64 subjects included in the HbA1c, HOMA-IR, and TG/HDL-C analysis. For the two cyclic variation parameters used in combination, the means suggest a modest separation of the data for all three subject classifications.

After the average cyclic variation results were obtained, ROC analysis was employed to quantify how magnitude and time delay could distinguish between populations, both individually and in combination. Table 5.2 summarizes the nonparametric estimate of the area under the curve and the associated standard error for the cyclic variation parameters analyzed individually as well as in combination. When the subjects are divided into quartiles of HbA1c, the magnitude of cyclic variation yielded an area and standard error of 0.69 ± 0.07. The normalized time delay, for these subjects, resulted in an area under the curve and standard error of 0.75 ± 0.06, and

TABLE 5.2: A summary of the nonparametric estimate of the area under the Receiver Operating Characteristic curve (AUC) and the associated standard errors (St.Err.). The first two rows represent the results when only magnitude or normalized time delay information is used. The third row reports the results when the magnitude and time delay results are combined through Bayes classification. HbA1c = Hemoglobin A1c, HOMA-IR = Homeostasis model assessment for insulin resistance, TG/HDL-C = Triglyceride to high density lipoprotein-cholesterol ratio

	HbA1c	**HOMA-IR**	**TG/HDL-C**
	AUC ± St.Err.	AUC ± St.Err.	AUC ± St.Err.
Magnitude	0.69 ± 0.07	0.63 ± 0.07	0.58 ± 0.07
Delay	0.75 ± 0.06	0.74 ± 0.06	0.64 ± 0.07
Combination	0.78 ± 0.06	0.76 ± 0.06	0.68 ± 0.07

the combination of the magnitude and time delay of cyclic variation through Bayes classification gave an area and error of 0.78 ± 0.06. A similar trend is seen when the subjects are divided into quartiles of HOMA-IR. In this analysis the magnitude of cyclic variation resulted in an area and standard error of 0.63 ± 0.07, normalized time delay of cyclic variation yielded an area and error of 0.74 ± 0.06, and the combination of the two parameters gave an area and error of 0.76 ± 0.06. In the third measure, TG/HDL-C, the area under the curve and standard error for the magnitude of cyclic variation was 0.58 ± 0.07, and 0.64 ± 0.07 (area ± standard error) for the normalized time delay. The combination of magnitude and normalized time delay gave an area under the curve and standard error of 0.68 ± 0.07 for the TG/HDL-C grouping of subjects.

5.6 Discussion

Although the study subjects were considered to have clinically normal hearts as assessed by a stress echocardiography exam, and no greater than Stage 1 hypertension, differences in the magnitude and normalized time delay of cyclic variation were observed when the subjects were classified by hemoglobin A1c (HbA1c), homeostasis model assessment of insulin resistance (HOMA-IR), and the ratio of triglycerides to high-density lipoprotein cholesterol (TG/HDL-C). For each of these parameters, the cyclic variation of backscatter measurements behaved in a fashion similar to that observed in previous studies of subjects with type 1 and type 2 diabetes (Akdemir *et al.*, 2001; Di Bello *et al.*, 1995, 1996, 1998; Fang *et al.*, 2003; Perez *et al.*, 1992; Wagner *et al.*, 1995). Those studies showed that the magnitude of cyclic variation is larger and the normalized time delay measurements are smaller in normal hearts than in diabetic hearts. Figures 5.3 and 5.4 demonstrate a similar trend in the current subject population. The subjects with more favorable profiles (low HbA1c, HOMA-IR, or TG/HDL-C) have a larger magnitude and smaller time delay of cyclic variation than the subjects in the highest quartiles of each classification. These differences in the cyclic variation parameters reach significance in all but one instance.

The cyclic variation results may suggest a trend toward a larger area under the ROC curve when information from magnitude and time delay of cyclic variation is combined using Bayes classification than when each feature is analyzed individually. However this observed improvement is relatively modest, suggesting the need for

additional studies and the identification of additional features that may improve the approach used to characterize the cyclic variation waveform. Many laboratories only report the magnitude of cyclic variation, yet this study suggests an improved ability to distinguish between subject groups when both magnitude and time delay of cyclic variation are used together. This result is similar to that reported in the Wagner et al. study of type 1 diabetic patients with systemic complications versus normal controls (Wagner *et al.*, 1995). Unlike the Wagner et al. study, the current study examined subjects who have clinically normal hearts and no systemic complications from diabetes. Yet in spite of this, the magnitude and time delay measurements show differences between the two groups. The 95% confidence intervals calculated in the current study are comparable to those reported in Figures 2, 3, and 4 of the Wagner et al. paper despite the different subject populations. In the current study, the difference between the area under the curve for the magnitude, time delay, and combination of cyclic variation parameters could increase if a quadratic classifier was used in the Bayes classification rather than the linear classifier used in this study (Fukunaga, 1972; Wagner *et al.*, 1995). Although the calculated values for area under the curve are quite modest, they are comparable to the areas obtained when the ratio of triglyceride to high-density lipoprotein cholesterol is used as a surrogate for insulin resistance (Kannel *et al.*, 2008).

There are a number of limitations to the present study. First, because endomyocardial biopsy was not appropriate in these otherwise healthy subjects, we do not have direct evidence of myocardial abnormalities, either with regard to structure or

metabolism. Second, the body mass index of subjects in the highest quartiles was substantially larger than that in the lowest quartiles for all three metabolic parameters. However, because obesity is a known risk factor for the development of type 2 diabetes, this finding is not unexpected. Studies suggest that there may be a link between obesity and the magnitude of cyclic variation of backscatter (Di Bello *et al.*, 2006; Wong *et al.*, 2004). This connection could be due to the influence of obesity on the load experienced by the myocardium. However, studies have shown that the magnitude of cyclic variation is relatively preload and afterload independent (Naito *et al.*, 1996).

In summary, classifying subjects according to hemoglobin A1c, homeostasis model assessment of insulin resistance, and the ratio of triglycerides to high-density lipoprotein cholesterol resulted in differences in the magnitude and normalized time delay of cyclic variation between the lowest and highest quartile groups for each classification. In the long view, these results suggest that monitoring the hearts of patients with type 2 diabetes using the combination of magnitude and time delay of cyclic variation of backscatter might permit observation of changes associated with disease progression that may contribute to the development of diabetic cardiomyopathy.

5.7 Appendix

5.7.1 Bayes Classification

A detailed description of Bayes classification can be found in *Introduction to Statistical Pattern Recognition* by Fukunaga and is summarized below (Fukunaga, 1972). In this study Bayes classification analysis used cyclic variation results to calculate a decision rule that minimized the error of identifying a new subject with the wrong group. The Bayes decision rule incorporated both the magnitude and normalized time delay from the same subject and used information about the mean and covariance of the tests within both groups.

In general, when the two populations studied are normally distributed and their covariance matrices are equal, the Bayes decision rule simplifies to a linear classifier,

$$h(X) = (M_2 - M_1)^T \Sigma^{-1} X + \frac{1}{2}(M_1^T \Sigma^{-1} M_1 - M_2^T \Sigma^{-1} M_2) \tag{5.1}$$

where $h(X)$ is the log likelihood ratio that the subject is in population 1 or 2, X is a vector of test results for one subject, M is a vector representing the means for each test, Σ is the covariance matrix, T the matrix transpose, and the subscripts 1 and 2 represent the two different populations (Fukunaga, 1972). The elements of the covariance matrices were calculated using the formula

$$\sigma_{mn}^2 = \frac{1}{N-1} \sum_{k=1}^{N} (x_{mk} - \mu_m)(x_{nk} - \mu_n) \tag{5.2}$$

In the cyclic variation analysis, N is the number of subjects in the test population, x is the k^{th} subject's test result for test m or n, and μ is the mean of test m or

n, where m and n are indices corresponding to the diagnostic tests that are being compared. In this cyclic variation analysis, two tests (magnitude and time delay) were analyzed for each patient, so m and n both run from 1 to 2, and four covariance matrix elements are calculated. If the two populations studied (highest and lowest quartiles) do not have equal covariance matrices, the elements in the covariance matrix of population 1 can be averaged with the corresponding elements in the covariance matrix of population 2 to yield a common covariance matrix (Wagner *et al.*, 1995). Alternatively a quadratic classifier can be calculated for the decision rule. In the present study, the covariance matrices for the two groups were averaged and a linear classifier was employed in order to make the results comparable to those presented in the Wagner et al. study of type 1 diabetic patients (Wagner *et al.*, 1995). In the current study the $h(X)$ values ranged from approximately -3 to 3 with negative $h(X)$ values indicating a higher likelihood to be in population 1 and positive $h(X)$ values signifying the subject is more likely to be in population 2.

The calculated linear classifier was estimated from a finite sample of subjects resulting in a decision rule that was derived from imperfect information. The performance of this classifier is expected to be inferior to a decision rule based on precise knowledge of the study population, but by using resampling techniques the effects of finite sample size can be reduced. The primary resample method was round-robin classification, also known as leave-one-out jackknife (Efron, 1982; Wagner *et al.*, 1995). In the round-robin resampling scheme, one of the samples was held out of the training set and the other samples were used to calculate or train the classifier. The left

out sample was then classified using the trained decision rule and replaced into the original dataset. After replacement of the first left-out sample, a different sample was removed from the training dataset and the remaining samples were used to calculate the decision rule. The newly calculated decision rule was slightly different from the first rule because the training dataset included the previously left-out sample and did not include the latest sample that was removed. The removed sample was classified using the latest decision rule and then the sample was moved back into the original dataset. This process was repeated multiple times with different samples excluded from the training set until all the samples were classified and results could be used in ROC analysis.

5.7.2 Receiver Operating Characteristic (ROC) Analysis

A nonparametric estimate of the area under the ROC curve was used to assess the performance of the Bayes classified data by quantifying its ability to distinguish between the two populations. ROC analysis provides a description of the separability of two groups that is independent of a decision threshold, a test interpreter's mindset, and prevalence of the disease. This method of analysis often relates the true positive fraction (the fraction of actually positive cases that are identified as positive by the test) to the false positive fraction (the fraction of actually negative cases that are called positive by the test) as a function of decision threshold. An ideal test with clear separation between test results of two groups would yield an area under the curve of 1.0. Conversely an area under the curve of 0.50 is representative of a random

guess. In general an area under the curve between 0.50 and 0.70 indicates a poor test performance, an area between 0.70 and 0.80 is considered fair, 0.80 to 0.90 is good, and an area greater than 0.90 is considered excellent (Kannel *et al.*, 2008).

The nonparametric estimate of area under the curve is also referred to as the Wilcoxon (Wilcoxon, 1945) and the Mann-Whitney U-statistic (Mann and Whitney, 1947). Several studies have shown that these unbiased estimators are analogous to that of the parametric area under the ROC curve (Bamber, 1975; DeLong *et al.*, 1988; Gallas, 2006; Hanley and McNeil, 1982). The Wilcoxon and Mann-Whitney U-statistic estimate the probability that a randomly selected result from one group will be greater than or equal to a randomly selected result from the other group. This statistic W is expressed as

$$W = \frac{1}{M \cdot N} \sum_{j=1}^{N} \sum_{i=1}^{M} \Psi(X_i, Y_j) \quad \text{where} \quad \Psi(X_i, Y_j) = \begin{cases} 1 & \text{if } Y < X \\ \frac{1}{2} & \text{if } Y = X \\ 0 & \text{if } Y > X \end{cases} \tag{5.3}$$

In this formulation, the two subject groups are represented by X and Y, with subject populations M and N respectively. This figure of merit can be interpreted as the expected percent correct in a binary decision situation. As more test results are assigned to the correct population the statistic W gets closer to 1.0, in a fashion similar to that of the parametric area under the ROC curve. In this study all of the ROC results reported are from a nonparametric estimate of the area under the ROC curve.

5.8 Acknowledgments

We would like to acknowledge the late Dr. Robert F. Wagner for his support and guidance with this project and throughout years of collaboration. This research was supported in part by NSF 57238 (FDA Scholar in Residence), NIH P20 RR020643, NIH HL 40302, Burroughs Wellcome Fund (1005935), and a grant from the Barnes Jewish Foundation.

Bibliography

Akdemir, O., Dagdeviren, B., Altun, A., Ugur, B., Arikan, E., Tugrul, A., and Ozbay, G. (**2001**). "Quantitative ultrasonic myocardial texture analysis of the diabetic heart", Anadolu Kardiyol Derg **1**, 17–21; AXIII.

Alavaikko, M., Elfving, R., Hirvonen, J., and Jarvi, J. (**1973**). "Triglycerides, cholesterol, and phospholipids in normal heart papillary muscle and in patients suffering from diabetes, cholelithiasis, hypertension, and coronary atheroma", J Clin Pathol **26**, 285–93.

Augustus, A. S., Kako, Y., Yagyu, H., and Goldberg, I. J. (**2003**). "Routes of FA delivery to cardiac muscle: modulation of lipoprotein lipolysis alters uptake of TG-derived FA", Am J Physiol Endocrinol Metab **284**, E331–9.

Bamber, D. (**1975**). "The area above the ordinal dominance graph and the area below the receiver operating characteristic graph", J. Math Psych **12**, 387–415.

Barrett-Connor, E., Grundy, S. M., and Holdbrook, M. J. (**1982**). "Plasma lipids and diabetes mellitus in an adult community", Am J Epidemiol **115**, 657–63.

Barzilai, B., Madaras, E. I., Sobel, B. E., Miller, J. G., and Perez, J. E. (**1984**). "Effects of myocardial contraction on ultrasonic backscatter before and after ischemia", Am J Physiol **247**, H478–83.

Borradaile, N. M. and Schaffer, J. E. (**2005**). "Lipotoxicity in the heart", Curr Hypertens Rep **7**, 412–7.

Carley, A. N. and Severson, D. L. (**2005**). "Fatty acid metabolism is enhanced in type 2 diabetic hearts", Biochim Biophys Acta **1734**, 112–26.

Chiu, H. C., Kovacs, A., Blanton, R. M., Han, X., Courtois, M., Weinheimer, C. J., Yamada, K. A., Brunet, S., Xu, H., Nerbonne, J. M., Welch, M. J., Fettig, N. M., Sharp, T. L., Sambandam, N., Olson, K. M., Ory, D. S., and Schaffer, J. E. (**2005**). "Transgenic expression of fatty acid transport protein 1 in the heart causes lipotoxic cardiomyopathy", Circ Res **96**, 225–33.

Chiu, H. C., Kovacs, A., Ford, D. A., Hsu, F. F., Garcia, R., Herrero, P., Saffitz, J. E., and Schaffer, J. E. (**2001**). "A novel mouse model of lipotoxic cardiomyopathy", J Clin Invest **107**, 813–22.

DeLong, E. R., DeLong, D. M., and Clarke-Pearson, D. L. (**1988**). "Comparing the areas under two or more correlated Receiver Operating Characteristic curves: a nonparametric approach", Biometrics **44**, 837–45.

Di Bello, V., Giampietro, O., Matteucci, E., Giorgi, D., Bertini, A., Piazza, F., Talini, E., Paterni, M., and Giusti, C. (**1998**). "Ultrasonic tissue characterization analysis in type 1 diabetes: a very early index of diabetic cardiomyopathy?", G Ital Cardiol **28**, 1128–37.

Di Bello, V., Giampietro, O., Matteucci, E., Talarico, L., Giorgi, D., Bertini, A., Caputo, M. T., Piazza, F., Paterni, M., and Giusti, C. (**1996**). "Ultrasonic videodensitometric analysis in type 1 diabetic myocardium", Coron Artery Dis **7**, 895–901.

Di Bello, V., Santini, F., Di Cori, A., Pucci, A., Palagi, C., Delle Donne, M. G., Fierabracci, P., Marsili, A., Talini, E., Giannetti, M., Biadi, O., Balbarini, A., Mariani, M., and Pinchera, A. (**2006**). "Obesity cardiomyopathy: Is it a reality? An ultrasonic tissue characterization study", J Am Soc Echocardiogr **19**, 1063–71.

Di Bello, V., Talarico, L., Picano, E., Di Muro, C., Landini, L., Paterni, M., Matteucci, E., Giusti, C., and Giampietro, O. (**1995**). "Increased echodensity of myocardial wall in the diabetic heart: an ultrasound tissue characterization study", J Am Coll Cardiol **25**, 1408–15.

Efron, B. (**1982**). "The Jackknife, the Bootstrap and other resampling plans", in *CBMS-NSF Regional Conference Series in Applied Mathematics*, 1–26 (Society for Industrial and Applied Mathematics, Philadelphia).

Fang, Z. Y., Prins, J. B., and Marwick, T. H. (**2004**). "Diabetic cardiomyopathy: evidence, mechanisms, and therapeutic implications", Endocr Rev **25**, 543–67.

Fang, Z. Y., Yuda, S., Anderson, V., Short, L., Case, C., and Marwick, T. H. (**2003**). "Echocardiographic detection of early diabetic myocardial disease", J Am Coll Cardiol **41**, 611–7.

Finck, B. N., Han, X., Courtois, M., Aimond, F., Nerbonne, J. M., Kovacs, A., Gross, R. W., and Kelly, D. P. (**2003**). "A critical role for PPARalpha-mediated lipotoxicity in the pathogenesis of diabetic cardiomyopathy: modulation by dietary fat content", Proc Natl Acad Sci U S A **100**, 1226–31.

Fraze, E., Donner, C. C., Swislocki, A. L., Chiou, Y. A., Chen, Y. D., and Reaven, G. M. (**1985**). "Ambient plasma free fatty acid concentrations in noninsulin-dependent diabetes mellitus: evidence for insulin resistance", J Clin Endocrinol Metab **61**, 807–11.

Fukunaga, K. (**1972**). *Introduction to Statistical Pattern Recognition.* (Academic Press, Orlando, FL).

Gallas, B. D. (**2006**). "One-shot estimate of MRMC variance: AUC", Acad Radiol **13**, 353–62.

Giglio, V., Pasceri, V., Messano, L., Mangiola, F., Pasquini, L., Dello Russo, A., Damiani, A., Mirabella, M., Galluzzi, G., Tonali, P., and Ricci, E. (**2003**). "Ultrasound tissue characterization detects preclinical myocardial structural changes in children affected by Duchenne muscular dystrophy", J Am Coll Cardiol **42**, 309–16.

Hallgren, B., Stenhagen, S., Svanborg, A., and Svennerholm, L. (**1960**). "Gas chromatographic analysis of the fatty acid composition of the plasma lipids in normal and diabetic subjects", J Clin Invest **39**, 1424–34.

Hamby, R. I., Zoneraich, S., and Sherman, L. (**1974**). "Diabetic cardiomyopathy", JAMA **229**, 1749–54.

Hancock, J. E., Cooke, J. C., Chin, D. T., and Monaghan, M. J. (**2002**). "Determination of successful reperfusion after thrombolysis for acute myocardial infarction: a noninvasive method using ultrasonic tissue characterization that can be applied clinically", Circulation **105**, 157–61.

Hanley, J. A. and McNeil, B. J. (**1982**). "The meaning and use of the area under a Receiver Operating Characteristic (ROC) curve", Radiology **143**, 29–36.

Holland, M. R., Gibson, A., Kirschner, C., Hicks, D., Ludomirsky, A., and Singh, G. (**2009**). "Intrinsic myoarchitectural differences between the left and right ventricles of fetal human hearts: An ultrasonic backscatter feasibility study", J Am Soc Echocardiogr **22**, 170–176.

Holland, M. R., Gibson, A. A., Peterson, L. R., Areces, M., Schaffer, J. E., Perez, J. E., and Miller, J. G. (**2006**). "Measurements of the cyclic variation of myocardial backscatter from two-dimensional echocardiographic images as an approach for characterizing diabetic cardiomyopathy", J Cardiometab Syndr **1**, 149–52.

Hu, X., Wang, J., Sun, Y., Jiang, X., Sun, B., Fu, H., and Guo, R. (**2003**). "Relation of ultrasonic tissue characterization with integrated backscatter to contractile reserve in patients with chronic coronary artery disease", Clin Cardiol **26**, 485–8.

Iwakura, K., Ito, H., Kawano, S., Okamura, A., Asano, K., Kuroda, T., Tanaka, K., Masuyama, T., Hori, M., and Fujii, K. (**2003**). "Detection of TIMI-3 flow before mechanical reperfusion with ultrasonic tissue characterization in patients with anterior wall acute myocardial infarction", Circulation **107**, 3159–64.

JNC (**2003**). "The Seventh Report of the Joint National Committee on the Prevention, Detection, Evaluation, and Treatment of High Blood Pressure", Report, NIH National Heart Lung and Blood.

Kannel, W. B., Hjortland, M., and Castelli, W. P. (**1974**). "Role of diabetes in congestive heart failure: the Framingham study", Am J Cardiol **34**, 29–34.

Kannel, W. B., Vasan, R. S., Keyes, M. J., Sullivan, L. M., and Robins, S. J. (**2008**). "Usefulness of the triglyceride-high-density lipoprotein versus the cholesterol-high-density lipoprotein ratio for predicting insulin resistance and cardiometabolic risk (from the Framingham Offspring Cohort)", Am J Cardiol **101**, 497–501.

Komuro, K., Yamada, S., Mikami, T., Yoshinaga, K., Noriyasu, K., Goto, K., Onozuka, H., Urasawa, K., Fujii, S., Tamaki, N., and Kitabatake, A. (**2005**). "Sensitive detection of myocardial viability in chronic coronary artery disease by ultrasonic integrated backscatter analysis", J Am Soc Echocardiogr **18**, 26–31.

Losi, M. A., Betocchi, S., Chinali, M., Barbati, G., D'Alessandro, G., Cacace, A., Lombardi, R., Contaldi, C., de Simone, G., and Chiariello, M. (**2007**). "Myocardial texture in hypertrophic cardiomyopathy", J Am Soc Echocardiogr **20**, 1253–9.

Madaras, E. I., Barzilai, B., Perez, J. E., Sobel, B. E., and Miller, J. G. (**1983**). "Changes in myocardial backscatter throughout the cardiac cycle", Ultrason Imaging **5**, 229–39.

Mann, H. and Whitney, D. (**1947**). "On a test whether one of two random variables is stochastically larger than the other", Ann Math Statist **18**, 50–60.

Masuyama, T., St Goar, F. G., Tye, T. L., Oppenheim, G., Schnittger, I., and Popp, R. L. (**1989**). "Ultrasonic tissue characterization of human hypertrophied hearts in vivo with cardiac cycle-dependent variation in integrated backscatter", Circulation **80**, 925–34.

Micari, A., Pascotto, M., Jayaweera, A. R., Sklenar, J., Goodman, N. C., and Kaul, S. (**2006**). "Cyclic variation in ultrasonic myocardial integrated backscatter is due to phasic changes in the number of patent myocardial microvessels", J Ultrasound Med **25**, 1009–19.

Mobley, J., Banta, C., Gussak, H., Perez, J. E., and Miller, J. G. (**1995**). "Clinical tissue characterization: Online determination of magnitude and time delay of myocardial backscatter", Video Journal of Echocardiography **5**, 40–48.

Mohr, G. A., Vered, Z., Barzilai, B., Perez, J. E., Sobel, B. E., and Miller, J. G. (**1989**). "Automated determination of the magnitude and time delay ("phase") of the cardiac cycle dependent variation of myocardial ultrasonic integrated backscatter", Ultrason Imaging **11**, 245–59.

Naito, J., Masuyama, T., Mano, T., Yamamoto, K., Doi, Y., Kondo, H., Nagano, R., Inoue, M., and Hori, M. (**1996**). "Influence of preload, afterload, and contractility on myocardial ultrasonic tissue characterization with integrated backscatter", Ultrasound Med Biol **22**, 305–12.

Nielsen, L. B., Bartels, E. D., and Bollano, E. (**2002**). "Overexpression of apolipoprotein B in the heart impedes cardiac triglyceride accumulation and development of cardiac dysfunction in diabetic mice", J Biol Chem **277**, 27014–20.

Ohara, Y., Hiasa, Y., Hosokawa, S., Suzuki, N., Takahashi, T., Kishi, K., and Ohtani, R. (**2005**). "Ultrasonic tissue characterization predicts left ventricular remodeling in patients with acute anterior myocardial infarction after primary coronary angioplasty", J Am Soc Echocardiogr **18**, 638–43.

Perez, J. E., McGill, J. B., Santiago, J. V., Schechtman, K. B., Waggoner, A. D., Miller, J. G., and Sobel, B. E. (**1992**). "Abnormal myocardial acoustic properties in diabetic patients and their correlation with the severity of disease", J Am Coll Cardiol **19**, 1154–62.

Peterson, L. R., Herrero, P., Schechtman, K. B., Racette, S. B., Waggoner, A. D., Kisrieva-Ware, Z., Dence, C., Klein, S., Marsala, J., Meyer, T., and Gropler, R. J. (**2004**). "Effect of obesity and insulin resistance on myocardial substrate metabolism and efficiency in young women", Circulation **109**, 2191–6.

Rijzewijk, L. J., van der Meer, R. W., Smit, J. W., Diamant, M., Bax, J. J., Hammer, S., Romijn, J. A., de Roos, A., and Lamb, H. J. (**2008**). "Myocardial steatosis is an independent predictor of diastolic dysfunction in type 2 diabetes mellitus", J Am Coll Cardiol **52**, 1793–9.

Sharma, S., Adrogue, J. V., Golfman, L., Uray, I., Lemm, J., Youker, K., Noon, G. P., Frazier, O. H., and Taegtmeyer, H. (**2004**). "Intramyocardial lipid accumulation in the failing human heart resembles the lipotoxic rat heart", Faseb J **18**, 1692–700.

Stremmel, W. (**1988**). "Fatty acid uptake by isolated rat heart myocytes represents a carrier-mediated transport process", J Clin Invest **81**, 844–52.

Szczepaniak, L. S., Dobbins, R. L., Metzger, G. J., Sartoni-D'Ambrosia, G., Arbique, D., Vongpatanasin, W., Unger, R., and Victor, R. G. (**2003**). "Myocardial triglycerides and systolic function in humans: in vivo evaluation by localized proton spectroscopy and cardiac imaging", Magn Reson Med **49**, 417–23.

Wagner, R. F., Wear, K. A., Perez, J. E., McGill, J. B., Schechtman, K. B., and Miller, J. G. (**1995**). "Quantitative assessment of myocardial ultrasound tissue characterization through Receiver Operating Characteristic analysis of Bayesian classifiers", J Am Coll Cardiol **25**, 1706–11.

Wallace, T., Levy, J., and Matthews, D. R. (**2004**). "Use and abuse of HOMA modeling", Diabetes Care **27**, 1487–1495.

Wilcoxon, F. (**1945**). "Individual comparisons by ranking methods", Biometrics **1**, 80–83.

Witteles, R. M. and Fowler, M. B. (**2008**). "Insulin-resistant cardiomyopathy clinical evidence, mechanisms, and treatment options", J Am Coll Cardiol **51**, 93–102.

Wong, C. Y., O'Moore-Sullivan, T., Leano, R., Byrne, N., Beller, E., and Marwick, T. H. (**2004**). "Alterations of left ventricular myocardial characteristics associated with obesity", Circulation **110**, 3081–7.

Zhou, Y. T., Grayburn, P., Karim, A., Shimabukuro, M., Higa, M., Baetens, D., Orci, L., and Unger, R. H. (**2000**). "Lipotoxic heart disease in obese rats: implications for human obesity", Proc Natl Acad Sci U S A **97**, 1784–9.

Chapter 6

Dissertation Summary and Concluding Remarks

The goal of this Dissertation was to study the physics of sound waves incident upon the anisotropic and inhomogeneous myocardium. Ultrasound has been utilized as a clinical tool to assess heart structure and function, and the usefulness of this noninvasive approach has grown with our understanding of the mechanisms underlying the interaction of ultrasound with the myocardium. One aim of this Dissertation was to extend the knowledge of myocardial ultrasonic properties to include new information regarding asymptomatic type 2 diabetes patients and fetal hearts.

The first portion of the Dissertation demonstrated regional differences in mid-gestational fetal pig hearts by analyzing the ultrasonic properties of the anisotropic ventricular myocardium. The hearts were interrogated using a 50 MHz transducer that enabled finer spatial resolution than could be achieved at more typical clinical frequencies. By insonifying the tissue with higher frequencies and therefore shorter wavelengths, specific transmural layers of the ventricular myocardium could be re-

solved. Ultrasonic data analyses demonstrated the left ventricular myocardium appears to be composed of three layers whereas the right ventricular myocardium appears to consist of two layers. The data analyses also demonstrated bands within the midmyocardium of the left ventricular free wall and the subepicardial area of the right ventricular free wall that correspond to insonification perpendicular to the predominant myofiber orientation. Interestingly, these differences in the ventricular structure exist in spite of the fact that the left and right ventricles are exposed to similar pressures during fetal development, an important determinant of ventricular structure.

In addition to quantifying the myoarchitecture of the left and right ventricles, analyses were also performed to characterize areas of perpendicular insonification relative to the predominant myofiber orientation. These analyses documented further differences in the ultrasonic properties of the ventricular myocardium. In Chapter 2 it was shown that the apparent integrated backscatter was larger in the right ventricular myocardium than the left. Similarly in Chapter 3 the slope of attenuation and attenuation coefficient at midbandwidth were shown to be larger in the right ventricular myocardium than in the myocardium of the left ventricle. Unlike studies focused solely on the left ventricular myocardium, this work compared the ultrasonic properties of the right ventricles to that of the left in midgestational fetal hearts.

Chapter 5 demonstrated the clinical usefulness of ultrasound by analyzing the cyclic variation of myocardial backscatter in asymptomatic type 2 diabetes patients and in normal control subjects. Although the study subjects were considered to have

apparently normal hearts, differences in the magnitude and normalized time delay of cyclic variation of myocardial backscatter were observed when the subjects were classified based on hemoglobin A1c (HbA1c), the homeostasis model assessment of insulin resistance (HOMA-IR), and the ratio of triglycerides to high-density lipoprotein-cholesterol (TG/HDL-C). The cyclic variation results also suggest a trend toward a larger area under the ROC curve when information from magnitude and time delay of cyclic variation is combined using Bayes classification than when each featured is analyzed individually. In the long view, these results suggest that, by capitalizing on our understanding of the interaction of sound waves with myocardium, changes associated with disease progression may provide enhanced methods to monitor the hearts of patients undergoing treatment.

Ultrasound continues to be a powerful tool that enables noninvasive quantification of material properties. The studies in this Dissertation show that understanding the physical mechanisms that underpin the interaction of ultrasonic waves with myocardium can reveal beneficial information about the structure, composition, and overall state of the heart. By looking beyond the ultrasonic images themselves and quantifying the myocardial properties responsible for generating the images, we contribute to the knowledge base that ultimately provide improved diagnoses of congenital heart disease and of diabetic cardiomyopathy.